MAGNETIC BARKHAUSEN NOISE RESPONSE TO STRESS IN AIRCRAFT LANDING GEAR STEEL SAMPLES

LE BRUIT DE BARHAUSEN EN RÉPONSE AUX ÉCHANTILLONS D'ACIER SOUS CONTRAINTE MÉCANIQUE

A Thesis Submitted to the Division of Graduate Studies
of the Royal Military College of Canada
by

Julia Milne

Captain

In Partial Fulfillment of the Requirements for the Degree of
Master of Physics in Non-Destructive Evaluation

August, 2025

Abstract

A portable Magnetic Barkhausen noise (MBN) testing system was used to perform MBN measurements and hysteresis plots on three steel samples; 300M, AISI 4340 and HY80. The primary material for this research was 300M, which is used for CF-188 aircraft landing gear components, with the goal of developing a Non-Destructive Evaluation (NDE) method for evaluating residual stresses. Three experiments were conducted; hysteresis plots analyzed with the Włodarski Model, MBN response to elastic bending and MBN response to plastic bending. Results showed that the Włodarski Model could accurately approximate minor hysteresis loops for 300M. The second experiment showed a near linear relationship for MBN energy response to elastic tension in the samples, with the strongest correlation for 300M. The third experiment proposed a calibration method of using MBN energy response to elastic bending to estimate residual stress. The average final residual stress, for three 300M samples, estimated by this method was 550 $\pm$70 MPa. This was the lowest out of four residual stress estimation methods used, with the ANSYS model giving an average of 580 MPa and the strain calculations and profile measurement methods showing close agreement with 660 $\pm$50 MPa and 650 $\pm$30 MPa, respectively. These results indicate that the plastic deformation is suppressing MBN response, which should be further investigated for this calibration method. This research demonstrates potential of this MBN system to be used for NDE of residual stress in aircraft landing gear component material.

Résumé

Un système portable de mesure du bruit magnétique de Barkhausen (BMB) a été utilisé pour effectuer des mesures de BMB et pour tracer les cycles d'hystérésis sur trois échantillons d'acier; le 300M, l'AISI 4340 et le HY80. Le matériau principal de cette étude était le 300M, utilisé pour les composants du train d'atterrissage des avions CF-188. L'objectif de ce projet était de développer une méthode d'évaluation non destructive (END) magnétique permettant l'évaluation des contraintes internes résiduelles. Trois expériences ont été menées; des graphiques de cycles d'hystérésis analysés à l'aide du modèle de Włodarski, l'observation du BMB pour les échantillons sous contrainte mécanique de flexion élastique et sous contrainte de flexion plastique. Les résultats ont montré que le modèle de Włodarski permettait d'approximer avec précision les cycles mineurs d'hystérésis pour le 300M. La deuxième expérience a montré une relation quasi-linéaire des mesures de l'énergie du BMB et de la contrainte élastique appliquée aux échantillons. La troisième expérience a proposé une méthode d'étalonnage utilisant les variations de l'énergie du BMB à une flexion élastique pour estimer les contraintes internes résiduelles. Cette méthode a estimé la contrainte résiduelle finale moyenne pour trois échantillons de 300M de 550 $\pm$70 MPa. C'était la plus basse parmi les quatre méthodes d'estimation utiliser; le modèle ANSYS a donné une moyenne de 580 MPa, et les méthodes de calcul de la déformation et de mesure du profil ont montré une concordance proche de 660 $\pm$50 MPa et 650 $\pm$30 MPa, respectivement. Ces résultats ont indiqué que la déformation plastique supprime les signaux du BMB. Cette recherche a démontré le potentiel de ce système de mesure du BMB pour être utiliser pour l'END des contraintes internes résiduelles dans les matériaux des composants de train d'atterrissage d'avion.

Acknowledgements

First of all, I would like to thank my supervisor, Professor Thomas Krause, for his guidance and expertise throughout this research. I am very grateful for all the feedback, encouragement, instruction and direction he generously gave me over these past two years.

I would like to express my gratitude to Dr. Ross Underhill, who's knowledge and experience in this area of research, and the inner workings of the non-destructive laboratory, were invaluable. Without his assistance, and the support of the lab technicians, Peter Snell and Mich Lavoie, these experiments would not have been possible.

I'd like to acknowledge my colleague, Fan Liu, who conducted the ANSYS simulation for the finite element method stress analysis. His model results provided valuable data and supported the stress calculations for my third experiment.

Finally, I would like to thank my family. To my parents and partner Richard, who understand the challenges of graduate studies and gave me their love, patience and support. Thank you for everything!

Contents

List of Figures

List of Tables

List of Acronyms

AISI American Iron and Steel Institute

BCC Body-Centred Cubic

BH B and H field

CF Canadian Fighter

DW domain wall

DWs domain walls

emf electromotive force

FEM Finite Element Method

FORC First-Order Reversal Curve

J-A Jiles-Atherton model

MBN Magnetic Barkhausen noise

MBNe Magnetic Barkhausen noise energy

mmf magnetomotive force

MO Magnetic Object model

NDE Non-Destructive Evaluation

NDT Non-Destructive Testing

RCAF Royal Canadian Air Force

RMS Root-Mean-Squared

SAE Society of Automotive Engineers

SEM Scanning Electron Microscope

SSE sum-squared-error

List of Symbols

a	Radius of the loop or solenoid
a	Włodarski model parameter for the reversal rate from saturation
$\vec{a}$	Small area vector created by an orbiting electron
b	Włodarski model parameter for the rate of approach to saturation
c	Włodarski model parameter for the coercivity component
c	Distance location of the centroid of the beam
$d\vec{a}$	An elemental area vector
$d\vec{I}'$	Unit length of the current vector with respect to the point r
dl'	Unit vector length with respect to the point r
f	Frequency in Hz
l	Length
i, j	Neighbouring positions in a lattice structure
m	Unit meters
$\vec{m}$	Magnetic moment of an atom
$\vec{n}$	Normal component of magnetization
r	A point at which the electric and magnetic field effects are considered
$\vec{r}$, $\hat{r}$	The vector and unit vector of the distance from the fields to the point r
s	Unit seconds

t	Time
$\vec{v}$	Velocity vector
x, y, z	Distances along the x, y or z-axis
A	Unit Amperes
A, $\vec{A}$	Cross-sectional area and area vector
B, $\vec{B}$	Magnetic flux density or external magnetic field
E	Young's modulus or modulus of elasticity in GPa
$\vec{E}$	Electric field
F	Force, by physical load in Neutons
$\vec{F}$	Force vector acting on a test change
$\mathcal{F}$	Magnetomotive force
$F()$	An odd function, used in the Włodarski model
H	Unit Henrys
H, $\vec{H}$	Applied magnetic field or H field
Hz	Unit Hertz
I,$\vec{I}$	Current or current vector
$\vec{J}$	Volume current density vector
L	Length, with a given measurement
M, $\vec{M}$	Magnetization of the material, magnetic field
N	Number of turns or loops in a solenoid
Pa	Unit Pascals
Q	A test charge
R	Electrical resistance
$\mathcal{R}$	Magnetic reluctance

S Unit Siemens

T Temperature

T Unit Teslas

V Unit Volts

V Electrical potential or voltage drop/difference

α and β Switch up and switch down values for the H field of a elementary hysteresis operator for the Preisach model.

α, α_1, α_2, α_3 Directional cosines relative to the easy axis directions

γ, γ_1, γ_2, γ_3 Directional cosines of the stress tensor with respect to the easy axis

δ Bending deflection in mm

ϵ Strain tensor, mechanical strain

θ Angle between the direction of magnetization and the easy axis

κ, κ_0, κ_1, κ_2 Anisotropy energy constants

λ, λ_t Magnetostriction, transverse magnetostrictive strain

μ Magnetic permeability

ν Slope of the hysteresis loop in the Rayleigh region

π The number pi

ρ Density of electrical charge

σ Stress tensor, applied mechanical stress

χ Susceptibility

ω angular frequency in rad/s

Φ Magnetic flux through an area

Ω Unit ohms

h_p Height of the plastic zone

B_1, B_2 Magnetic B field for the first and second branches of a hysteresis loop, respectively

B_-, B_+ Magnetic B field for the upper and lower branches of a hysteresis loop, respectively

E_{ex} Exchange energy

E_{ms} Magneto-static energy

E_κ Anisotropic energy

E_σ Magnetostrictive energy

$\vec{F}_{mag}$ Magnetic component of the force vector acting on a test change

H_a or H_r The reversal point for a partial hysteresis curve for the FORC method

H_d Internal demagnetization field

H_{eff} Effective applied magnetic field

H_m Maximum H field amplitude

I_{enc} Enclosed or bound current

I_z Second moment of inertia, about the z-axis

$\vec{J}_b$ Bound volume current density vector

J_{ex} Exchange energy integral

$\vec{J}_f$ Free volume current density vector

M_1, M_2 or M_{12} Magnetic M field for the first and second branches of a hysteresis loop, respectively

M_a Reversible magnetization parameter

M_b Irreversible magnetization parameter

M_s Magnetization field at saturation

M_z Bending moment, about the z-axis

M_-, M_+ Magnetic M field for the upper and lower branches of a hysteresis loop, respectively

N_d	Demagnetization factor
S_i, S_j	Spin vectors ($\pm 1/2$) of neighbouring atoms in lattice sites i and j
T_c	Curie Temperature
V_a, V_b	Voltage at point a and b
δ_s	Skin depth, penetration of an electromagnetic wave in mm
ϵ_0	Permittivity of free space
λ_l	Charge density of a line element
λ_s	Magnetostriction at saturation
λ_{100}, λ_{110}, λ_{111}	Magnetostrictive strain in the 100, 110, and 111 crystalline directions
μ_0	Magnetic permeability of air or free space
μ_i	Initial permeability, referring to the Rayleigh region
μ_r	Relative permeability
σ_c	Electrical conductivity in S/m
σ_e	Maximum stress of the elastic regime, the yield point in MPa

1 Introduction

Aircraft landing gear are typically made of high strength steel that can accumulate residual stress due to repetitive loading from regular use and occasional hard landings. This residual stress may not result in visually apparent plastic deformation, and therefore, could be missed during inspections and affect the serviceability of the component. Residual stress compounds with applied loads, which increases the risk of failure. A Non-Destructive Testing (NDT) method that could assess the stress state of aircraft landing gear could be used to determine component serviceability and potentially reduce costs by reducing the number of unnecessary component replacements.

Current NDT methods for detecting residual stress in metals are limited to X-ray and neutron diffraction [1]. X-ray requires surface preparation, such as nital etching, which removes approximately 0.2 mm of surface material, and the method has limited penetration depth, approximately 0.15 mm in steel [2]. Both methods are expensive and neutron diffraction is not portable [3]. For these reasons, neutron and X-ray diffraction techniques have limited applications in aviation, and are reserved more for the detection of water ingress, cracks and corrosion [4], rather than for detecting stress.

This thesis explores the Magnetic Barkhausen noise (MBN) response to stress in 300M steel samples, which is the material used for Canadian Fighter (CF)-188 aircraft landing gear components. There is a correlation between mechanical stress and magnetic response in ferromagnetic materials, which gives this approach the potential to be used for NDT. MBN is approved as a technique for the detection of grinding burns, by the Society of Automotive Engineers (SAE) Standard ARP4462 [5], and the United States Navy has a procedure for using it to detect residual stress in their F-18 aircraft landing gear [6]. Despite

this, it is not an approved technique for aircraft inspection in the Royal Canadian Air Force (RCAF).

1.1 Thesis scope

The work is broken into three experiments; the first one measures the magnetic hysteresis plots and conducts analysis by the Włodarski Model [7][8], and second one explores the MBN response to elastic bending. The third experiment extends the MBN bending response into the plastic regime and measures the hysteresis plots before and after plastic deformation. The objective of this thesis work is to explore an MBN calibration method for detecting and estimating residual stress in 300M steel samples, with the goal of developing an NDE application for aircraft landing gear.

Novelty of this thesis work lies in the experimental equipment used and the method of analysis. MBN evaluation of 300M samples is conducted with a unique four-point bending apparatus and a custom built portable MBN system [9][10]. This research differs, in that the MBN responses of 300M samples are compared with that of AISI 4340 and HY80 steel, along with their hysteresis curves. The Włodarski model has not previously been used to approximate the hysteresis curves of martensitic steels such as 300M. The stress of the bent samples have been compared to strain gauge measurements, bent profile calculations and Finite Element Method (FEM) model simulations.

1.1.1 Organization of this thesis

The organization of this thesis begins with the background theory relevant to MBN measurements and magnetic hysteresis, then the experimental instruments, equipment and samples are introduced, followed by the results of three experiments, and discussions. The Sections of this thesis are as follows:

2. Background
    - Covers an introduction to electro-magnetics, magnetic hysteresis, and domain theory, as it applies to MBN detection systems and ferromagnetic materials.

3. Experimental equipment and materials
    - Discusses the equipment; the MBN system, the bending apparatus and the hysteresis measurement set up, and the sample materials; 300M, AISI 4340 and HY80 steel.
4. Experiment 1: Hysteresis plot experiment
    - Investigates the applicability of the Włodarski model [8][7] to approximate experimentally measured hysteresis plots of 300M, AISI 4340 and HY80 steel samples.
5. Experiment 2: Elastic bending experiment
    - Explores the relationship of MBN energy response to elastic bending stress.
6. Experiment 3: Plastic bending experiment
    - Investigates an MBN calibration method for estimating residual stress of plastically bent samples, which is compared to an ANSYS FEM model, strain gauge measurements and bent profile measurements. Hysteresis plots are measured before and after bending, and compared with MBN results.
7. Discussion
    - Presents discussions on the results from Sections 4, 5 and 6.
8. Conclusions
    - Presents a summary of the findings and provides suggestions for future research and next steps for the development of an MBN technique for detection of residual stress in aircraft landing gear.

2 Background

2.1 Electro-magnetics

Magnetic fields are produced by the movement of electric charge, either from an electrical current or the property of orbital motion and electron spin within the atom, as is the case with a permanent magnet [11]. The relationship between the electric field, $\vec{E}$, and magnetic field, or magnetic flux density, $\vec{B}$, is given by Maxwell's equations [12]:

Gauss's law:

$$\nabla \cdot \vec{E} = \frac{1}{\epsilon_0}\rho \tag{2.1.1}$$

Faraday's law:

$$\nabla \times \vec{E} = -\frac{\partial \vec{B}}{\partial t} \tag{2.1.2}$$

Gauss's law for no magnetic monopoles:

$$\nabla \cdot \vec{B} = 0 \tag{2.1.3}$$

Ampère's law with Maxwell's correction:

$$\nabla \times \vec{B} = \mu_0 \vec{J} + \mu_0 \epsilon_0 \frac{\partial \vec{E}}{\partial t} \tag{2.1.4}$$

where $\epsilon_0 = 8.85 \times 10^{-12}$ C^2/Nm^2 is permittivity of free space, $\mu_0 = 4\pi \times 10^{-7}$ N/A^2 is permeability of free space, ρ is the density of electrical charge, $\vec{J}$ is the volume current density vector, and *t* is time.

Of the four equations, Faraday's law, Equation 2.1.2, no magnetic monopoles, Equation 2.1.3, and Ampére's law, Equation 2.1.4, are the most relevant to this research, as they relate to the induction of a magnetic field, closed magnetic lines of flux and the affect of a magnetic field through mediums, respectively.

2.1.1 Faraday's Law

Faraday's law, also called Faraday's law of induction, describes how an electric field induces a time-dependent magnetic field and vise versa. This law considers the voltage drop, or electromotive force (emf), around a loop of wire causing or inducing a change in the magnetic field enclosed by the loop. The integral form of Equation 2.1.2 is:

$$V_{emf} = \oint \vec{E} \cdot d\vec{l} = -\frac{d}{dt} \int \vec{B} \cdot d\vec{A} \,, \tag{2.1.5}$$

where $d\vec{l}$ is an elemental segment of wire loop and $d\vec{A}$ is the elemental area enclosed, which can be replaced by N number of turns to represent a coil around that area A;

$$V = -NA\frac{dB}{dt} = -N\frac{d\Phi}{dt} \,, \tag{2.1.6}$$

where Φ is the magnetic flux and this equation shows how changing flux is related to the changing flux density B through the enclosed area A. This form of the equation, also known as the flux rule [12], is useful for measuring the magnetic field through a sample, by way of an encircling coil wrapped around a metal core, as shown in Figure 2.1, or inducing a field in a U-core magnet.

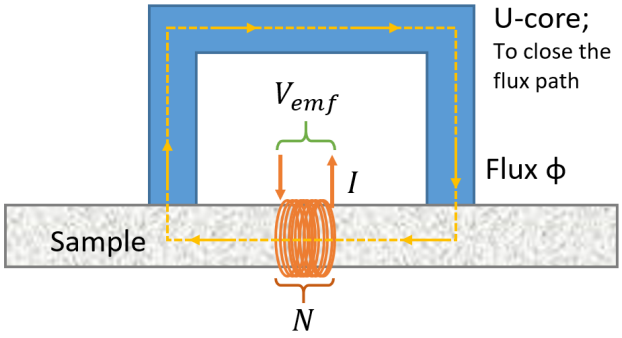

Figure 2.1: Flux through a sample and a U-core as measured by an encircle coil.

In order to make the assumption of average flux density B through the cross-sectional area of a metal as shown in Equation 2.1.6, skin depth effects must be considered. Skin depth, δ_s, is defined as the distance it takes for an electromagnetic wave travelling into a medium to decrease in amplitude by a factor of 1/e (approximately a third) [10]. This

example with a tangential magnetic field travelling into an infinite planar sample can be expressed for frequencies, f (Hz), below the microwave range ($f < 10^8$ Hz) [13] as;

$$\delta_s = \sqrt{\frac{2}{\omega\sigma_c\mu_0\mu_r}} = \frac{1}{\sqrt{\pi f\sigma_c\mu_0\mu_r}}\ , \tag{2.1.7}$$

where $\omega = 2\pi f$ is the angular frequency (rads/s), σ_c is the conductivity (S/m) of the material, and μ_r is the relative permeability. This equation is often used for a finite sample, as is the case for this research, but it should be noted that geometry will modify the electromagnetic wave interactions. Through modelling, S. White [10] found that the skin depth at which MBN signals can be picked up, which has frequencies between 3-300 kHz, is of approximately 2/3rd that given by the Equation 2.1.7 for a finite sample. This demonstrates that Equation 2.1.7 provides an approximation for the best case skin depth calculation.

The conductivity of a material, σ_c can be measured by the electric potential or voltage drop between two points; a and b due to an $\vec{E}$ field through it, according to Ohm's law and Kirchoff's voltage law [14];

$$\sigma_c = \frac{lI}{(V_a - V_b)A} \tag{2.1.8}$$

where l is the distance between points a and b, A is the cross-sectional area and $V_a - V_b = V$ is the measured potential.

2.1.2 Ampère's law

Ampère's equation with Maxwell's correction can be simplified for frequencies below the microwave range ($f < 10^8$ Hz) [13] because $\vec{J} \gg \epsilon_0\frac{\partial\vec{E}}{\partial t}$. this allows the second term in Equation 2.1.4 to be neglected:

$$\nabla \times \vec{B} = \mu_0\vec{J}\ , \tag{2.1.9}$$

where the current density $\vec{J}$ can be considered as the sum of bound current, $\vec{J}_b$ within the material and free current $\vec{J}_f$;

$$\vec{J} = \vec{J}_b + \vec{J}_f\ . \tag{2.1.10}$$

Bound currents are attributed to the magnetization field, $\vec{M}$, within the material and free currents are attributed to the applied or auxiliary field, $\vec{H}$, produced by a current through a

coil. They are expressed as:

$$\nabla \times \vec{M} = \vec{J_b} \ , \tag{2.1.11}$$

and

$$\nabla \times \vec{H} = \vec{J_f} \ . \tag{2.1.12}$$

Combining Ampère's law with Equations 2.1.10, 2.1.11 and 2.1.12 gives an expression for the magnetic flux density through a magnetized material:

$$\vec{B} = \mu_0(\vec{M} + \vec{H}) \ , \tag{2.1.13}$$

where $\vec{B}$ is in units of Tesla, $\vec{M}$ and $\vec{H}$ are in units of A/m. This equation shows the relationship between the three fields for a material being magnetized.

2.1.3 Magnetic Circuits

Magnetic field behaviour in physically connected elements can be considered as magnetic circuits, analogous to electric circuits, with the caveat that magnetic field lines can leak out of the circuit [14]. In this analogy, shown in Table 2.1, the driving field is the applied $\vec{H}$ field, the magnetic flux, Φ acts as a current, and the $\vec{B}$ field can be considered as a current density.

Table 2.1: Comparison of electric and magnetic circuit equivalences (adapted from [14]).

Electric	**Magnetic**
Electric Field $\vec{E}$	Auxiliary Field $\vec{H}$
Current $I = \int \vec{J} \cdot d\vec{A}$	Magnetic flux $\Phi = \int \vec{B} \cdot d\vec{A}$
Current Density $\vec{J_f} = \sigma_c E$	Flux Density $\vec{B} = \Phi / A$
Conductivity σ_c	Permeability $\mu = \mu_0 \mu_r$
electromotive force (emf) V_{emf}	magnetomotive force (mmf) $\mathcal{F}$
Resistance $R = l/\sigma_c A = V/I$	Reluctance $\mathcal{R} = l/\mu A = \mathcal{F}/\Phi$
Ohm's law $V = IR = El$	Ohm's law $\mathcal{F} = Hl = \mathcal{R}\Phi = NI$

Coils or solenoids are used to measure time varying $\vec{B}$ fields using Faraday's law of induction Equation 2.1.5. They are similar to conductors when a magnetic equivalent to a current ($\vec{H}$ field) is applied to them, or to inductors when the circuit induces a current in

them, as is the case with a pick-up coil. In magnetic circuit theory, magnetomotive force (mmf), $\mathcal{F}$, is analogous to the voltage emf so that Equation 2.1.5 through a conductive material has the magnetic circuit equivalent [14]:

$$\mathcal{F} = NI = \oint \vec{H} \cdot d\vec{l} = \int \vec{J}_f \cdot d\vec{A} \,, \tag{2.1.14}$$

where current I is related to the free current density J_f, which comes from the applied $\vec{H}$ field as shown with Equation 2.1.12, and mmf is in units of ampere-turns. The source of this force is usually a coil carrying a current, which produces a magnetic flux, Φ, which flows through the circuit. Flux is related to $\mathcal{F}$ by the reluctance $\mathcal{R}$ through the material, in the same way that voltage is described by Ohm's law:

$$\mathcal{F} = \mathcal{R}\Phi \,. \tag{2.1.15}$$

2.2 Magnetic Hysteresis

Magnetic hysteresis describes the behaviour of a material subjected to an $\vec{H}$ field, represented by an $\vec{H}$ versus $\vec{B}$ field plot, or an $\vec{H}$ versus $\vec{M}$ field plot. Hysteresis means to lag behind due to energy losses in the system, which prevents the material from immediately reaching saturation when exposed to an applied field. Sources of loss are due to impurities or defects in the material, magnetic anisotropy and coercivity [15], and the energy is dissipated in the form of heat due to eddy current [16].

This energy loss prevents smooth magnetization, at the macroscopic scale, and is indicative of an irreversible magnetization process, which produces Barkhausen noise [17]. Figure 2.2 shows a typical hysteresis loop zooming in to show the steps or jumps of the magnetization process, which produce MBN signals.

Key characteristics of hysteresis plots are; the x-axis intersection, which indicates the material's coercivity, H_c, and the y-axis intersection, which is the material's remanence, B_r, as indicated in Figure 2.3. The rate of magnetization due to an applied field is dictated by the material's permeability, μ. Coercivity is a characteristic of how magnetically hard a material is and determines the width of the hysteresis loop. For example, ferrites are

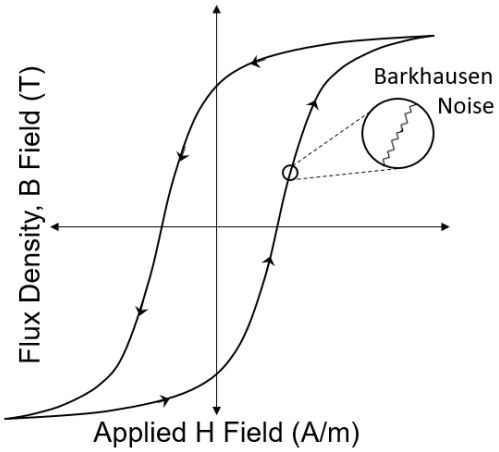

Figure 2.2: Magnetic hysteresis loop of a ferromagnetic material showing the irreversible changes associated with Barkhausen noise (adapted from [18]).

magnetically soft and magnetize easily with low coercivity, whereas permanent magnets are very magnetically hard [19]. Remanence is the level of magnetization that would be left in the material if the applied field was removed, which is high for permanent magnets and an important characteristic for magnetic recording applications [15].

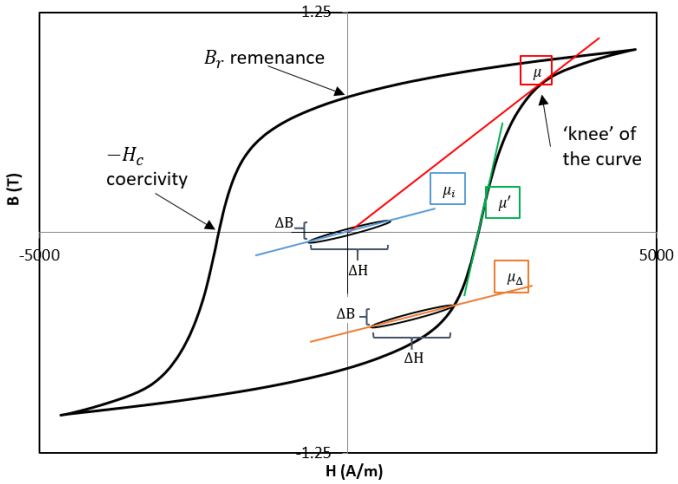

Figure 2.3: Depiction of plot hysteresis characteristics and different forms of permeability represented on a hysteresis plot of 300M steel.

Relative permeability, μ_r is the ratio of the material's permeability and that of free

space, resulting in a dimensionless ratio:

$$\mu_r = \frac{1}{\mu_0}\left(\frac{B}{H}\right) = \frac{1}{\mu_0}\left(\frac{1}{H}\mu_0(H+M)\right) = 1 + \frac{M}{H} = 1 + \chi\ . \tag{2.2.1}$$

where χ is susceptibility, which is the ratio of M and H, $\chi = M/H$.

Figure 2.3 shows different forms of permeability, with the maximum relative permeability as the red slope to the knee of the curve. This is the form of μ_r explored in this research, but it is also useful to be aware of the other types of permeability. Initial permeability, μ_i, is the slope of a minor hysteresis loop or the beginning of the initial magnetization curve, used to characterize the behaviour in the Rayleigh region [17]. Differential permeability, $\mu' = \frac{1}{\mu_0}\frac{\partial B}{\partial H}$, is often used to describe the steepest tangent slope of the curve around the coercivity intercept. Incremental permeability, $\mu_\Delta = \frac{\Delta B}{\Delta H}$, is used to describe the slope of a minor hysteresis loop.

Relative permeability is one of the indicators of magnetic classification for diamagnetic, paramagnetic and ferromagnetic or ferrimagnetic materials. A diamagnetic material has low susceptibility, and low permeability, and a perfect diamagnet is a superconductor. Paramagnetic material has higher susceptibility and permeability and ferromagnetic or ferrimagnetic materials have very high susceptibility and permeability. This research considers the magnetic behaviour of ferromagnetic samples, named after its iron content and strong magnetic response.

2.2.1 Models of magnetic hysteresis

Several models have been developed for representing the hysteric behaviour of ferromagnetic materials, including, but not limited to:

- The Rayleigh relation, 1887 [20], which uses a quadratic function to describe hysteresis loops at low H fields.
- The Preisach model, 1935 [21], which approximates hysteresis by summing a series of elementary rectangular loops.

- The Jiles-Atherton model (J-A) model, 1983 [22], which numerically solves a differential magnetization equation to describe domain wall motion subjected to pinning and effective H field strength.
- The Stoner-Wohlfarth model, 1991 [23], which is based on magnetization by domain rotation and is applicable to the anisotropy of magnetic powder [11].
- The First-Order Reversal Curve (FORC) method, 1999 [24], which computes multiple reversal paths to plot hysteresis.
- The Włodarski Model, 2007 [7], which constructs symmetric branches of hysteresis loops through superposition of reversible and irreversible magnetization terms.

This research explores the applicability of the Włodarski Model [7] for modelling the hysteresis behaviour of high strength steel samples. A brief description and literature review on the other models can be referenced in Appendix A.

The **Włodarski Model** is an empirical model governed by an S-shaped odd function and five model parameters that can be derived directly from the initial magnetization curve [7],[8]. It is similar to the J-A model [22], in that the theory is based on reversible and irreversible magnetization components that superimpose to create the BH curve of a hysteresis loop. The model differs by its governing equations that are not differential and can incorporate reversal points like the FORC [24] method. Despite its relative simplicity and proposed versatility, this model has not found many applications. Outside of Włodarski's own papers, [7], [8], it appears in one publication for modelling a transformer core's hysteresis by deep neural network computations [25].

The governing equation for magnetization as a function of the applied H field, is a loop specified by the reversal point H_r, the maximum field strength H_m, and the coercivity parameter, c. For a symmetric hysteresis loop, which is the most common application, the reversal point is the same as the field maximum, ($H_r = H_m$). This main equation has the form;

$$\begin{aligned} M(H, H_r, H_m, c) = M_{12}(H_m, H_r, c) \pm A\left[F\left(\frac{H+c}{b}\right) - F\left(\frac{H_r+c}{b}\right)\right] \\ \times\left[F\left(\frac{H-c}{b}\right) - F\left(\frac{H_r-c}{b}\right)\right], \end{aligned} \tag{2.2.2}$$

where $M_{12}(H_m, H_r, c)$ is the magnetization constant for the given reversal point and loop tip, A is a scaling and shaping factor for the rest of the equation, b and c are two of the model parameters and F is the odd function chosen to best fit the material's behaviour. For most ferromagnetic material, the Langevin function [26], is selected. This model is further described in Section 4, where it is used to model hysteresis loops for 300M, AISI 4340 and HY80 steel samples.

2.3 Domain theory

In ferromagnetic and ferrimagnetic materials, the atomic magnetic moments spontaneously align (or anti-align, as in the case of ferrimagnetic material) into small sub-volumes called domains. These domains have a uniform magnetization at saturation. They form when the material cools below its Curie temperature ($T_c = 770$ °C for iron) and the atoms get close enough to be influenced by their neighbour's electron spins, known in quantum mechanics as spin exchange interaction [16]. Above that temperature, the material is paramagnetic and does not order itself into domains, since the thermal energy is stronger than that of neighbouring atoms. This theory of paramagnetism is credited to Langevin and the spontaneous magnetization of domains for ferromagnetic materials is credited to Weiss [27] in 1907.

The discovery of Barkhausen noise [28] supported domain theory. Then in the 1930's, magnetic domains were observed directly under a microscope [29]. This was done by placing magnetic powder on the polished surface of a ferromagnetic crystal, known as the Bitter method [30]. Later, an experiment by Williams *et al.* [31] demonstrated the movement of domains of a single Si-Fe crystal in the form of a hollow rectangle, like a picture frame, due to a low alternating magnetic field.

The bulk magnetization, $\vec{M}$, of the material is the vector sum of the magnetization in these domains. The transition zone between different domains is called a domain wall. For steel or iron, which has a Body-Centred Cubic (BCC) structure, there are two types of walls; 90°and 180°domain walls, named after the degree of magnetic vector transition across them. The configuration of these domains, size, orientation, number and thickness

of the walls, is the result of a balance of magnetic energies.

2.3.1 Magnetic Energies

Magnetic domains form to minimize internal energy [16]. There are four basic energies involved in ferromagnetism, which influence domain formation; exchange energy, magnetostriction (or magneto-elastic energy), magneto-static energy and anisotropic energy [16],[18], [32].

Exchange energy (E_{ex}) is the quantum-mechanical exchange force at the molecular scale, which aligns adjacent electron spins, and is minimized when atomic dipole moments are parallel for ferromagnetic materials such as iron, cobalt and nickel [33]. These elements have a positive exchange interaction, whereas antiferromagnetic elements such as manganese and chromium, minimize this energy when their electrons have antiparallel moment arrangements, which is a negative exchange interaction [11]. The Bethe-Slater curve shows the variation in exchange energy as a function of the ratio of interatomic distance (a) to the radius (r) of the unfilled electron shell as shown in Figure 2.4.

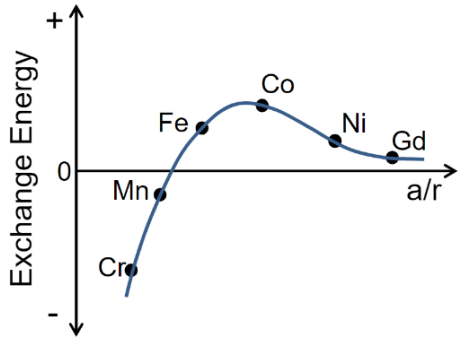

Figure 2.4: Bethe-Slater curve: exchange energy for increasing ratio of interatomic distance (a) to electron shell radius (r) [32].

Exchange energy is calculated by considering the interaction between two atoms at lattice sites i and j, and is given by [11] :

$$E_{ex} = -J_{ex}\vec{S_i} \cdot \vec{S_j} = -2J_{ex}S_iS_jcos\phi \ , \tag{2.3.1}$$

where J_{ex} is the exchange integral representing the strength of the overlap of charge distribution between the atoms. This integral is strongest for neighbouring atoms and is dependent on temperature, and so for atoms that are far apart, J_{ex} is taken to be zero. ϕ is the angle between the atoms' spins and $\vec{S_i}$ and $\vec{S_j}$ are the spin vectors, which have a magnitude of $\pm 1/2$ under the assumption of the Ising model [30]. Equation 2.3.1 applies to all matter, with any orientation of S, and is also called the Heisenberg model [34].

Anisotropic energy (E_κ), relates to the preferred directions of the magneto-crystalline structure called the "easy" axis of magnetization. Iron has a body-centered-cubic (BCC) crystalline structure, which has an "easy" axis along the cube's edges [001] or [100], a "medium" axis diagonal across the cube face [110] or [011] and a "hard" axis through the center [111], as shown in Figure 2.5 a), with relative magnetization curves in Figure 2.5 b). The equation for anisotropic energy is related to the strength of the anisotropy with respect to the easy axis directions [11]:

$$E_\kappa = \kappa_0 + \kappa_1(\alpha_1^2\alpha_2^2 + \alpha_2^2\alpha_3^2 + \alpha_1^2\alpha_3^2) + \kappa_2(\alpha_1^2\alpha_2^2\alpha_3^2) + ... \tag{2.3.2}$$

where $\kappa_0, \kappa_1, \kappa_2$ etc. are the magneto-crystalline anisotropy coefficients for the material at a given temperature, α are direction cosines relative to the easy axis directions, as indicated by the subscripts 1, 2, and 3. The first term, κ_0, is independent of angle and is usually neglected from the equation [32]. The coefficients increase as temperature decreases below T_c and κ_1 is much larger than κ_2 so additional coefficients are neglected.

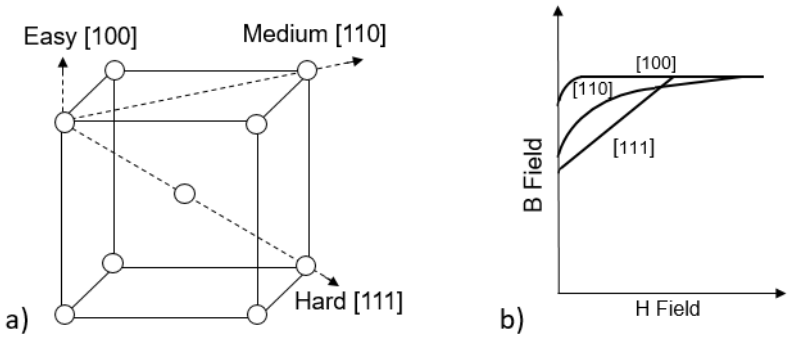

Figure 2.5: a) The three anisotropic axis of a single BCC iron crystal and b) associated magnetization curves (adapted from [17]).

The width of domain walls is the result of the balance of exchange energy and anisotropic energy. The exchange energy strives to increase the domain wall width so as to reduce the angle between neighbouring electron spins, whereas anisotropic energy aims to reduce the amount of magnetization in non-easy axis directions. The resulting width of the magnetic domain wall, through which the spins are rotated 180°, is around 300 atoms wide for iron [32]. The sum of these energies is also called **domain wall energy** and the number of domain walls can change to accommodate stresses present in the material [18].

Magnetostriction, λ, is the term for strain induced changes in magnetization due to the relationship between exchange energy and magnetic energy [18].

$$\lambda = \frac{\Delta l}{l} \quad and \quad \lambda_t = -\frac{1}{2}\lambda \ , \tag{2.3.3}$$

where l is the length, Δl is the change in length and λ_t is the transverse strain perpendicular to the applied magnetic field, which, for most ferromagnetic materials, is approximately $1/2\lambda$ in the opposite direction. Note, λ is used for magnetostriction strain to differentiate it from mechanical strain, ϵ. Either form of strain will change the ratio of interatomic distances and therefore, the level of exchange energy (Figure 2.4) which, in turn, affects the material's magnetic response. Similarly, an external magnetic field will cause the material's crystalline structure to strain or constrict in response to the magnetic energy [16].

Positive magnetostriction is when the material elongates in the direction of the applied magnetic field, as is the case for iron, and negative magnetostriction is when the material contracts along the applied magnetic field, as is the case for nickel [33]. Figure 2.6 shows positive magnetostriction in the direction of an applied H field. Magneto-elastic energy encompasses magnetostriction, since this energy relates to strain, ϵ, and, its effects on the crystalline structure of the atoms in the magnetic material [33].

Anisotropy affects magnetostrictive strain so the variable is often denoted with a subscript for the crystalline direction it is measured in; λ_{100}, λ_{110}, and λ_{111}, denoted by the anisotropic axes shown in Figure 2.5. In polycrystalline structures, such as steel, the "easy" axis [100] refers to the direction parallel to the 180° domains and the "hard" axis [111] is perpendicular to them [17].

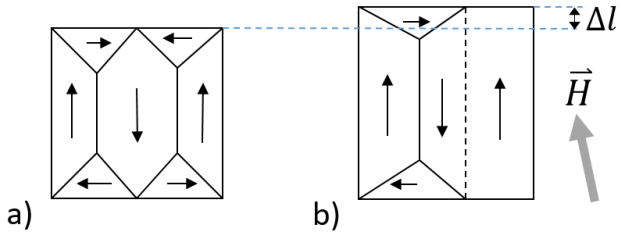

Figure 2.6: Magnetostriction with magnetic object model of iron crystal a) without H field, and b) with H field causing domain wall movement and elongation.

The saturation magnetostriction λ_s that is in the same direction as the applied magnetic field is given by [11]:

$$\lambda_s = \frac{3}{2}\lambda_{100}(\alpha_1^4 + \alpha_2^4 + \alpha_3^4 - \frac{1}{3}) + 3\lambda_{111}(\alpha_1^2\alpha_2^2 + \alpha_2^2\alpha_3^2 + \alpha_1^2\alpha_3^2) \ , \tag{2.3.4}$$

where α are directional cosines between the applied magnetization and the easy axis directions, which are the same as the ones for the anisotropic energy equation.

Magneto-static energy is the energy of a finite body associated with free poles at a surface [16]. Magneto-static energy is non-zero when magnetization is either non-uniform ($\nabla \vec{M} \neq 0$) and/or there is a normal component of magnetization ($\vec{n} \cdot \vec{M} \neq 0$), both of which strongly depend on the geometry of the finite body [16]. This energy is minimized when the material's magnetization is closed and external fields are reduced.

There are two sources of magneto-static energy; from the self-magnetization of a permanent magnet and from the internal demagnetization field, $\vec{H}_d$ [11]. In both cases, the magneto-static energy opposes an applied magnetic field, $\vec{H}$, it resists change and is proportional to $\vec{H}$. This section focuses on the second type, where the effective field, $\vec{H_{eff}}$ through the material is the difference between the applied $\vec{H}$ field and the demagnetization $\vec{H}_d$ field.

$$\begin{aligned} \vec{H}_{eff} &= \vec{H} - \vec{H}_d \\ \text{where} \quad \vec{H}_d &= N_d \vec{M} \ , \end{aligned} \tag{2.3.5}$$

where N_d is the demagnetization factor, which ranges from 0 to 1 and depends on shape of the material being magnetized [11]. To calculate this factor, consider an infinitely long

plate with length $L \sim \infty$ and thickness t and a field applied through the plate H, as shown in Figure 2.7 a). Apply Equation 2.1.1 $\nabla \cdot \vec{B} = 0$ for a surface integral of a plate with a normal component of $\vec{H}_n$ over a region S [30].

$$\begin{aligned} \iint \vec{H}_n \cdot d\vec{S} &= m \ , \\ H_d \, S = MS \quad or \quad \vec{H}_d &= \vec{M} \ , \end{aligned} \tag{2.3.6}$$

where m is the magnetization element on the surface. Assuming the magnetic field H is constant and uniform across the plate, and the length is significantly larger than the thickness, then the demagnetization factor is $N_d = 1$ [12]. Alternatively, if the field is applied along the length of the plate, as shown in Figure 2.7 b), then the demagnetization field and factor will be zero ($H_d = 0, \ N_d = 0$) because the surface effect on the ends is negligible.

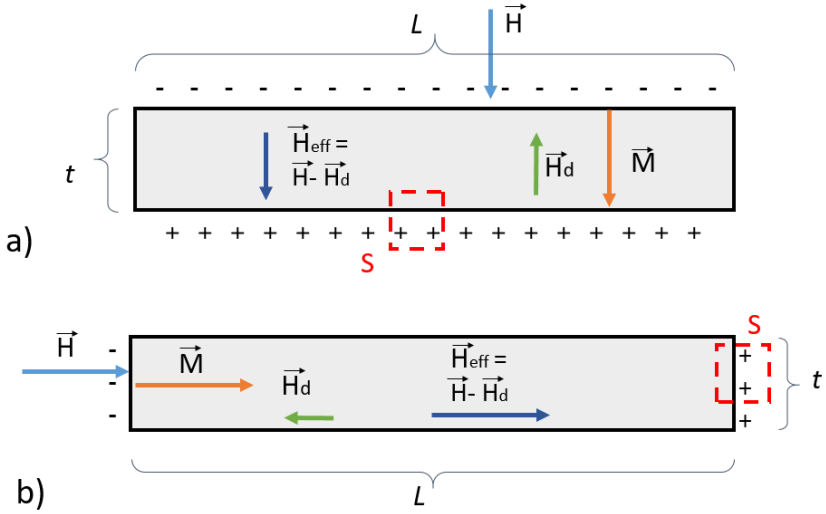

Figure 2.7: Infinitely long plate with $\vec{H}$ field applied a) perpendicular and b) parallel to the plate (adapted from [30]).

The magneto-static energy E_{ms} is calculated as the volumetric integral of the magnetization field H_d, which can be written in terms of applied magnetic field using Equation 2.3.5 as [16, 30]:

$$E_{ms} = \frac{1}{2} \int H_d^2 dv = -\frac{1}{2} N_d \cdot M^2 \ , \tag{2.3.7}$$

To reduce this energy, ferromagnetic materials divide themselves into fully saturated magnetic domains, where the smaller the domain, the smaller the external magnetic field ($M =$

M_s) [11, 16, 30, 32]. But there is energy associated with the creation of domain walls due to the presence of the other magnetic energies; exchange energy, magnetostriciton and anisotropic energy. The formation of magnetic domains with minimum energy is illustrated with the use of the Magnetic Object model (MO) model, as previously shown in Figure 2.8.

2.4 Magnetic object model

Magnetic domain structure is a result of the interaction and minimization of the four main energy states. To understand these interactions, the magnetic object (MO) model can be used, which contains one or more 180° domain walls, as previously shown in Figure 2.8. The MO takes a volume of a single grain or crystal of the material that has uniform magnetic properties, i.e., the same easy axis along which the 180° magnetic domains lie [18]. Figure 2.8 shows a flux-closed configuration, which minimizes the total energy within the structure as the sum of exchange (E_{ex}), crystallographic anisotropy (E_k), magnetostrictive (E_σ), and magneto-static (E_{ms}) energies [18, 32].

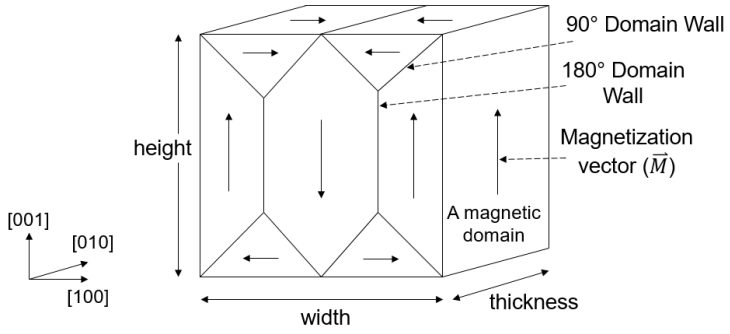

Figure 2.8: 180°and 90°domain walls indicated on a magnetic object for a single crystal of iron with the easy axis defined by the crystallographic [100] direction (adapted from [18]).

Under an applied magnetic field, H, the magnetic domains change size in response to the increasing flux density, B, in the material, as shown in Figure 2.9 [32].

The reversible stage i) is when the MO is first subjected to the magnetic field and is demagnetized with a flux-closed domain structure. The next stage ii) is the irreversible growth of the 180° domains most closely aligned with the applied field. These domains

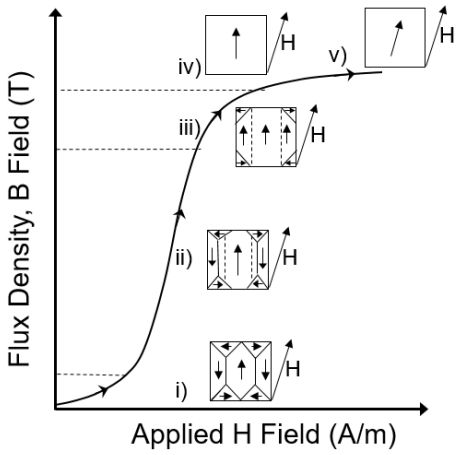

Figure 2.9: The behaviour of domains in a ferromagnetic material during initial magnetization (adapted from [32]).

grow first, since they make the dominant contribution to magnetization. The magnetization slows down with the movement of the 90° domain walls, at the knee of the curve iii), since those domains have less magnetic contribution to balance the applied magnetic field. Once the MO has a single domain iv), it rotates to align with the applied field, and saturation v) is reached [32]. When the direction of the applied field is reversed, it creates a magnetic hysteresis loop, which is used to produce and measure MBN.

2.5 Magnetic Barkhausen Noise

Barkhausen noise is primarily associated with irreversible magnetization transitions within the material, where 180°magnetic domain walls (DWs) are abruptly moving from one pinning site to another in an energy landscape [18]. Pinning sites are locations of lower energy such as a defect, grain boundary or impurity [35]. Therefore, it takes additional energy to overcome the barrier and jump to the next place of lowest energy level within the MO. Figure 2.10 gives an example of a hypothetical energy landscape, where a DW moves from pinning site 1 to 2 in response to the H field, while the DW pinned on site 3 doesn't have enough energy to move.

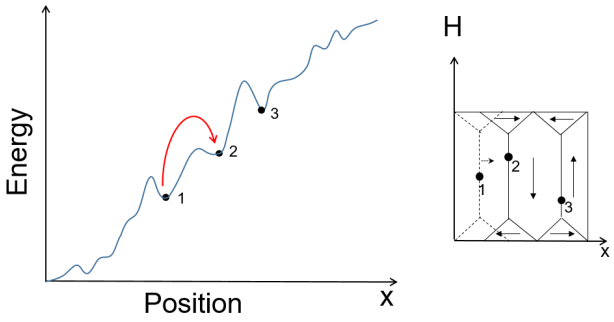

Figure 2.10: Motion of domain walls through energy landscape (adapted from [18]).

These abrupt DW movements cause changes in the material's magnetization or magnetic flux $\frac{d\Phi}{dt}$ with time. A pick-up coil placed near the area of the material being magnetized can read a voltage induced by the changing flux according to Faraday's law, as previously shown in 2.1.5 [32]. The signal is retrieved through the pickup coil at a frequency of 100 Hz to 300 kHz. It is then passed through a high pass filter and amplified to separate it from background noise.

The MBN signals are concentrated in two bursts per magnetization cycle, or hysteresis loop, which occur around the coercive points for the material, as shown in Figure 2.11.

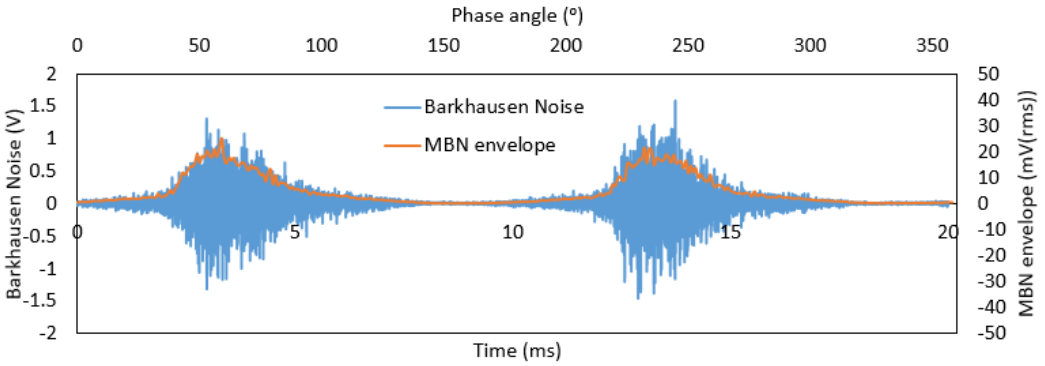

Figure 2.11: Barkhausen noise and envelope response for a 300M steel sample due to a 0.8 T field alternating at 50 Hz.

The signals are translated to positive values by evaluation of Root-Mean-Squared (RMS) voltage. The RMS is integrated over short time intervals to produce positive curves called MBN envelopes with units mVrms. Figure 2.11 shows the pick-up coil response in blue

for Barkhausen noise events as a function of time and the MBN envelopes in orange as a function of phase angle, due to a magnetic field alternating at 50 Hz.

Magnetic Barkhausen noise energy (MBN energy) is calculated by taking the integral of this voltage squared signal over time, dt, of one cycle [36]:

$$MBN_{energy} = \int V^2 dt, \tag{2.5.1}$$

The resulting MBN energy is in units of $(\text{mV})^2\text{s}$. It is understood that $(\text{mV})^2\text{s}$ isn't units of energy (Joules) but it is proportional to energy, as there is an effective resistance constant that is ignored [32].

2.5.1 MBN and stress

Stress is defined as a force per unit area. For crystalline materials, such as steel, these forces act in three dimensions, expressed as a Cauchy stress tensor, $\vec{\sigma}$, with principle stresses along the x, y and z axes [37]:

$$\vec{\sigma} = \begin{bmatrix} \sigma_{xx} & \sigma_{xy} & \sigma_{xz} \\ \sigma_{yx} & \sigma_{yy} & \sigma_{yz} \\ \sigma_{zx} & \sigma_{zy} & \sigma_{zz} \end{bmatrix}. \tag{2.5.2}$$

In the same way, strain, $\vec{\epsilon}$, is a tensor. This research applies stress by bending rectangular samples so that it is uniaxial; only applied in along the x axis. For this reason stress and strain can be simplified to $\sigma_{xx} = \sigma$ and $\epsilon_{xx} = \epsilon$, respectively, and will here on, be referred to by these magnitudes.

A relationship between mechanical stress and magnetic characteristics was first observed by Joule [38] in 1841, when he described the lengthening of a steel bar under an applied magnetic field. Then in 1865, Villari [39], observed the inverse, a bar lengthened by tension would change its magnetic properties, which came to be known as Villari reversal [17]. This was later combined with magnetic domain theory and the balance of energies including applied and residual stress.

From the balance of magnetic energies perspective, mechanical stress comes hand in hand with strain, be it from spontaneous magnetostriction, field-induced magnetostriction

or mechanical applied force. Assessing the stress experienced by a volume of material is called the inverse effect of magnetostriction and it plays an important role in determining the domain structures in an attempt to reduce this energy [30]. To calculate magnetostrictive energy E_σ, we consider an applied stress σ and include it in Equation 2.3.4:

$$E_\sigma = -\frac{3}{2}\lambda_{100}\sigma(\alpha_1^2\gamma_1^2+\alpha_2^2\gamma_2^2+\alpha_3^2\gamma_3^2-\frac{1}{3})-3\lambda_{111}\sigma(\alpha_1\alpha_2\gamma_1\gamma_2+\alpha_2\alpha_3\gamma_2\gamma_3+\alpha_1\alpha_3\gamma_1\gamma_3) \tag{2.5.3}$$

where the γ_i are the directional cosines of the stress tensor with respect to the easy axis. For iron, magnetostriction is isotropic meaning that $\lambda_{100} = \lambda_{111} = \lambda_s$ [32], so Equation 2.5.3 can be simplified to:

$$E_\sigma = -\frac{3}{2}\lambda_s\sigma\cos^2\theta \quad \text{where} \quad \cos\theta = \frac{1}{\sqrt{3}}(\gamma_1+\gamma_2+\gamma_3) \tag{2.5.4}$$

where θ is the angle between the direction of magnetization and easy axis, but also holds true for describing the angle between the magnetization and the stress σ, since isotropic magnetostriction is assumed.

These magnetic changes due to stress influence Magnetic Barkhausen noise (MBN), which has given this phenomenon an application for Non-Destructive Evaluation (NDE) for residual stress measurement. Residual stress is the internal stress that remains in a material after plastic deformation and once the applied stress has been removed [40]. Tensile stress or strain has been shown to cause large changes in MBN responses for ferromagnetic material [41]. This phenomenon has been researched for applications with pipeline steel [42], [43], submarine steel [44, 45], tool steel [46], electrical steel [47, 48], pressure vessels [49] and aircraft landing gear [36]. Since stress effects domain configuration and MBN arises from the movement of magnetic domain walls, a relationship can be inferred to be present between MBN signals and stress [32].

3 Experimental equipment and materials

This section covers the experimental equipment, instruments, and samples used in the experiments. The portable MBN system is used in all three experiments to take MBN measurements of the samples in elastic and plastic bending experiments, as well as apply the time-varying magnetic field to the samples for the hysteresis plot experiment. The four-point bending apparatus applies bending loads to the sample and houses the MBN probes from the portable system. The bending stress is confirmed by strain gauge equipped samples under four-point bending. Once the samples are bent, the deformed profile is measured by a precision gauge attached to a milling machine. The hysteresis plots or BH curves are measured with a U-core probe, an encircle coil and Hall sensors set up.

The materials tested in these experiments are 300M, American Iron and Steel Institute (AISI) 4340 and HY80 steel. The sample materials section covers the dimensions, mechanical and magnetic properties of the samples, as well as Scanning Electron Microscope (SEM) images of their surface microstructure. Samples' skin depth calculations were done for different frequencies of H field and MBN signal using conductivity measurements and magnetic permeability values derived from the hysteresis curve experiments. The section concludes with a simple test to show the samples' magnetic anisotropy by taking MBN readings along longitudinal and transverse orientations on the samples.

3.1 Experimental instruments and equipment

3.1.1 Portable MBN system

A MBN measurement system has three main components [50]; the excitation circuit, which applies the magnetic field through a U-core electromagnet probe, a pick-up (or inductive) coil, and an RMS amplifier circuit to measure MBN and send it to a computer. The system used for this research has an additional feature, which allows for flux control of the excitation circuit by way of feedback coils [51]. Figure 3.1 shows a schematic for the system used to take MBN measurements and Figure 3.2 shows the equipment set up.

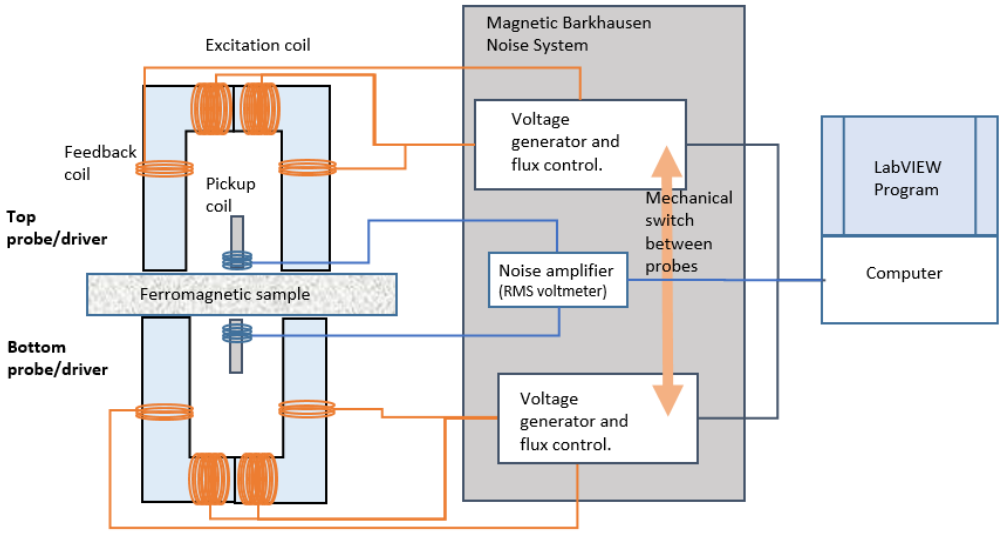

Figure 3.1: System for MBN measurements.

The MBN signal, as mV, is retrieved through the pickup coil, by Equation 2.1.6, at a frequency of 1 kHz - 300 kHz, with most of the signal ocuring at 200 kHz [10], at a sampling rate of 200 MHz. It is then passed through a high pass filter of 500 kHz to separate it from background noise. The system converts it to MBN energy by the time integrated square RMS voltage over several magnetization cycles [45] as shown previously in Equation 2.5.1, then amplifies it by 500 times. The system runs twenty cycles for each measurement but discards the first four cycles to allow for stabilization before integrating over the last sixteen. This signal is compared to the phase of the excitation signal, to show

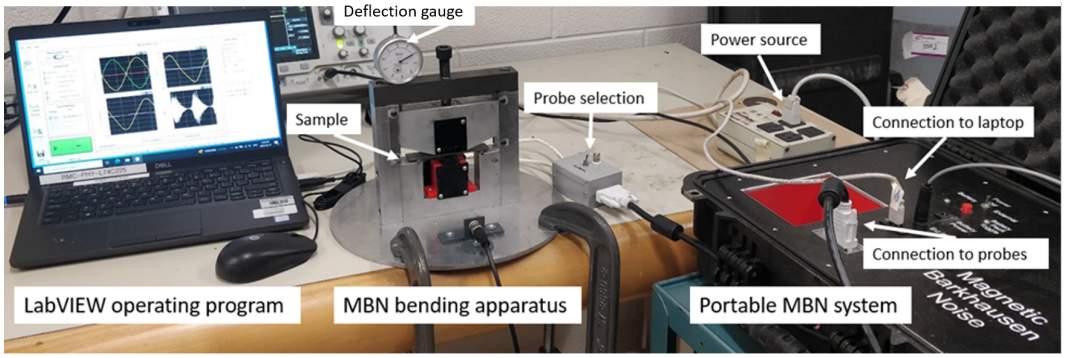

Figure 3.2: MBN system and bending apparatus.

how quickly the material is magnetized.

The top and bottom MBN probes were built to be as similar as possible to allow for measurements on the top and bottom of the sample while in bending. The U-core is made of Supermendur, a vanadium iron cobalt laminated alloy [52], a highly permeable material for maximum magnetic flux density transfer. It was purchased pre-formed in a U, which was cut in the center to position the excitation coils, then butted back together to make the probe. The excitation coil has 500 turns total, 250 turns wired in parallel on each half of the U-core, and the feedback coil has 200 turns total, with two coils of 100 turns wired in series on each arm, or pole, of the probe. The pickup coil is located between the poles and is a commercial component with an inductance of 15 micro-Henri. These probe characteristics are summarized in Table 3.1.

Table 3.1: MBN probe components

Component	Characteristic	Value
U-core	cross-sectional area	$9.6 \times 3.8 = 36.4$ mm^2
Excitation coil	turns	250 + 250 = 500
Feedback coils	turns	100 + 100 = 200
Pickup coil	inductance	15 μH

3.1.2 MBN bending apparatus

The experimental equipment is a four-point bending apparatus, as shown in Figure 3.3 with Barkhausen measurement probes on the top and bottom of the sample to take readings from

the side in compression and tension, respectively. The dial on the top of the rig measures the deflection in millimeters and the center screw pushes the two center points down causing the bending. The probes each consist of a magnetization yoke made from a Supermendur (vanadium-iron-cobalt alloy [52]) U-core, excitation coils also called driver coil, feedback coils on either arm of the U-core and a pickup coil between the poles.

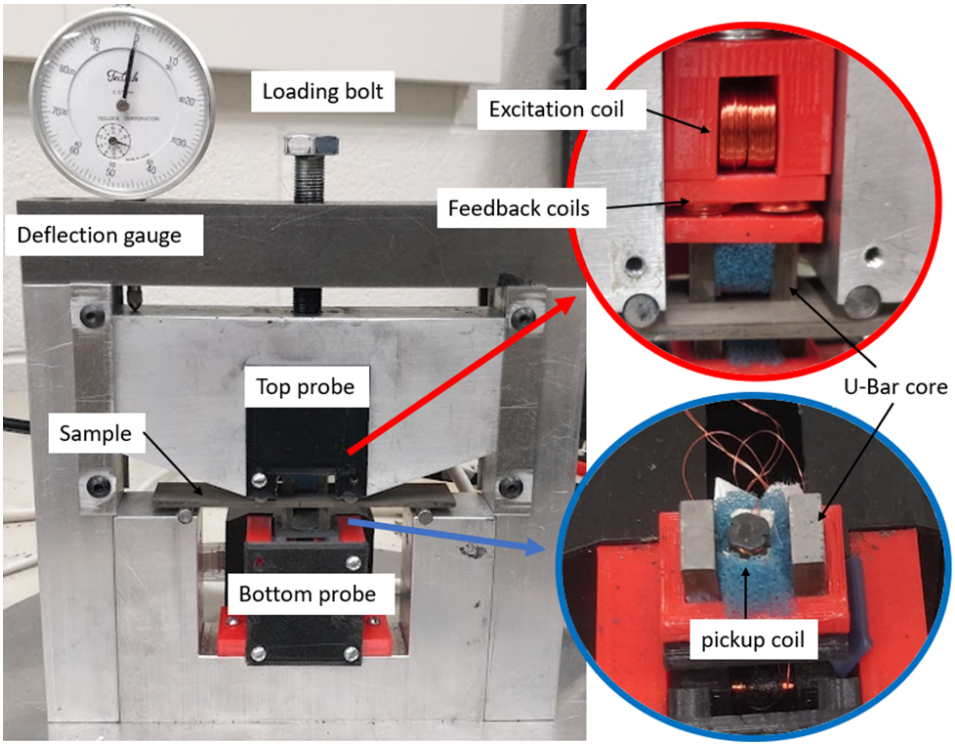

Figure 3.3: Sample in the MBN bending apparatus between top and bottom MBN probes.

Four-point bending was chosen as the method to apply stress to the sample because the region between the two center contact points has a constant bending moment, in the elastic regime, where the probes are located. With the four-point bending apparatus, compression occurs on the top surface of the sample and tension at the bottom. Figure 3.4 shows the moment and bending diagram for a sample in the bending apparatus from the front-on view. The distance between the bottom contact pins, A and D is $L = 80$ mm and the distance between the center loading pins, D and C is 30 mm. When the sample is permanently deformed and the bending load is released, residual stress is present with tension on the top

(concave surface) and compression on the bottom (convex surface).

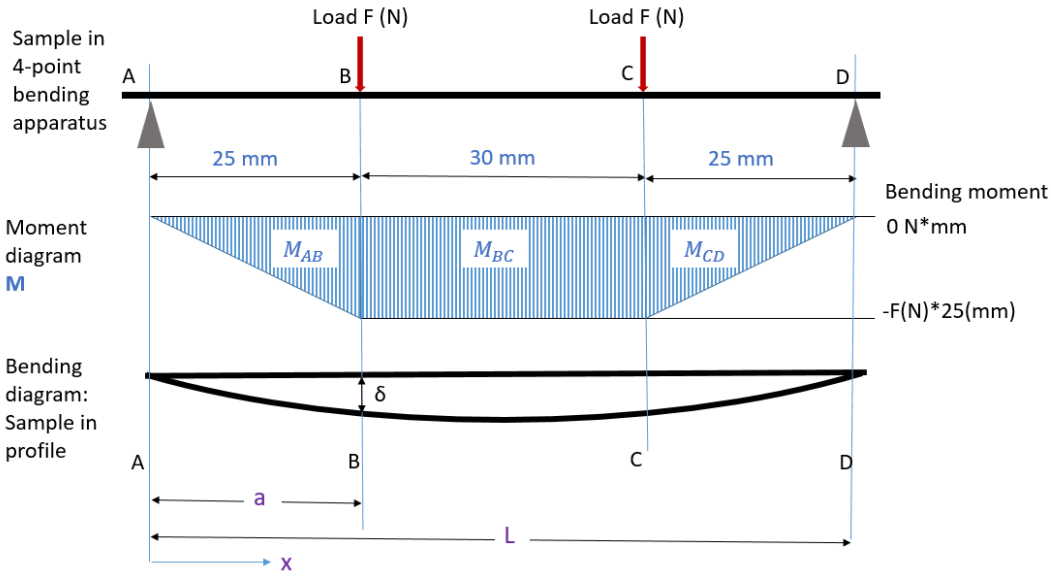

Figure 3.4: Profile view of bending apparatus, moment diagram and bending diagram.

To conduct the elastic and plastic bending experiments, the sample is placed and centered in the bending apparatus, as shown in Figure 3.3. The loading bolt is adjusted until the top pins come into contact with the sample, then the deflection gauge is zeroed. Ensuring that the MBN probes are making good contact with the top and bottom surfaces of the sample, measurements can be taken with the MBN system, operated from the LabVIEW program. The sample bending load is incremented by deflection between the top and bottom contact pins, as read from the deflection gauge. Bending stress calculations for the elastic regime are performed prior to the experiment to determine these increments.

The **stress analysis** for the bending apparatus is presented in Appendix B and summarized below. In the elastic regime, stress, σ has a linear relationship with strain, ϵ, by way of the modulus of elasticity (or Young's modulus) E [53].

$$\sigma = E\epsilon \ . \tag{3.1.1}$$

Stress is defined as force per unit area, positive for tension and negative for compression. Strain is the change in length divided by the original length. Mechanical strain ϵ is defined

the same as magnetostrictive strain λ, as shown in Equation 2.3.3.

The yield point between elastic and plastic stress is defined as the intersection of the stress strain curve and a parallel slope beginning at $\epsilon = 0.2\%$ [53]. The plastic regime no longer has a linear relationship with strain. When the bending load is removed, residual stress remains in the sample due to plastic deformation. This stress analysis section focuses on elastic bending only.

Stress is force per unit area and in bending, this force is acted over a distance, so the moment must be calculated. Referring to Figure 3.4, the moment diagram shows that the moment is 0 at points A and D, since the beam is simply supported there. Between points B and C, the moment, M_{BC} is constant and at its maximum. This value can be calculated for the distance $x = a = 25$ mm for the contact point B:

$$M_{BC} = F \times a = F \times 25\,\text{mm} \quad \text{for } B \leq x \leq C, \tag{3.1.2}$$

where F is the applied force or load.

From the moment equation, stress is given as a function of the height or y coordinate across the thickness of the sample, with the maximum tension and compression at the bottom and top surfaces of the sample. If the center of the sample is the neutral axis (zero stress) $y = 0$ and the surfaces are half the thickness, c, then the maximum stress is given at the surfaces $y = \pm c$ as:

$$\sigma_{max} = \frac{M_{BC} \times c}{I_z}\ , \tag{3.1.3}$$

where I_z is the second moment of inertia about the z axis for the sample, calculated as a rectangular beam.

The stress exerted on the samples is controlled by bending deflection, as read from the deflection gauge shown in Figure 3.3. For the bending apparatus configuration, shown in Figure 3.4, the deflection, δ_a, measured at point B ($x = a$), where the deflection gauge measures, is given by [54]:

$$\delta_a = -\frac{M_{BC}}{6EI_z}\left(3La - 4a^2\right), \tag{3.1.4}$$

where a is the distance, 25 mm, between points A and B, and L is the length, 80 mm, between the outer contacts, point A and D, as shown in Figure 3.4.

Once the deflection produces a strain that results in a stress exceeding the yield point, residual stress is calculated based on the strain gauge measurements and the theoretical height of the plastic zone through the thickness. Residual stress can also be derived from the deflection profile of the bent sample by radius of curvature measurements. Both methods are discussed under plastic deformation in Appendix B.

3.1.3 Strain measuring equipment

A strain gauge was attached to one sample of each material in order to measure bending strain in the MBN bending apparatus. These measurements were used to confirm the bending calculation and assess the material's mechanical behaviour. The strain gauges used were from Micro-Measurements [55] and had a gauge factor of 2.115 $\pm 5\%$. The instrument used to take the strain measurements was a P-3500 Strain indicator, by Vishay Measurements Group, the same company that made the gauges.

To use the strain gauged samples, the bottom MBN probe needs to be removed from the apparatus. The gauge leads are then connected to the strain indicator following the instructions on the instrument's lid for a half Wheatstone bridge configuration. Once zeroed, the sample is placed in the bending apparatus with the gauge side down, as shown in Figure 3.5. It can then be subjected to the desired bending increments and MBN response can be measured with the top probe. The indicator reads micro strain ($\times 10^{-6}\%$), which needs to be manually recorded, since the indicator does not output to a computer.

3.1.4 Bent sample profile measurements

After the plastic bending experiment is conducted, the bent samples' profile is measured to determine the radius of curvature and residual strain. This was conducted with a milling machine mounted with a pressure sensitive position gauge. The sample was clamped into

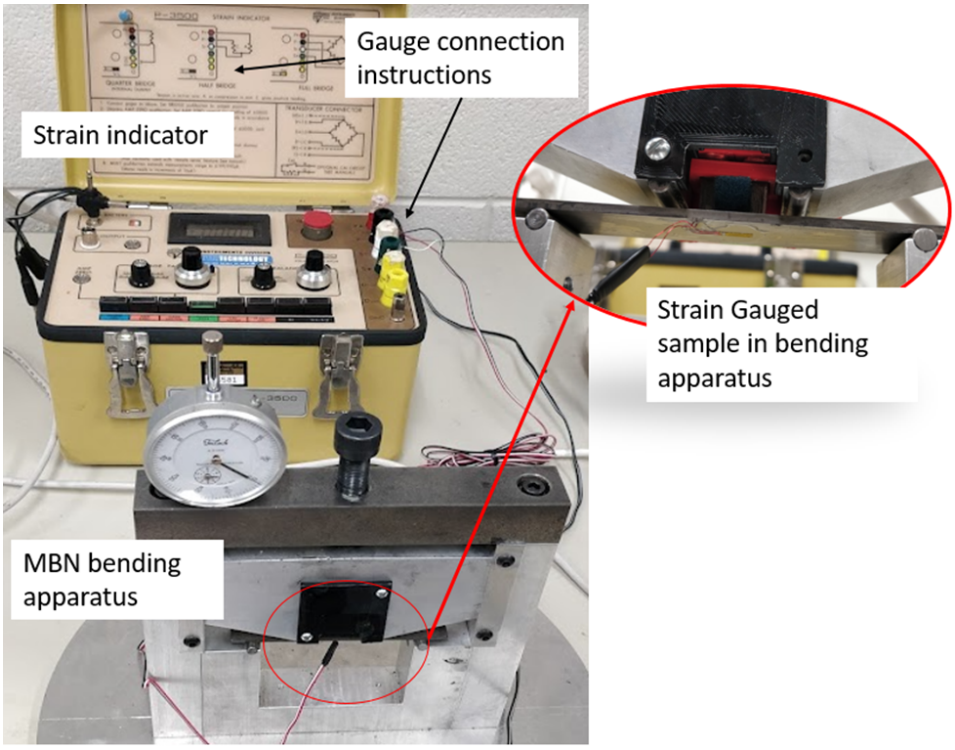

Figure 3.5: Experimental set up for strain gauged sample the bending apparatus.

the milling machine's surface with the convex (bottom) surface up and the position gauge measured the surface's height along the length, as shown in Figure 3.6.

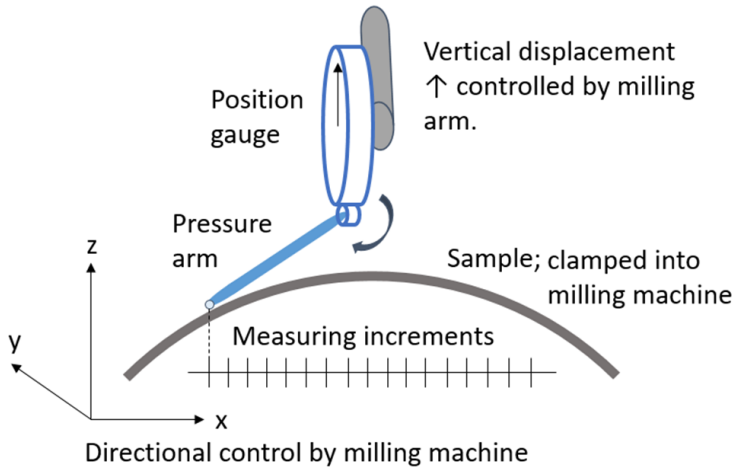

Figure 3.6: Bent sample curvature measuring experimental set up.

These height measurements of the convex surface of the sample at equal increments gave the bent profile. This curvature could then be used to plot the deflection and work backwards through the plastic stress calculations to estimate the residual stress, as described in Appendix B.

3.1.5 Hysteresis plots; BH Curve measurements

The magnetic hysteresis or B versus H field curves are plotted by sensing the magnetic flux density, B field, through a sample subjected to a known applied H field. The experimental equipment and set up with a sample are shown in Figure 3.7. An H field is applied to the sample by a U-core magnet with the same design as the Magnetic Barkhausen noise (MBN) probe. The core is made of Supermendur, which magnetizes easily due to its high permeability, up to $\mu_r = 6.6 \times 10^4$ [52]. An alternating magnetic field is generated in the core from the excitement coil that is controlled by the portable MBN system with an input voltage. A feedback coil is shown on the U-core in Figure 3.7, but it is not used during the experiment, which is simply voltage controlled.

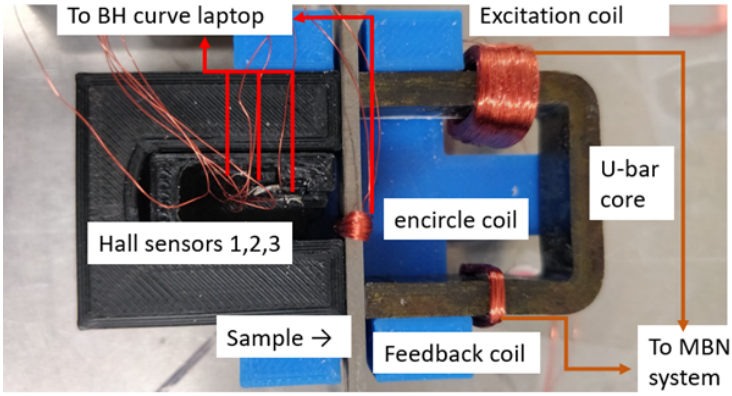

Figure 3.7: Experimental setup for measuring the BH curve of a sample.

To take BH curve measurements, the sample is placed in the apparatus jig between the core and the hall sensors with the encircle coil wrapped around it and clamped in place to ensure good contact between the surfaces, as shown in Figure 3.7. There are three Hall sensors, Allegro model A1321 [56], positioned parallel to the surface of the sample at lift

off distances of 1.5 mm, 4.5 mm and 7.5 mm. Their sensitivity factor is 1.59×10^4 (A/m)/V [56].

The Hall sensors measure H field strength, which is extrapolated linearly through air back to the sample, and boundary conditions dictate that the parallel component of the H field is continuous into the surface of the sample [12]. The B field is measured by the encircle coil around the sample using Faraday's Law (Equation 2.1.1). Both field responses are received by a LabVIEW program, which, along with inputs for the sample's cross-sectional area, allows it to generates the BH curve, for each measurement.

The labView program, named BH Timed V2.vi, takes the user inputs for the cross-sectional area of the sample, the frequency (2 Hz), and an input voltage from 1-10 V. The program then uses the MBN system to run the excitation coil for 20 magnetization cycles. The first four cycles are discarded, to allow the system to stabilize, then the last 16 cycles are averaged and smoothed using the Savisky-Golay filter, to produce the hysteresis loop. The applied H field is controlled by the input voltage, since flux control (and the feedback coil) is not an option with this system. A minimum of eight BH curve measurements and various input voltages should be taken to create a family of nested hysteresis loops, which are then copy pasted into Excel for analysis.

3.2 Sample materials

Three types of high strength steel samples were used for these experiments. The primary sample material was 300M, aircraft landing gear steel. Two others were tested for comparison purposes; AISI 4340; the non-heat treated version of 300M and HY80; a submarine hull steel. Typical samples are shown in Figure 3.8. Material properties and composition of these steels are summarized in Table 3.2.

The sample material was cut into pieces, 9 total samples of 300M and 5 samples of each AISI 4340 and HY80, with the dimensions shown in Table 3.3. One of each sample was cut lengthwise to provide a narrower sample for the hysteresis plots experiment, as shown in the second Dimensions column. The uncertainty in the caliper measurements

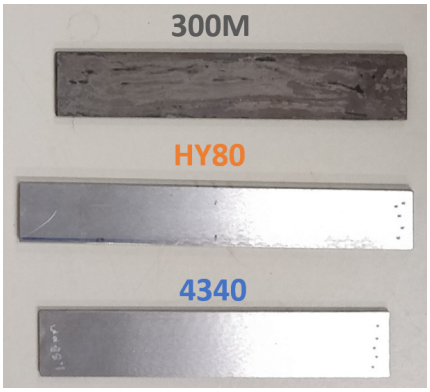

Figure 3.8: Samples 300M, HY80 and AISI 4340.

Table 3.2: Material properties for steel samples.

Material	**Composition (% wt)**	**Yield Strength**	**Modulus of Elasticity**	**Source**
AISI 4340	0.4% C, 0.8% Cr, 0.7% Mn, 0.25% Mo, 1.8% Ni	Annealed 470 MPa	200 GPa	[57]
300M	0.4% C, 0.8% Cr, 0.7% Mn, 0.25% Mo, 1.8% Ni	1500 MPa	205 GPa	[58]
HY80	0.15% C, 1.7% Cr, 0.25% Mn, 0.6% Mo, 3.25% Ni	570 MPa	205 GPa	[57],[36], [45]

was approximately 0.1 mm for the length and width and 0.05 mm for the thickness, which results in a ± 5 to 6% uncertainty in the area and volume calculations for the samples.

Table 3.3: Sample dimensions for the bending and BH curve experiments.

Material	**# of samples**	**Dimensions (mm^3)**	**Dimensions BH curve (mm^3)**	**Uncertainty (mm$\times$ mm$\times$ mm)**
300M	9	$102 \times 19 \times 2.0$	$102 \times 9.63 \times 2.06$	$0.1 \times 0.1 \times 0.05 = \pm 6\%$
		$102 \times 19 \times 2.2$		$0.1 \times 0.1 \times 0.05 = \pm 5\%$
AISI 4340	5	$102 \times 19 \times 2.0$	$102 \times 9.66 \times 2.02$	$0.1 \times 0.1 \times 0.05 = \pm 6\%$
HY80	5	$114 \times 17 \times 2.8$	$114 \times 9.63 \times 2.81$	$0.1 \times 0.1 \times 0.05 = \pm 5\%$

Sample hardness was measured for confirmation that the published material properties could be applied to the samples, and, in the case of the 300M samples, to confirm the results of the heat treatment process. The method for hardness testing was to take the average of five indent measurements at the end of the sample on each side, using a Rockwell hardness

tester; Newage Indentron NI 400. The results are shown in Table 3.4. It is unclear whether the AISI 4340 samples were annealed or normalized steel, since the measured hardness was in between. Annealed AISI 4340 was assumed, since it has a lower yield strength, which was used for the elastic bending experiment.

Table 3.4: Sample hardness measurements.

Material	Hardness (published)	Hardness (measured)
300M	50 Rockwell C [57]	53.6 Rockwell C
AISI 4340	Annealed: 17 Rockwell C Normalized: 40 Rockwell C [57]	29.3 Rockwell C
HY80	21 Rockwell C [45]	20.3 Rockwell C

The samples' conductivities, σ_c, were measured by way of Ohm's law, Equation 2.1.8, using 4-point contacts on the sample, as shown in Appendix C. This value, along with relative permeability μ_r, which was derived from the hysteresis experiment data in Section 3.1.5, was used to estimate the skin depth effect at different excitation frequencies, f, with the skin depth Equation 2.1.7. This equation gives the depth at which electromagnetic waves would dissipate by about a third into an infinitely thick sample material, and it provides an estimate for the depth the applied magnetic H field would magnetize the samples. Equation 2.1.7 can also be used to estimate the depth at which MBN signals can be detected, which have a frequency range of 1 kHz to 300 kHz with the majority of the signal at 200 kHz [10]. Table 3.5 shows the skin depth estimates for frequencies used in the following experiments; 2 Hz for the hysteresis plots, 30 Hz for the elastic bending, and 50 Hz for the plastic bending experiments, as well as the MBN frequency range.

3.2.1 Sample's microstructure

AISI 4340 has a microstructure of 100% martensite, 300M 100% tempered martensite and HY80 has 20% bainite and 80% martensite, as shown in Table 3.6. A Scanning Electron Microscope (SEM) was used to capture images of the samples' microstructure surface conditions. The striated surfaces of the HY80 and AISI 4340 samples, show grooves oriented longitudinally, as shown in Figures 3.9 a), c), d) and f). The 300M sample has hints of the

Table 3.5: Sample measured permeability and conductivity properties that were used to estimate the skin depth effect for selected frequencies.

Property & skin depth	300M	AISI 4340	HY80
Max Permeability, μ_r	243	593	1067
Conductivity, σ_c (S/m)	1.96×10^6	2.25×10^6	3.67×10^6
Skin depth at 2 Hz (mm)	16.3	9.8	7.3
Skin depth at 30 Hz (mm)	4.2	2.5	1.9
Skin depth at 50 Hz (mm)	3.3	2.0	1.5
MBN depth at 1 kHz (mm)	2.3	1.4	1.0
MBN depth at 200 kHz (majority noise) (mm)	0.16	0.10	0.07
MBN depth at 300 kHz (mm)	0.13	0.08	0.06

same grooves, but the surface is rough and granular as shown in Figures 3.9 b) and e), which may be evidence of the randomly orientated ferrite and cementite colonies that were locked in position by heat treatment.

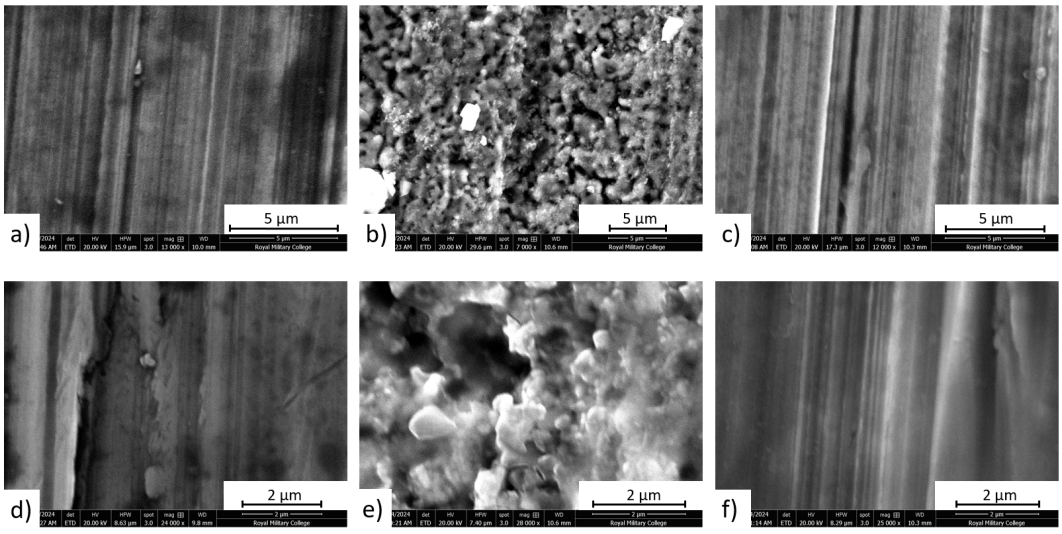

Figure 3.9: SEM images of high strength steel samples: a) AISI 4340 (5 μm scale), b) 300M (5 μm scale), c) HY80 (5 μm scale), d) AISI 4340 (2 μm scale), e) 300M (2 μm scale), and f) HY80 (2 μm scale).

The heat treatment process for 300M was in accordance to SAE international heat treatment of steel process AMS-H-6875 [60]. It was austentized at 840°C for one hour, oil quenched to room temperature and then tempered at 302°C for four hours and allowed to air cool. This process increases fracture toughness, since it allows carbon to precipitate

Table 3.6: Microstructure of steel samples.

Material	Carbon content (% wt)	Microstructure	Source
AISI 4340	0.4%	100% martensite	[59]
300M	0.4%	100% tempered martensite	[59]
HY80	0.15%	20% bainite, 80% martensite	[45]

at the grain boundaries, which strengthens the grains and allows some movement at the grain boundaries without fracture [61]. In preparation for the heat treatment process, the samples were painted with a ceramic coating called ATP-641 anti-scaling to prevent oxidation, which would have affected the surface conditions. The hardness test, as shown in Table 3.4, was performed to confirm that the heat treatment was conducted correctly and that it matched the expected values between 52-55 Rockwell C in accordance with the reference [62].

3.2.2 Samples' anisotropy

An assessment of the samples' anisotropy, or direction of 'easy' magnetic axis was conducted by measuring the Magnetic Barkhausen noise (MBN) response of the samples in different orientations. This was done by comparing the response for the sample oriented longitudinally, as shown in Figure 3.10 a), with it oriented transversely, as shown in Figure 3.10 b), with respect to the MBN probe. This test provided insight into the samples' magnetic anisotropy and surface conditions; whether there was residual stress from cutting or grinding produced in the samples, and if the heat treatment process had relieved these stresses.

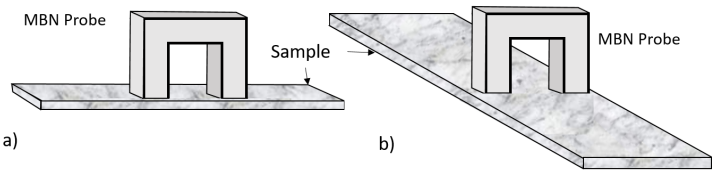

Figure 3.10: A sample orientated a) longitudinally, and b) laterally with respect to the MBN probe.

The MBN energy flux sweep measurements were conducted at 30 Hz excitation and the

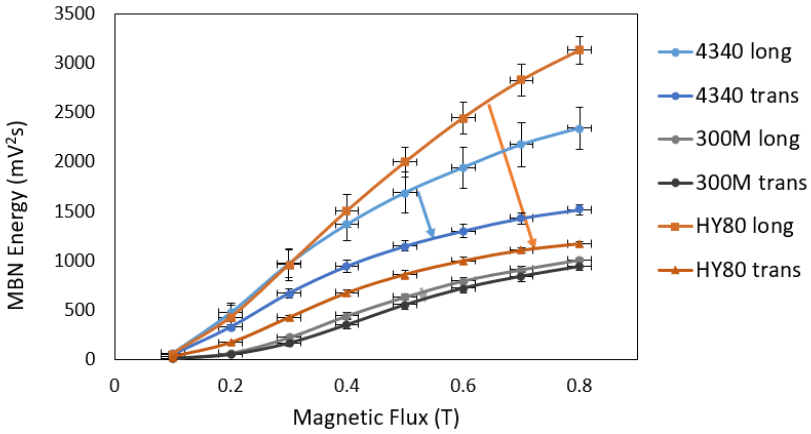

Figure 3.11: Samples' MBN response to being measured in a longitudinal and transverse orientation with respect to the MBN probe.

results are shown in Figure 3.11. Both AISI 4340 and HY80 samples show a difference in MBN response with sample orientation, as shown by a drop in MBN energy from the longitudinal to the transverse orientation, more so in HY80 than AISI 4340. This indicates magnetic anisotropy and the potential presence of stress on the surface in the longitudinal direction. The 300M sample shows very little change in MBN energy response with orientation, demonstrating that the sample's heat treatment successfully relieved the surface stresses, and isotropy for this material can be assumed.

Anisotropy affects the material's capacity to create or remove 180° domain walls (DWs) and is an indicator of internal stresses [63]. The configuration of DWs form to minimize total energy and, since there is an energy cost to adding walls, they tend to be aligned along the easy magnetic axis as indicated by the anisotropy [63]. Iron has positive magnetostriction [17] so tensile stress will increase anisotropy, as appears to be the case for the AISI 4340 and HY80 samples. This test provided insight into the samples' initial condition as a baseline for the following experiments.

4 Hysteresis plot experiment

Hysteresis plots are generated from measuring the magnetic B flux through a material due to an applied H field, according to the relationship in Equation 2.1.13. For this reason, it is also referred to as B and H field (BH) curves. This experiment was conducted on the high strength steel samples; AISI 4340, 300M and HY80, in order to measure their magnetic characteristics for saturation, permeability, coercivity and remanence, experimentally, and with the Włodarski model [7, 8] .

The objective of this experiment is to determine if the Włodarski model [7, 8] provides a good approximation for the hysteresis curves of 300M, AISI 4340 and HY80 steel samples. An accurate analytical model facilitates tracking and quantizing changes in magnetic characteristics under specific conditions. Włodarski model [7, 8] can be used to derive magnetic saturation, permeability, coercivity and remanence, as well as theoretical values for reversible and irreversible magnetization components.

4.1 Background: the Włodarski Model

This research selected the Włodarski Model [7, 8] for analyzing magnetic hysteresis loops, out of the available models mentioned in Section 2.2.1 and discussed in more detail in Appendix A. It claims to be simpler and less computationally intensive than other models, while maintaining similar accuracy for strongly hysteretic materials like 300M. The model incorporates concepts from the Rayleigh relation [20] to plot hysteresis loops at low H field strengths [8] and utilizes the FORC method [64] to derive asymmetric hysteresis loops [7].

4.1.1 Initial magnetization curve and parameter selection

A key advantage of the Włodarski model [7, 8] over the Preisach [21] and the Jiles-Atherton [22] models, is that it requires only five parameters to accurately plot hysteresis loops, all of which can be directly determined from the measured initial magnetization curve:

$$M(H) = M_a F\left(\frac{H}{a}\right) + \frac{M_b}{4}\left[F\left(\frac{H+c}{b}\right) + F\left(\frac{H-c}{b}\right)\right]^2, \tag{4.1.1}$$

where $M(H)$ is the magnetization of the sample as a function of H field, $F()$ is an odd function, and the five Włodarski parameters are:

- M_a is the reversible magnetization parameter;
- M_b is the irreversible magnetization parameter;
- a is the parameter governing the reversal rate from saturation;
- c is the coercivity parameter; and
- b is the parameter controlling the rate of approach to saturation.

The odd function most commonly used in this model to describe the S-shape curve of the hysteresis loop for ferromagnetic materials is the Langevin function [8];

$$F(x) = \coth(x) - \frac{1}{x}, \tag{4.1.2}$$

where $x = x(H)$ is a function of the applied field H, as given by the Włodarski model equations [7, 8].

Measuring the initial curve is difficult, so an experimental approximation method was used where the positive tips of nested hysteresis loops are plotted to create the curve [15]. Figure 4.1 shows how this method creates the initial magnetization curve from multiple hysteresis loops produced by an incrementally increasing alternating H field. An alternate method is to use an incrementally increasing DC field, but this was not used for this thesis due to equipment availability.

The data for the experimental approximation for the initial magnetization curve was measured as flux density $B(H)$, so Equation 4.1.1 is combined with Equation 2.1.13;

$$B(H) = \mu_0\left[M_a F\left(\frac{H}{a}\right) + \frac{M_b}{4}\left[F\left(\frac{H+c}{b}\right) + F\left(\frac{H-c}{b}\right)\right]^2 + H\right]. \tag{4.1.3}$$

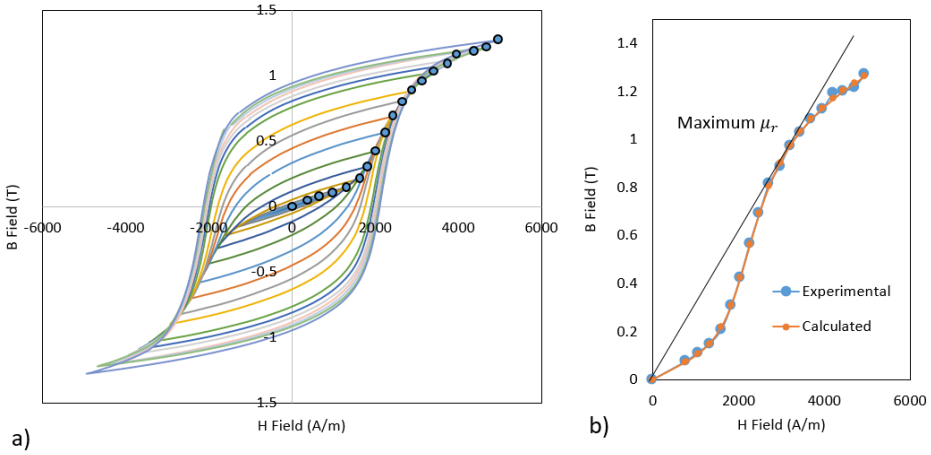

Figure 4.1: Experimental approximation of initial magnetization curve a) the positive tips of nested hysteresis loops identified, and b) plotted tips (blue) compared to calculation for initial magnetization.

An initial guess of the parameters is made so that there are there are two initial magnetization curves; one from experimental data and the other calculated from Equation 4.1.3. Then the difference between these two curves is calculated with the sum-squared-error (SSE) in Excel. An Excel Solver is used to minimize the SSE value by optimizing the five model parameters.

$$SSE = \sum_{i=1}^{n} [B(H_{mi}) - B_{mi}]^2 = \text{minimum} \ , \tag{4.1.4}$$

where B_{mi} is the experimental data for the maximum B flux value for the i^{th} loop and $B(H_{mi})$ is the equation derived for the B flux value at the maximum H field level of that same loop. This SSE method was also used to quantify how well the model approximates experimental data for the selected hysteresis loops.

The material's normal relative permeability, μ_r, is also estimated from the initial magnetization curve. This was done simply with Equation 2.2.1 for the points in the curve, then the largest value was selected as the relative permeability for the material, as shown in Figure 4.1 b).

4.1.2 Hysteresis loop modelling

Once the five model parameters; M_a, M_b, a, b, and c are derived from the initial magnetization curve, they can be used to model a hysteresis loop. For a loop with an H field range of $\pm H_m$, the magnetization curve for the lower, M_1 and upper, M_2, loop branches are given as;

$$M_1(H, H_m) = M_a F\left(\frac{H}{a}\right) + M_1(H, H_m, c) \ , \tag{4.1.5}$$

and

$$M_2(H, H_m) = M_a F\left(\frac{H}{a}\right) + M_2(H, H_m, c) \ . \tag{4.1.6}$$

The first term of the branch equations is the anhysteretic or reversible magnetization component; $M_{an}(H) = M_a F(H/a)$. The second term is the irreversible magnetization component that is superimposed with the anhysteretic component to model the loop. The terms $M_1(H, H_m, c)$ and $M_2(H, H_m, c)$ cycling between $\pm H_m$ are;

$$\begin{aligned} M_{12}(H, H_m, c) = \pm M(H_m, c) \mp \frac{M_b}{2} \times \left[F\left(\frac{H+c}{b}\right) - F\left(\frac{\pm H_m + c}{b}\right)\right] \\ \times \left[F\left(\frac{H-c}{b}\right) - F\left(\frac{\pm H_m - c}{b}\right)\right] , \end{aligned} \tag{4.1.7}$$

where $M(H_m, c)$ is a constant related to the tips of the loop where $H = \pm H_m$ is given as:

$$M(H_m, c) = \frac{M_b}{4}\left[F\left(\frac{H+c}{b}\right) + F\left(\frac{H-c}{b}\right)\right]^2 . \tag{4.1.8}$$

For better comparison between the experimental and modelled data, the magnetization branches, $M_1(H, H_m)$ and $M_2(H, H_m)$ were converted into B field values for the lower and upper branches, by way of Equation 2.1.13:

$$B_1(H, H_m) = \mu_0[M_1(H, H_m) + H] \ , \quad \text{and} \tag{4.1.9}$$

$$B_2(H, H_m) = \mu_0[M_2(H, H_m) + H] \ . \tag{4.1.10}$$

These equations can be plotted as nested magnetization hysteresis loops of any H field amplitude and are related to the BH curve through Equation 2.1.13.

4.1.3 Characteristics from hysteresis

Coercivity and remanence values depend on H_m and can be solved by setting Equation 4.1.5 or 4.1.6 to $M = 0$ and $H = 0$, respectively. The magnetic saturation for the material, M_s, is approximated with the reversible and irreversible magnetization parameters;

$$M_s = M_a + M_b \ . \tag{4.1.11}$$

Relative permeability is the ratio of the B field and the H field, with respect to the permeability of free space, so this value can be taken for any point around a hysteresis loop. For a standardized method between the different materials, the relative permeability value, μ_r, is estimated from the initial magnetization curve, as shown in Section 4.1.1.

The following section discusses how well this model was able to approximate measured major hysteresis loops for 300M, AISI 4340 and HY80 samples, as well as minor hysteresis loops for 300M.

4.2 Method

This experiment is conducted with three steel samples;

- 300M Sample, labelled S1;
- AISI 4340 Sample, labelled S2; and
- HY80 Sample, labelled S3.

The samples were cut to be the same width as the Supermendur U-core with dimensions and characteristics covered in Section 3.2.

BH curves were plotted with a 2 Hz alternating H field at incremental amplitudes creating a family of nested hysteresis loops. The maximum H field strengths of the loops were a result of the MBN system input voltage, which ranged from 1.5 V to 10 V at 0.5 V increments (seventeen loops total). The BH curve experimental set up was used as described in Section 3.1.5.

The Włodarski Model [7, 8] parameters were determined from the initial magnetization curves approximated by the positive tips of the nested loops, as shown in Section 4.1.1. The

experimental and modelled hysteresis data can then be compared with respect to magnetic characteristics; coercivity, remanence, saturation and permeability, which were derived in Section 4.1.3.

The analysis, by method of comparison between the model and the experimental loops, was conducted for two cases;

- six minor hysteresis loops for the 300M sample; and
- the largest or major hysteresis loops of each of the three sample materials.

The comparison between model and experimental data, for both cases, was assessed by how well the magnetic characteristics matched. For the second case, the model parameters were adjusted for a better fit, by way of SSE to see if the Włodarski model could be improved upon.

4.2.1 Assumptions

This experiment assumes that the magnetic B flux density is constant through the sample cross-sectional area. Based on the skin depth effect, Equation 2.1.7, the sample thickness is significantly less than the depth at which a flux gradient would become apparent for 2 Hz excitation and the relative permeability measured for the materials. Calculated results are shown in Table 3.5. The condition of constant B field also depends on the assumption that the mechanical and material properties of the samples are consistent throughout.

4.2.2 Sources of error

The BH curve program calculations are based on signals from the Hall sensors and the encircle coil. The Hall sensors measure H field as a function of lift off distance from the sample; 1.5 mm, 4.5 mm and 7.5 mm, linearly extrapolated to the surface. The spacing between the sensors is fixed but uncertainty would be introduced if their housing isn't placed right against the sample's surface. This spacing uncertainty is estimated at 0 to +0.1 mm or up to +7% variation in H field strength.

The encircle coil measures flux through the sample, which is used to determine the B field strength. Its uncertainty comes from the sample cross-sectional area measurement. The calipers measure to the hundredth of a mm but repetitive measurements of the same dimension can vary as much as 0.1 mm. As shown in Table 3.3, this results in a ± 5 to 6% uncertainty.

4.3 BH Curve experiment results

Seventeen loops, with input voltages from 1.5 V - 10 V, were measured for each steel sample; 300M, AISI 4340 and HY80, under no residual stress conditions, as shown in Figures 4.2, 4.3 and 4.4. These Figures show the experimental data only.

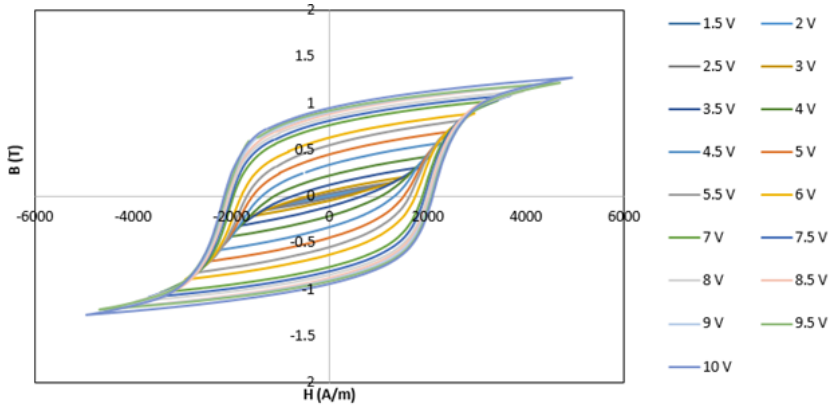

Figure 4.2: Experimental BH curves for 300M.

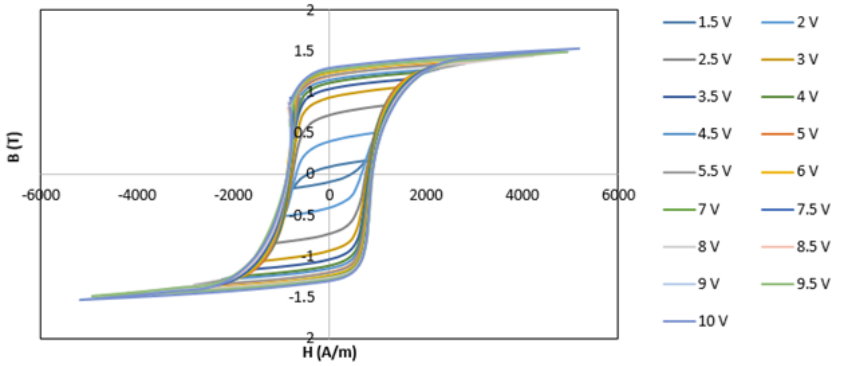

Figure 4.3: Experimental BH curves for AISI 4340.

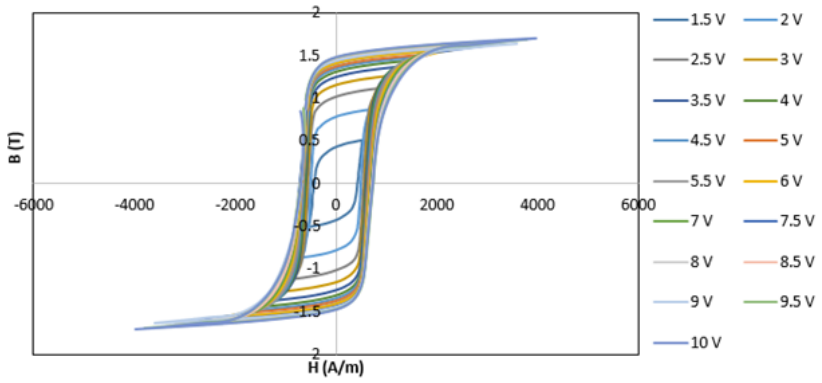

Figure 4.4: Experimental BH curves for HY80.

The initial magnetization curves for each sample are shown in Figure 4.5 with the experimental data in blue and the modelled curves derived with Equation 4.1.3 in orange, yellow and green for each sample. The initial curves show a good fit between experimental and calculated data but the AISI 4340 and HY80 samples are lacking data points around the low H field Rayleigh region, which would improve the results of the model parameters. All three curves do not plateau completely at the upper H field range, which indicates that magnetic saturation was not reached. These curves were used for the derivation of the Włodarski Model parameters and relative permeability, as summarized in Table 4.1.

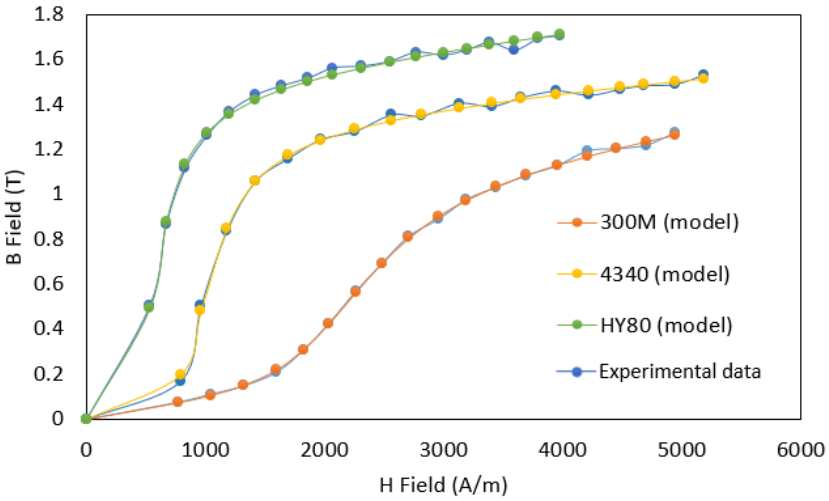

Figure 4.5: Initial magnetization curve approximation for each sample with experimental data in blue and modelled data in orange, yellow and green.

Table 4.1: Włodarski Model parameters and relative permeability from initial magnetization curves for 300M, AISI 4340 and HY80 samples.

Parameter	**300M**	**AISI 4340**	**HY80**
M_a (A/m)	1.10×10^6	6.45×10^5	6.31×10^5
a	5.32×10^3	6.62×10^3	8.84×10^3
M_b (A/m)	8.00×10^5	1.09×10^6	1.32×10^6
b	3.31×10^2	1.27×10^2	1.08×10^2
c	1.96×10^3	8.83×10^3	4.66×10^3
μ_r	243	593	1067

These model parameters will be used in the analysis to generate BH curves for the samples for comparison of fit and magnetic characteristics. The maximum relative permeability values were based on the initial magnetization curve, so there is little to no change between the experimental and model results. It is difficult to compare these permeability values with literature since it is influenced by composition and microstructure. Thomspon and Tanner [65] show that carbon content influences permeability with 0.17 weight % carbon steel (similar to HY80 with 0.15 weight %) having $\mu_r = 1266 \pm 20$ and 0.44 weight % carbon steel (similar to AISI 4340 and 300M with 0.4 weight %) having $\mu_r = 535 \pm 20$. Kahrobaee *et al.* [46] show that the heat treatment process affects the permeability of AISI D2 tool steel, which was similarly shown for AISI 4135 by Chai *et al.*[49]. Both materials are similar to AISI 4340 and 300M. Increasing the austenitizing temperature tends to decrease magnetic saturation, which decreases permeability, as is the trend between the AISI 4340 and 300M samples.

4.4 Analysis

The analysis of the results is a comparison between the experimental data and the model with respect to the magnetic characteristics that can be determined from magnetic hysteresis; coercicity, remanence, saturation and permeability. This section is broken into two parts; modelling minor hysteresis loops with the 300M sample and modelling major hysteresis for the three samples.

4.4.1 Modelling minor hysteresis loops

One of the benefits of the Włodarski model is its ability to model several minor hysteresis loops with the same parameters derived from the initial curve for the material. The applicability of this function was assessed with five minor loops, and the Major loop from the 300M sample experimental data. There loops are labelled Loops 1 - 5 and Major, and are identified by their loop tips; the peak B field, B_m, and H field, H_m point.

The same model parameters derived from the initial magnetization curve, as shown in Table 4.1 were used to model the minor loops as shown in Figures 4.6, and 4.7. The accuracy of these models was assessed by the peak magnetization, B_m, the loop axis intercepts for coercivity, H_c and remanence, B_r, and the difference between the curves by way of SSE. These characteristic comparisons with the experimental data are listed in Tables 4.2, 4.3, and 4.4, for loops 1-2, 3-4, 5 and major, respectively.

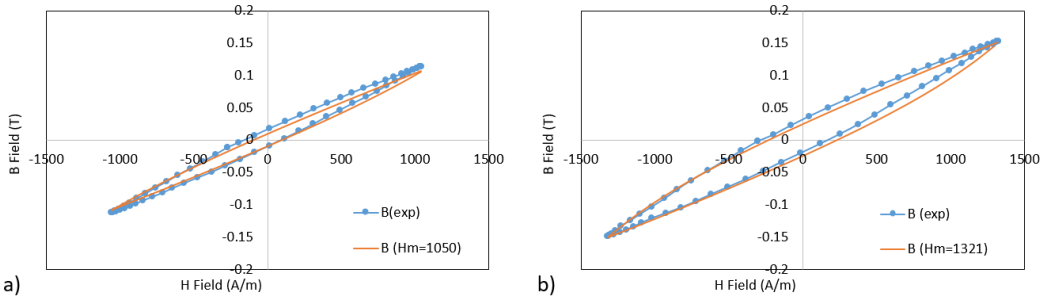

Figure 4.6: Experimental data and Włodarski Models of Rayleigh region hysteresis a) Loop 1 and b) Loop 2

Table 4.2: Minor Rayleigh loops 1-2 for 300M; loop peaks and plot intercepts for experimental data.

Characteristic	**Loop 1** ($H_m = 1050$ **A/m**)			**Loop 2** ($H_m = 1320$ **A/m**)		
	Exp.	**Model**	**Difference**	**Exp.**	**Model**	**Difference**
B_m (T)	0.113	0.107	5%	0.151	0.150	1%
B_r (T)	0.013	0.0095	27%	0.025	0.024	4%
H_c (A/m)	125	104	17%	219	229	5%
SSE	N/A	0.001	N/A	N/A	0.001	N/A

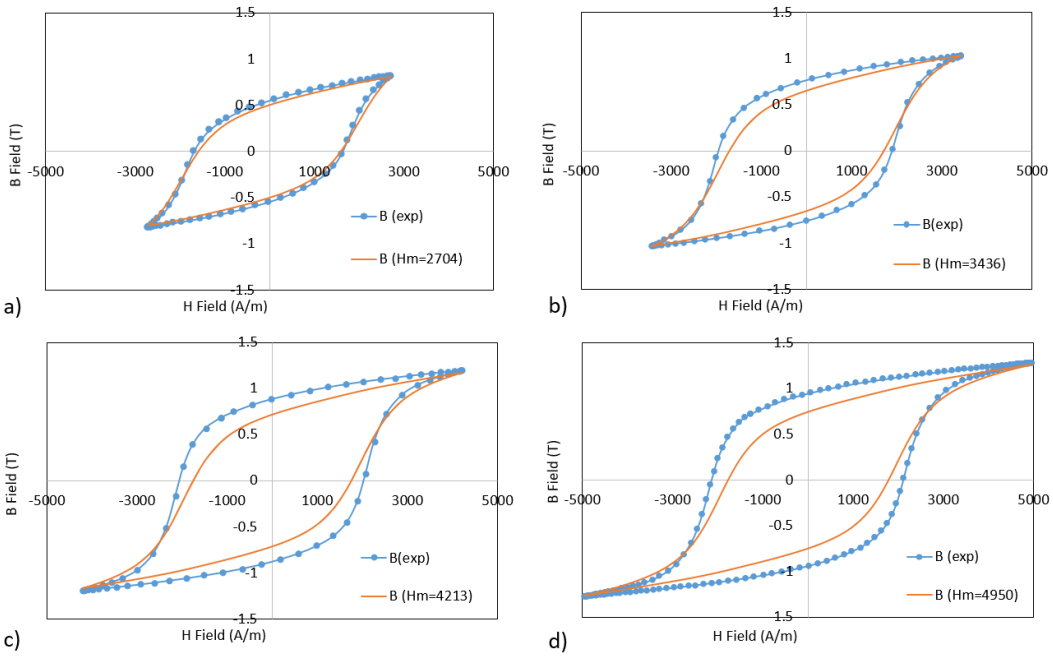

Figure 4.7: Experimental data and Włodarski Models of 300M hysteresis a) Loop 3, b) Loop 4 c) Loop 5 and d) Major loop.

Table 4.3: Minor loops 3-4 for 300M; loop peaks and plot intercepts for experimental data.

Characteristic	**Loop 3** ($H_m = 2704$ **A/m)**			**Loop 4** ($H_m = 3436$ **A/m)**		
	Exp.	**Model**	**Difference**	**Exp.**	**Model**	**Difference**
B_{max} (T)	0.817	0.805	1%	1.03	1.03	0%
B_r (T)	0.548	0.502	8%	0.762	0.652	14%
H_c (A/m)	1658	1587	4%	1922	1713	11%
SSE	N/A	0.062	N/A	N/A	0.27	N/A

Table 4.4: 300M minor loop 5 and major loop; loop peaks and plot intercepts for experimental data.

Characteristic	**Loop 5** ($H_m = 4213$ **A/m)**			**Major** ($H_m = 4950$ **A/m)**		
	Exp.	**Model**	**Difference**	**Exp.**	**Model**	**Difference**
B_{max} (T)	1.19	1.17	2%	1.27	1.26	1%
B_r (T)	0.882	0.716	19%	0.943	0.748	21%
H_c (A/m)	2047	1758	14%	2130	1778	-40%
SSE	N/A	0.63	N/A	N/A	1.04	N/A

The Włodarski Model [7, 8] fits the experimental data well for Loops 1, 2, and 3 but underestimates the B field amplitude above 1 T for the larger Loops 4, 5 and Major. In other

words, the model fits hysteresis loops that have an H_m amplitude below 60% of the range of the initial magnetization curve. There is limited loop width information in the initial curve, so, as the hysteresis loops get wider, the model gets less accurate. If the experimental magnetization curve was able to be measured all the way to saturation, this additional data and increased H field range could allow the model to fit BH loops above 1 T. Even with the increased range, it is still unlikely that the model would be able to accurately approximate the major hysteresis loop for saturation because of the method of deriving the parameters.

One of the challenges of multi-parameter fitting is that all the model parameters are based on the single dimensional initial magnetization curve of Figure 4.5 to produce a two dimensional loop. There is interdependency between the five model parameters; both a, b and c influence the slope of the curve and M_a and M_b affect the B field amplitude, so different permutations can produce the same curve. Therefore, the repeatability of the parameter derivation will depend on the initial guess for the values before running the Excel solver.

4.4.2 Modelling major loops of all samples

Comparison of the model and experimental data was conducted with the largest hysteresis loop for each sample. The loops are identified by their positive tip values of H_m and B_m, where B_m provides an experimental estimate for the material's saturation, $B_s \approx B_m$. Coercivity, H_c, and remanence, B_r, values were taken as the x and y axis intercepts, respectively, of the major loops and maximum relative permeability, μ_r was determined by the tangent to the 'knee' of the loop.

Figures 4.8 a), b) and c), show the major hysteresis loops for 300M, AISI 4340 and HY80 samples, respectively, comparing the experimental data with the Włodarski modelled loops using initial and adjusted parameters. The adjusted parameters were derived by running the SSE Excel Solver to best fit the entire major hysteresis loop, rather than the initial magnetization curve.

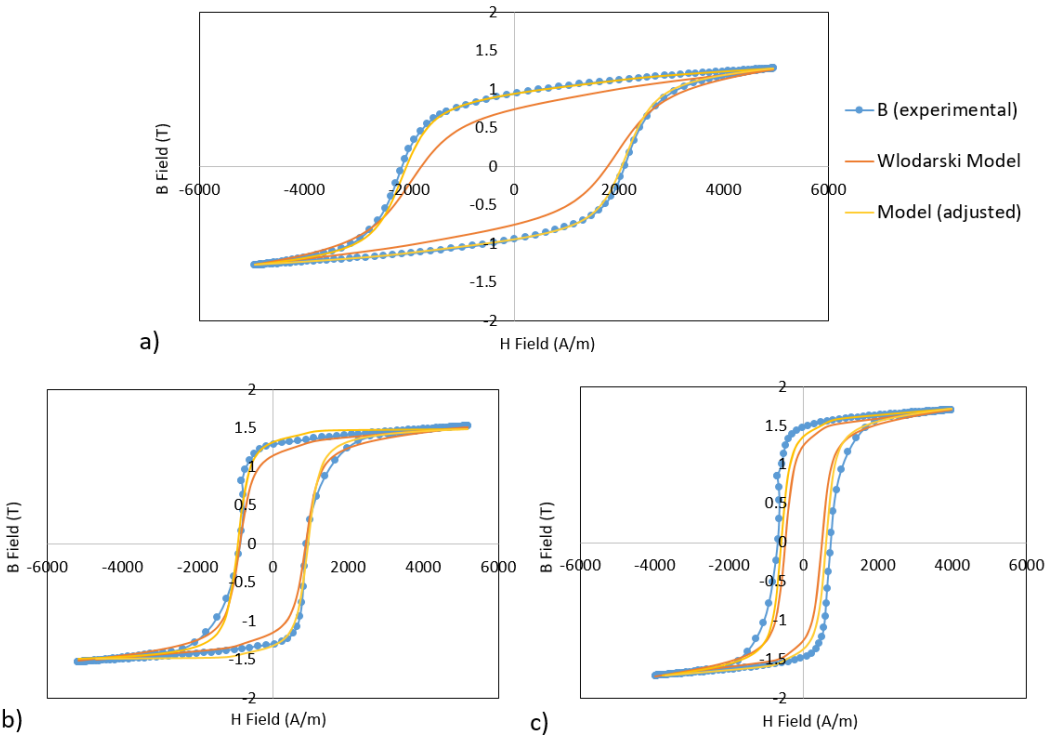

Figure 4.8: Major hysteresis loops with original and adjusted model parameters for a) 300M for $H_m = 4950$ A/m b) AISI 4340 for $H_m = 5180$ A/m, and c) HY80 for $H_m = 3970$ A/m.

This adjusting method is not part of the published procedure for the Włodarski Model [7, 8], but is explored in this analysis to improve on the parameter fit with the entire hysteresis curve instead of just the positive tips that make up the initial magnetization curve. The adjusted model parameter loop are shown with the initial parameter and experimental loops in Figures 4.8, for 300M, AISI 4340 and HY80 and summarized in Table 4.5.

This method of adjusting the model parameters worked best for the 300M sample, since the initial parameters already gave a good approximation of the experimental data. This adjusted model was within 5% of the experimental loop for the coercivity and remanence. The AISI 4340 model had more difficulty adjusting the parameters for better fit; the coercivity and remanence intercepts were within 1-11% of the experimental data for both the initial and adjusted parameters. When adjusting the AISI 4340 model, the magnetic saturation estimate was increased significantly from $B_s = 2.18$ T to $B_s = 3.57$ T between the initial

and adjusted models. This indicates that the adjustment mostly affected the M_a and M_b parameters, increasing both the reversible and irreversible magnetization parameters. The HY80 model was the most difficult to simulate; the coercivity and remanence values could be brought within 15% of experimental data. The resulting model parameters derived from this adjustment method are presented in Appendix D Table D.2.

Table 4.5: Experimental and modelled BH curves for 300M, AISI 4340 and HY80 major hysteresis loops.

Characteristic	**Exp. 300M**	**Model 300M (initial)**	**Diff.**	**Model (adjusted)**	**Diff.**
H_m (A/m)	4950	4950	N/A	4950	N/A
B_m and B_s (T)	1.27	2.39	88%	1.66	23%
B_r (T)	0.943	0.748	21%	0.941	0%
H_c (A/m)	2130	1778	17%	2036	5%
μ_r	256	262	2%	N/A	N/A
SSE	N/A	1.04	N/A	0.063	N/A
Characteristic	**Exp. 4340**	**Model 4340 (initial)**	**Diff.**	**Model (adjusted)**	**Diff.**
H_m (A/m)	5180	5180	N/A	5180	N/A
B_m and B_s (T)	1.53	2.18	42%	3.57	233%
B_r (T)	1.31	1.15	12%	1.32	1%
H_c (A/m)	872	880	1%	939	7%
μ_r	523	581	11%	N/A	N/A
SSE	N/A	1.09	N/A	0.45	N/A
Characteristic	**Exp. HY80**	**Model HY80 (initial)**	**Diff.**	**Model (adjusted)**	**Diff.**
H_m (A/m)	3970	3970	N/A	3970	N/A
B_m and B_s (T)	1.71	4.74	177%	2.70	58%
B_r (T)	1.48	1.25	16%	1.37	8%
H_c (A/m)	712	487	32%	608	17%
μ_r	768	1050	37%	N/A	N/A
SSE	N/A	37.6	N/A	1.9	N/A

4.5 Discussion

The purpose of the hysteresis plot experiment, Section 3.1.5, was to assess if the Włodarski model [7, 8] provided a good approximation to experimental measurements of hysteresis

loops for the three sample materials; 300M, AISI 4340 and HY80. Comparison with the largest experimental hysteresis loop showed the model underestimated the coercivity and remanence intercepts and overestimated the magnetic saturation, as shown in Figure 4.8 and Table 4.5. The model parameters could be adjusted to better fit the hysteresis loop by minimizing the sum-squared-error (SSE) difference between the model and the experimental data using an Excel Solver. This adjustment method worked better for the 300M sample than the AISI 4340 and HY80 because of the shorter and wider shaped loop of the magnetically harder 300M material.

Model applicability was also assessed for minor loops with the 300M sample. This comparison showed that the model provided a better approximation to smaller experimental loops, particularly in the Rayleigh region, with good accuracy up to an H field amplitude of $H_m = 2704$ A/m, which was approximately 60% the size of the largest experimental loop. The size of the experimental hysteresis loops was limited to 10 V input by the equipment, but if it could produce experimental data up to saturation, then the model could potentially increase its H field amplitude range accuracy.

For larger loops, the model struggled with the coercivity, or width of the loop, since the governing parameters were derived from the initial magnetization curve, which was a one dimensional representation of the two dimensional loops. This is evident in Figure 4.8, where the main challenge in fitting this model to the AISI 4340 and HY80 loops was approximating the 'knee' of the curve. The experimental loop produced a different curve radius depending on whether the material was approaching saturation (large radius) or reversing from it (smaller radius). Conversely, 300M has an equally large radius for the inner and outer curve of the 'knee' and does not have this discrepancy.

Understanding this limitation of the model and having the SSE method to adjust the parameters for larger loops, allows the Włodarski model [7, 8] to be a viable technique for modelling hysteresis loops of 300M steel samples, alternative to the more computationally expensive Priesach [21] or Jiles-Atherton [22] models.

5 Elastic Bending Experiment

This experiment examines how Magnetic Barkhausen noise responds to elastic bending stress in high strength steel samples; 300M, AISI 4340 and HY80.

The objective is to correlate MBN energy to elastic stress in order to propose a calibration technique for stress detection with this MBN system. This is done with a four-point bending apparatus, which applies stress by controlled bending of the sample, while an MBN probe on the top and bottom of the sample take measurements of compressive and tensile stressed surfaces, respectively.

5.1 Background

Applying stress to a ferromagnetic material changes the permeability of the material when it is within the elastic regime [18], due to magnetostriction and changes to the domain structure [32]. Beyond the elastic regime, plastic deformation takes place, which causes slip planes and dislocations within the material's crystalline lattice structure to take place. This changes the interaction between stress and magnetic properties, which is explored in Section 7; Plastic Bending Experiment.

5.2 Method

This experiment consisted of two parts: MBN measurements under elastic bending, and confirming bending stress by strain gauge measurements. The equipment and samples for both parts are described in Section 3. Below is a summary of the method followed for this

experiment.

5.2.1 Part 1: MBN response to elastic bending

The primary sample tested is 300M steel. AISI 4340 and HY80 samples are also examined for comparison. Two samples of each material are tested, originally labelled S3 and S5 for the 300M, S1 and S2 for AISI 4340 and S1 and S3 for HY80, as shown in Table 5.1. For simplicity, the samples are referred to by their material.

Elastic stress is applied to the samples by way of bending in the MBN bending apparatus, according to the stress calculations for bending deflection covered in Appendix B. For each bending increment, the MBN response in the form of MBN energy is measured across a flux sweep from 0.1 to 0.8 T under flux control at 30 Hz excitation frequency. The tested ranges for each sample are summarized in Table 5.1.

Table 5.1: Summary of sample stress ranges calculated and measured.

Sample	**Yield strength (MPa)**	**Deflection range (mm)**	**# of increments**	**Stress range (MPa)**
300M; S3, S5	1500	0-3.35	20	0-1180
AISI 4340; S1, S2	470	0-1.43 mm	9	0-502
HY80; S1, S3	570	0-0.61 mm	11	0-281

The elastic bending test was performed on both sides of the sample (flipping the sample between bending) and with two samples of each material, for a total of four sample sets. The average of these four sets of measurements was plotted with the standard deviation between them added to the uncertainty calculation. The bending calculations were confirmed with strain gauge measurements, which experimentally showed the tensile stress applied to each sample. Due to an initial bending calculation error, the AISI 4340 samples were inadvertently bent beyond yield during this experiment.

5.2.2 Part 2: Strain measurements

One sample of each material was equipped with a strain gauge: 300M S6, AISI 4340 S5 and HY80 S4. These samples were bent in the MBN bending apparatus with the bottom probe

removed, so that the gauge could measure strain due to tensile bending. The equipment and procedure followed are discussed in Section 3.1.3. Each strain gauged sample was bent twice, with three strain measurements per bending increment. The average of the two sets of data was used with Hooke's law (Equation 3.1.1) to determine the bending stress, and the standard deviation between the data sets contributed to the uncertainty calculations.

5.2.3 Assumptions

There are three main assumptions for this elastic bending experiment;

1. the samples are linear elastic materials;
2. the samples have uniform properties throughout their thickness and along the top and bottom surfaces; and
3. the top and bottom MBN probes are similar.

The first assumption allows for the use of the bending calculations, in particular Hooke's law, Equation 3.1.1, which assumes a constant Young's modulus, E for the slope of the elastic regime on a stress-strain plot. This is supported by the published mechanical properties for the materials [57][58][36].

The second assumption is that the samples are uniform through the thickness of the material and that the top and bottom surfaces are identical. The samples were cut from the same stock but minor differences in MBN response were noticed with position changes along the top and bottom surfaces. For this reason, repeatability tests were conducted to capture this variation and each sample was measured twice in bending, with the sample flipped in between.

Finally, the top and bottom probes are assumed to be identical in construction and function. Repeatability tests show that the bottom probe draws slightly more current for the higher flux levels than the top probes does, which results in a different shaped flux sweep curve. Calibration between the probes is conducted for the zero stress state of the samples but could not be assumed to have the same calibration factor under bending. For this reason, the results from the probes are kept separate and MBN energy response for tension (bottom side, bottom probe) and compression (top side, top probe) are assessed independently.

5.2.4 Sources of error

There are three main sources of uncertainty in this experiment, which affect the bending force applied and the MBN responses measured. The bending force is affected by the uncertainties with measuring bending deflection and the MBN responses are affected by the variation in the sample surface and the MBN system itself. Two tests were conducted to establish uncertainty values for both sources of error; the zeroing test and MBN repeatability test. The data collected for these tests are in Appendix E and the results are below.

5.2.4.1 Zeroing test

The accuracy of the measured bending force on the sample is reliant on the deflection gauge and its set up. The gauge reads in increments of 0.01 mm, so the precision of each deflection measurement is ± 0.01 mm. The initial set up for the 0 mm deflection has more uncertainty, since it is difficult to obtain contact between the top pins and the sample, while applying no load. A trial was conducted to collect the variation in the initial set-up deflection with two different samples. These samples were removed and returned in the bending apparatus 10 times each in the four possible orientations; flipped side up and down, and swapped left and right end. The deflection for each set-up was recorded without adjusting the dial. The results of this trial are summarized in Table 5.2, where the largest variation measured was converted to equivalent stress and used as the uncertainty. This resulted in an initial stress variation of ± 15 MPa for 300M and AISI 4340 and a variation of ± 25 MPa for HY80.

Table 5.2: Deflection and equivalent stress variation for initial sample set-up in the bending apparatus.

Sample material	Largest variation	Equivalent stress variation	Rounded stress variation
300M	± 0.041 mm	14 MPa	± 15 MPa
AISI 4340	± 0.045 mm	16 MPa	± 15 MPa
HY80	± 0.051 mm	24 MPa	± 25 MPa

5.2.4.2 Repeatability test

The accuracy of the MBN probes was assessed by repeatability tests, which accounts for the variations of sample surface conditions and the MBN system. This involved taking several measurements at different positions along the top and bottom surface of samples under zero load conditions. The variation in MBN energy is determined by the standard deviation of 20 total measurements taken with the top and bottom probes of two different samples of each material. These results give an average zero stress MBN energy measurement and uncertainty value for 0.8 T flux and 30 Hz for each sample material, as shown in Table 5.3.

Table 5.3: Average MBN energy variation at 0.8 T flux and 30 Hz excitation for 300M, AISI 4340, and HY80 samples.

Sample material	Ave. MBNe (mV^2s)	Variation (mV^2s)	Difference
300M	980	121	12 %
AISI 4340	2450	163	7 %
HY80	3005	114	4 %

5.3 Results

5.3.1 Part 1: MBN response to elastic stress

MBN energy response increases with tensile stress and decreases with compressive stress, as expected from previous research [42]. Flux sweep results from the high strength steel samples, 300M, AISI 4340 and HY80, a range of responses to bending stress, is shown in Figure 5.1. 300M shows the largest response to stress, Figure 5.1 a), partly because it has the highest yield strength of the samples tested; 1500 MPa compared to 470 MPa for AISI 4340 and 570 MPa for HY80. AISI 4340 showed an increase in MBN energy with tension but very little change with compression in Figure 5.1 b). HY80 showed the least MBN energy response to stress in Figure 5.1 c).

The shape of the flux sweeps change as the stress increase, for the 300M and AISI 4340 samples, the MBN energy stops increasing with flux between 0.5 T and 0.8 T. For 300M in Figure 5.1 a) there is a drop in MBN energy between 0.6 T and 0.8 T for 882 MPa tension.

Due to this change in flux sweep shape with stress, a single flux value was selected for analysis of MBN response to elastic bending.

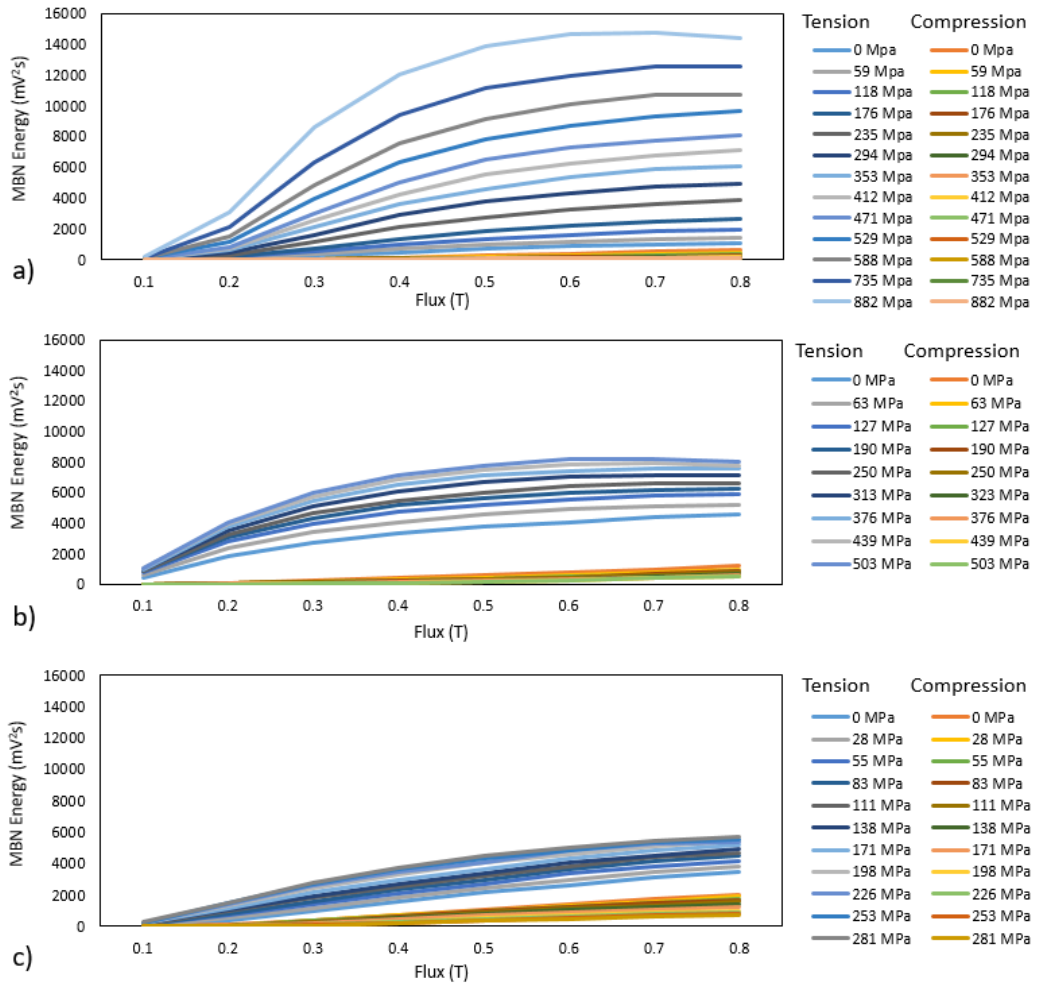

Figure 5.1: MBN energy flux sweeps for elastic bending of samples; a) 300M S3, b) AISI 4340 S1, c) HY80 S1.

0.8 T flux was selected for further analysis of MBN response to stress, as it is the highest flux value measured and has been used for MBN response analysis for previous research [45]. Figure 5.2 shows the relationship of MBN energy with tensile stress, and Figure 5.3 shows the samples' MBN response under compression. The MBN energy values plotted are the average of the four sets of measurements taken for the sample material. The error bars were calculated from the standard deviation of these measurement sets, plus the

standard deviation of the repeatability tests taken in Section 5.2.4.2. The stress error bars were calculated from the deflection dial uncertainty obtained from an initial zeroing set up for the samples, as shown in Section 5.2.4.

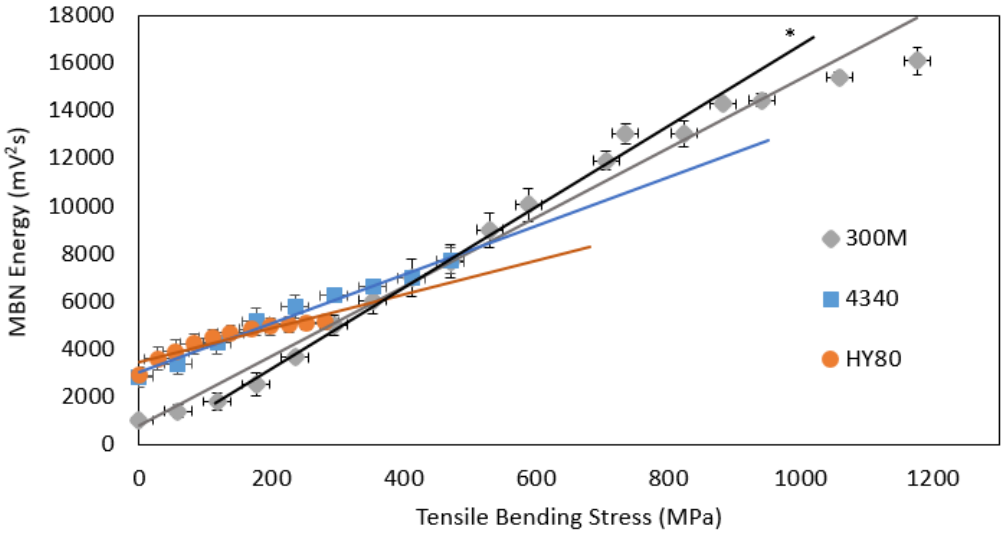

Figure 5.2: MBN energy at 0.8 T flux for samples under tensile bending. Solid trend lines are linear best-fits to the data and the black line* is the trend for 300M between 100-900 MPa.

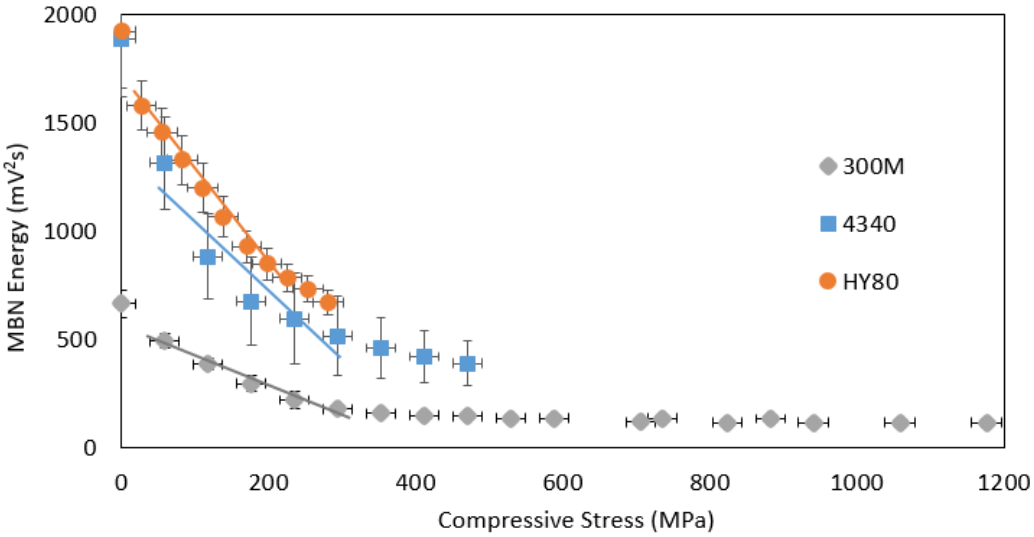

Figure 5.3: MBN energy at 0.8 T flux for samples under compression bending. Solid trend lines are linear best fits for select ranges of the data, as specified in Table 5.4

The rate MBN energy in response to tensile bending can be approximated with a linear trend line of the data shown in Figure 5.2. The 300M response between 100 MPa and 900 MPa is a very linear region in the elastic range, which is shown by the black trend line* in Figure 5.2. Beyond 900 MPa, 300M rate of change for MBN energy to stress decreases. A similar correlation was made for a selected range of the compressive stress response, since a trend line could not be fit well to the whole range of data. The slope and fit of the MBN energy response to both tensile and compressive stress for the three samples, at 0.8 T flux and 30 Hz, is summarized in Table 5.4.

Table 5.4: linear best fit trend of samples' rate of MBN energy change with tensile and compressive stress, over specified ranges.

Tensile stress			
Sample	**Range (MPa)**	**Slope (mV^2s/MPa)**	**Slope fit (R^2)**
300M	0-1180 $\pm$15	14.5	0.98
300M*	100-900 $\pm$15	16.7	0.99
AISI 4340	0-502 $\pm$15	10.2	0.98
HY80	0-281 $\pm$25	7.1	0.88
Compressive stress			
300M	55-300 $\pm$15	-1.4	0.98
AISI 4340	55-300 $\pm$15	-3.2	0.87
HY80	25-225 $\pm$25	-4.2	0.99

Figure 5.4 a) and b) gives a 2D Magnetic Object model (MO) model [18] of how the magnetic domains reconfigure when subjected to loading along the easy axis in tension and compression, respectively. In tension, the number of 180°domain walls increase to accommodate the additional energy into the system [63]. This will increase the rate of domain wall (DW) interaction with pinning sites resulting in more MBN energy when applying the magnetic field in the longitudinal direction [44, 66]. The MBN energy for the 300M sample starts lower and changes the most with tension, compared to the other two samples. This may be due to the sample's heat treatment process, which relieved stress induced surface anisotropy from grinding or rolling (see Section 3.2.2) and increases the material's capacity to increase 180°domain walls.

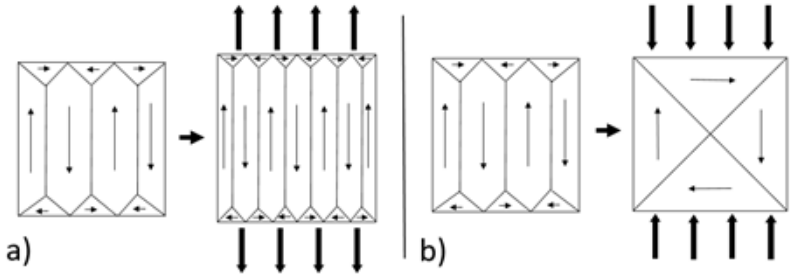

Figure 5.4: Magnetic Object (MO) model change of magnetic domains in response to stress: a) MO under tensile stress and b) MO under compressive stress.

Under compression, the opposite is happening, as shown in Figure 5.4 b). The $180°$ magnetic domain walls parallel to the direction of compressive force are decreasing until only $90°$walls remain, beyond which, no further reduction in domain wall area is possible [66]. This could explain why the MBN energy for the 300M sample levelled off after 300 MPa compression in Figure 5.3.

This behaviour of MBN energy change with stress, is consistent with magneto-elastic effects [18, 42]. Since iron has positive magnetostriction, tensile stress encourages the domains to align themselves along the stress axis, which coincides with the magnetization axis for the MBN measurements.

5.3.2 Part 2: Strain measurements

The elastic bending experiment was conducted with a strain gauged sample to confirm the bending stress calculated by deflection. The results are shown in Figure 5.5, where the green data is the stress values by strain measurements and the grey, blue and orange data the stress values by bending calculations for the 300M, AISI 4340 and HY80 samples, respectively. The uncertainty for the bending calculation comes from the precision of the deflection gauge as shown in Table 5.2. For the strain gauge measurements, this uncertainty is added to the standard deviation of two sets of strain measurements conducted for each sample.

The 300M and AISI 4340 samples show slightly higher stress by strain measurements than by bending calculation, but the general trend is linear for the deflection range. The

HY80 sample has a curve in the strain measured stress, which suggests that it is not as linearly elastic a material as the other two.

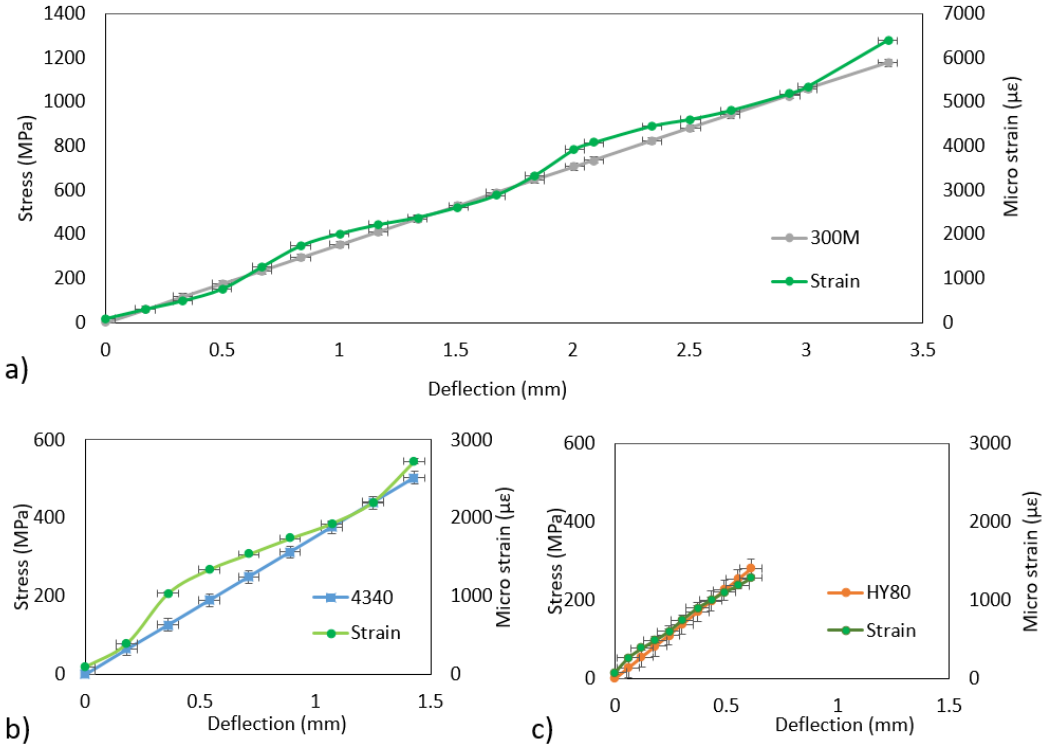

Figure 5.5: Stress, from elastic bending calculations and by strain measurements for samples a) 300M, b) AISI 4340 and c) HY80.

5.4 Discussion

The goal of the elastic bending experiment, Section 5, was to explore MBN response to elastic stress to assess if this comparison could be used as a method of calibration for determining stress in 300M, AISI 4340 and HY80 steels. The result was a near linear correlation between MBN energy and tensile stress for 300M and AISI 4340 at 0.8 T flux, for a specific range, as shown in Table 5.4. The tensile stress comparison for HY80 was more curved than a strict linear relationship, but it had the most linear trend for energy response to compressive stress, of the three samples. The 300M sample resulted in a better fit MBN energy

correlation with tensile stress, of the three samples, and demonstrated a linear relationship for a stress range of 100-900 MPa at 0.8 T flux.

6 Discussion on the first two experiment results

The results of the first two experiments provided an opportunity to explore the relation between the magnetic hysteresis model and MBN energy response.

6.1 Irreversible magnetization by Włodarski Model and MBN response

MBN occurs primarily due to the irreversible magnetization processes, B_{irr}, when the 180°domain walls (DWs) are moving in response to an applied H field. Reversible magnetization, B_{rev} primarily occurs in the Rayleigh region of low applied H field and during the approach to saturation, as previously shown with Figure 2.9. If the Włodarski model [7] [8] reflects this basic physics theory, it would be expected that a hysteresis loop with a higher irreversible magnetization component would correspond to higher MBN response.

The Włodaski parameters from Section 3.1.5 are compared with the initial MBN energy responses from the elastic bending experiment, Table 6.1 in Section 5. The results follow the predicted trend of higher irreversible magnetization component producing higher MBN energy, between the three sample materials; 300M, AISI 4340 and HY80. The lowest MBN energy response matches 300M as the material with the lowest irreversible magnetization component, whereas HY80 has the highest initial energy response and the largest comparative irreversible magnetization component. Figure 6.1 shows that this trend is still followed when comparing the ratio of irreversible magnetization to reversible magnetization compo-

nents, where the lowest ratio of 300M has the lowest energy response and the highest ratio is for the material with the highest initial energy value.

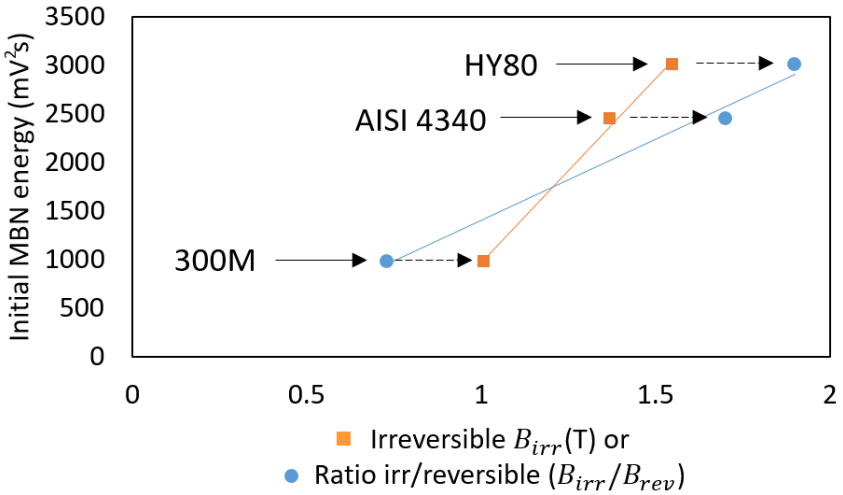

Figure 6.1: Comparison of initial MBN energy response and the irreversible magnetization component, B_{irr}, by the Włodarski model for 300M, AISI 4340 and HY80 samples.

Table 6.1: Average MBN energy response for the three sample materials compared with the irreversible magnetization component, B_{irr}, of the hysteresis model.

Magnetization property	**300M**	**AISI 4340**	**HY80**
MBN energy at 30 Hz (mV^2s)	980±120	2450±160	3005±114
Irreversible M_b (A/m)	8.00×10^5	1.09×10^6	1.23×10^6
Irreversible B_{irr} (T)	1.01	1.37	1.55
Reversible M_a (A/m)	1.10×10^6	6.45×10^5	6.31×10^5
Ratio B_{irr}/B_{rev}	0.73	1.70	1.90

6.2 MBN response to bending

This section discusses how MBN energy responds to bending stress for both the elastic bending experiment and the plastic bending experiment. It should be noted that these experiments were conducted at different excitation frequencies; 30 Hz for the elastic stress bending experiment Section 5 and 50 Hz for the plastic bending experiment Section 7. The effects of frequency on MBN response are discussed in Appendix F.

7 Plastic Bending Experiment

This experiment explores the MBN response to residual stress in 300M samples due to plastic bending. It is a combination of the previous two experiments, first, by measuring MBN response to bending stress, and second as BH curve measurements, with the difference of extending these measurements into the plastic regime.

The objective of this experiment is to assess if the MBN response to residual stress can be correlated to an equivalent level of elastic stress. This would allow the MBN system to be calibrated with elastic stress, for the detection of residual stress in 300M, with applications for aircraft landing gear.

7.1 Background

This section provides additional background to that which was provided for the previous two experiments, as relating to the calculations of plastic deformation used in the analysis of this experiment.

7.1.1 Plastic deformation calculations

Plastic bending stress and residual stress due to deformation is covered in Appendix B and summarized here. These calculations are based on the assumption that the material is elastic-perfectly plastic, meaning that the maximum stress it can experience in the plastic regime is the yield stress, $\sigma_{max} = \sigma_e$.

Under the apparatus' four-point bending configuration, the sample's strain, ϵ is directly

related to the bending deflection and radius of curvature R.

$$\frac{1}{R} = \frac{d^2 y_0}{dx^2} = \frac{M}{EI} = -\frac{\epsilon}{y} \,, \tag{7.1.1}$$

where y_0 is the deflection of the centroidal axis through the sample, noted as δ when referring to the deflection between the contact pins measured by the deflection gauge. x is the horizontal position along the length of the sample, M is the bending moment, E is the Young's modulus, I is the moment of inertia and y is the vertical position through the thickness of the sample where the deflection or radius of curvature is being measured, which is $y = c$ for the surface of the sample.

For elastic bending, strain is linearly related to stress through Hooke's law, Equation 3.1.1. Bending stress beyond the yield strength results in slip planes and dislocations [41] within crystalline lattice structure of the material, which creates a plastic zone causing deformation when the load is removed [67] [68]. Since strain continues to increase with deflection, the maximum loaded strain, ϵ_{max}, can be used to calculate the height of the plastic zone, h_p, which causes residual stress when unloaded.

$$h_p = c - \frac{\sigma_e c}{E(\epsilon_{max})} \,, \tag{7.1.2}$$

where σ_e is the yield strength, E is the Young's modulus and c is the half thickness of the sample. The plastic zone height can then be used to calculate the bending moment, M_z it took to create it;

$$M_z = \frac{I_z \sigma_e}{c}\left[1 + \frac{h_p}{c} - \frac{1}{2}\left(\frac{h_p}{c}\right)^2\right] . \tag{7.1.3}$$

Now the moment can be used to calculate the residual stress, σ_{res} because linear unloading for the bending force being removed is assumed;

$$\sigma_{res} = \frac{M_z}{I_z} c - \frac{\sigma_e c}{c - h_p} \,, \tag{7.1.4}$$

where I_z is the moment of inertia for the rectangular cross-sectional area of the beam and σ_e is the yield strength.

This series of calculations to obtain residual stress can be shown with a stress distribution diagram with superposition, as shown in Figure 7.1. The beam is loaded with a

moment, M_z, beyond the yield point, which creates a plastic zone, then it is added to a linear unloading step, which results in the permanent deformation with residual stress.

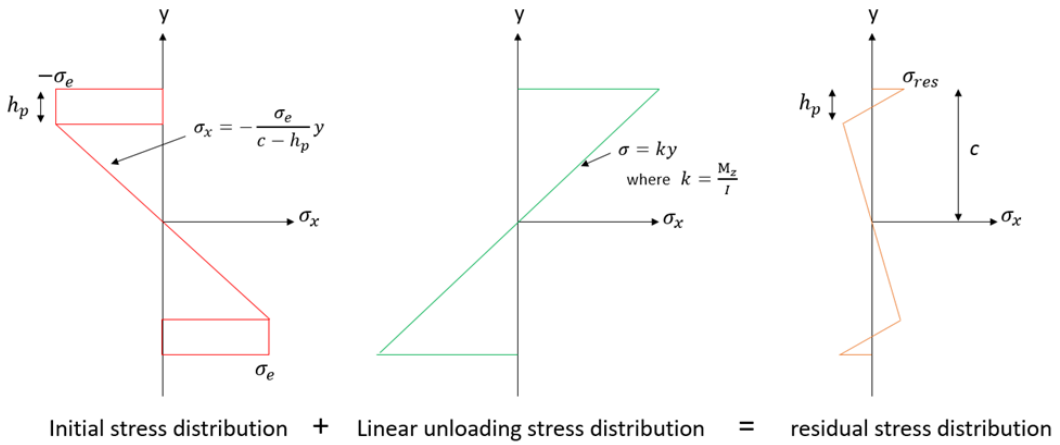

Figure 7.1: Residual stress distribution as a result of initial stress and linear unloading (adopted from [40]).

Strain gauge measurements are used to establish the stress on the surface of the sample in the loaded and unloaded (residual stress) states, according to these calculations. In the case that the strain gauge breaks before the sample does, the linear relationship between the deflection and strain, Equation I.0.2, and plastic height and strain, Equation 7.1.1, are used to extrapolate the expected strain and residual stress. These measured and calculated stress results are then compared to the Finite Element Method (FEM) analysis for the sample in bending.

7.1.2 FEM stress analysis

FEM stress analysis was conducted with ANSYS, Version 2024 R2 by Fan Liu, a fellow Masters student. The sample in bending was modelled with the four contact pins of the bending apparatus to better approximate the experimental stress conditions. This section covers the descriptions and limitations of this ANSYS model, while more details can be found in Appendix G.

The four-point contact pins were modelled as 2.5 mm radius cylinders of structural steel

with material properties from the ANSYS database [69]. A sweep mesh method was used with 1 mm element size for the sample and contact pins. The mechanical properties for both components of the model are listed in Table 7.1.

Table 7.1: Dimensions and mechanical properties of the sample and contact pins input for the ANSYS model.

Characteristic	300M Sample	Structural steel contact pins
Dimensions	$100\times19\times2.0$ mm^3	2.5 mm radius, 19 mm length
Yield strength	1500 MPa	250 MPa
Ultimate strength	2000 MPa	460 MPa
Poisson's ratio	0.28	0.3
Elastic modulus	205 GPa	200 GPa
Tangent modulus	13.6 GPa	N/A

The sample properties were taken from the stress-strain curve data from a previous 300M sample, conducted by M. Kashefi in 2023 [70], in accordance with the ASTM standard for tensile testing. This stress-strain curve was approximated as isotropic bilinear with straight lines for the elastic and plastic regions, as shown in Figure 7.2. The slope of the plastic regime, the tangent modulus, was calculated on the curve half way between the yield and ultimate strength, and used to connect the yield point, and the ultimate strength stress.

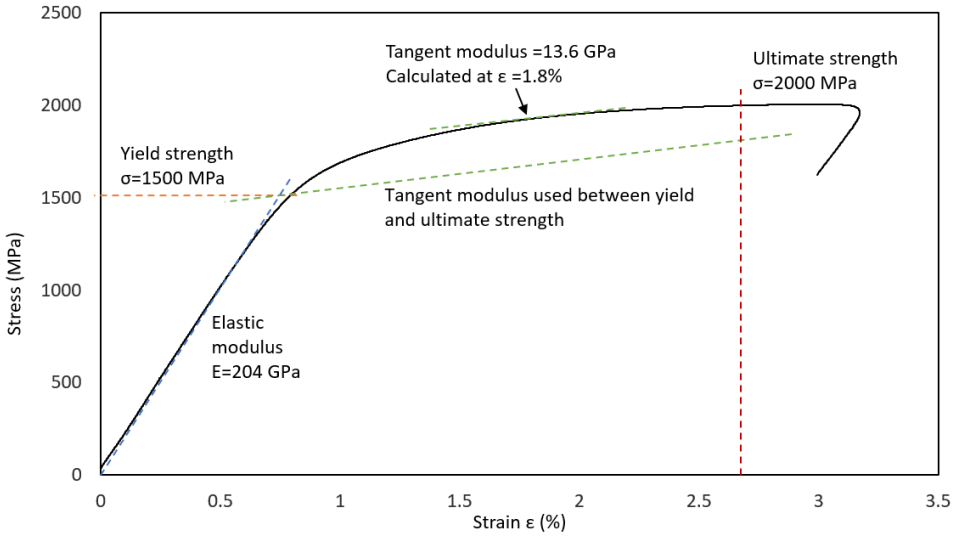

Figure 7.2: stress-strain curve for 300M steel [70], data used in FEM model.

This bilinear approximation lowered the stress of the plastic range and created a sharp transition around the yield point instead of the rounded knee of the stress-strain plot, as seen in Figure 7.2. Residual stress is dependent on the strain experienced during plastic deformation, which will cause this model to produce lower residual stress values than the expected from experimental results. It may be recommended, for future research, to rerun this model with a higher yield strength so that the tangent modulus segment better matches the plastic region of the stress-strain plot. This was not done for this research because it was decided to keep the yield strength the same for all the stress calculation methods conducted.

The model was used to predict the plastic and residual stress and strain on the center top and bottom surfaces of the sample, where the MBN probes would be. The prediction was done for ten strand-alone simulations for the downward applied displacement and unload of the top contact pins from 4.5 mm to 9.0 mm, at 0.5 mm increments. Figure 7.3 gives an example of the predicted von Mises residual stress distribution results after the 6.0 mm displacement of the top contact pins.

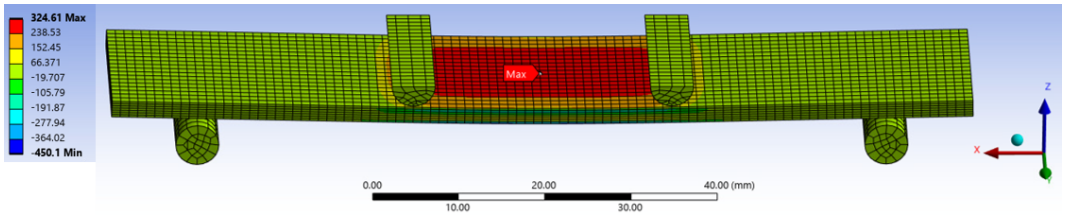

Figure 7.3: ANSYS model for the von Mises residual stress (MPa) after 6.0 mm displacement of the top pins.

This stand-alone approach should provide a good approximation to the experimental set up, since it is assumed that the applied stress can not exceed yield and is therefore, not influenced by previously loaded states. Further details on the simulation sequence and model parameters are in Appendix G.

7.2 Method

This experiment was conducted with four 300M samples with material properties and dimensions as discussed in Section 3.2. Three of the samples were used for MBN measurements in bending, labelled A, B, and C, and the fourth sample was equipped with a strain gauge and labelled G (for gauge).

The experiment was divided into four parts:

1. Strain gauge bending;
    - Conducted with 300M Sample G.
2. Sample elastic bending;
    - Conducted with 300M Samples A, B and C.
3. Sample plastic bending;
    - Conducted with 300M Samples A, B and C.
4. BH curve measurements.
    - Conducted with 300M Samples A, B and C.

Part 1 uses the strain equipment shown in Section 3.1.3 to record micro-strain values for Sample G in bending, following a similar procedure as the strain measurements for the elastic bending experiment, Section 5.2.2. The sample is placed in the four-point bending apparatus with the gauge side down and the bottom probe removed, as shown in Figure 7.4. The sample undergoes the same bending increments as Part 2, which is listed in Table 7.2, and records the average of three strain values for both the plastic loaded and unloaded states. Top MBN probe readings are not included in this experiment's dataset because elastic tensile MBN measurements could not be taken with the strain gauge attached.

Table 7.2: 300M Sample bending increments and applied stresses.

Bending	Deflection (mm)	Stress (MPa)	Increments
Elastic	0 - 3.39	0 - 1300	100 MPa or 0.26 mm
Yield zone	3.65 - 4.31	1400 - approx. 1650	50 MPa or 0.16 mm
Plastic	4.5 - 9.0	estimate 1650-1800	0.5 mm

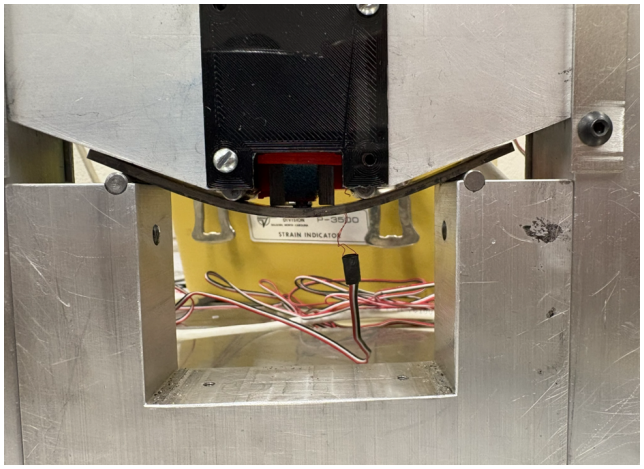

Figure 7.4: Strain gauged Sample G in bending, final deflection of 9.0 mm.

Part 2 was similar to the previous experiment for elastic bending, Section 5, but measurements are taken at 50 Hz excitation frequency, rather than 30 Hz. The change was made to facilitate comparison of the results with previous research, [44],[49] and [71]. The purpose of Part 2 was to establish an elastic tensile stress MBN response calibration curve to compare the tensile residual stress response in Part 3 below. To this end, Samples A, B, and C underwent 13 bending increments from 0 mm to 3.13 mm (which corresponds to 0-1200 MPa) measuring the MBN response for loaded tensile stress at each increment.

This procedure changed after Sample A, because there were slight differences between the top and bottom probe. This resulted in an elastic stress calibration curve from the bottom probe, which did not match the tensile residual stress response of the top probe. To address this, the bending apparatus was modified to allow the top probe to be positioned either above or below the sample. This way, Samples B and C were bent elastically with the top probe positioned below it to gather the tensile stress responses, which was then repositioned above for Part 3.

Part 3, plastic bending, was conducted with Samples A, B and C flipped in the bending apparatus so that the surface that was in tension for Part 2 would be facing up. The bending increments were the same for the elastic bending as in Part 2 and continued into the plastic region, as listed in Table 7.2, taking MBN tensile stress measurements with the bottom

probe. In the plastic range, the bending load was removed by returning the deflection to 0 mm, for every 0.5 mm increment from 4.5 mm to 9.0 mm. During these ten offloaded intervals, MBN measurements were taken with the top and bottom probes for residual tension and compression responses, respectively.

Analysis for the MBN results of Parts 2 and 3 involved plotting the MBN energy against applied stress for 0.4 T and 0.8 T flux levels. The residual stress was then estimated by comparing the MBN energy response with the calibration curve from the relationship between MBN response and elastic tension measured in Part 2. These calibration curves were derived for each sample separately for both 0.4 T and 0.8 T flux levels. The final bent stress states of each sample was taken as the average between the 0.4 T and 0.8 T flux stress calibration curve results. This stress estimation method was then compared to the FEM analysis, strain gauge calculations and bent profile measurements.

The procedure for **Part 4** was the same as the BH curve measurements in Section 3.1.5 for hysteresis plots measured with 2 Hz excitation frequency. Samples A, B and C had nine nested hysteresis loops measured before being bent for Parts 2 and 3, and then again after being bent. Following plastic deformation, the samples' BH curves are measured twice; by magnetizing from the concave side (side up) and convex side (side down), as shown in Figure 7.5. The purpose of this part of the experiment was to explore whether hysteresis plots could discern changes due to plastic deformation, and if they could support the MBN results. The Włodarski model [8][7], discussed in Section 4.1, is used to analyze the hysteresis loops and qualify the differences between the unbent and bent sample results.

Figure 7.5: Three sets of BH curve measurements for Samples A, B, and C; one before and two after plastic bending.

The **analysis procedure** for this experiment involves estimating the residual stress in the bent samples for comparison with the MBN response to residual stress estimation method. The three stress analysis methods were:

1. Strain measurements with plastic zone extrapolation;
2. ANSYS model; and
3. Bent profile measurements with radius of curvature calculation.

The first two methods are discussed in the background section for this experiment, Sections 7.1.1 and 7.1.2. The loaded strain measurements provide ϵ_{max} for the Equation 7.1.1, which can be used to find the residual stress values. The sample and four contact pins of the bending apparatus are modelled in ANSYS to provide FEM results of residual stress. The samples' bent profile is measured by the milling machine, as covered in Section 3.1.4. The deflection values along the length of the sample provide, y_0, which can be plotted as a parabola and differentiated twice for Equation 7.1.1.

7.2.1 Assumptions

Assumptions for this experiment include those made for the previous two experiments, covered in Sections 4.2.1 and 5.2.3, with additional considerations made for the plastic bending regime. There are two main considerations that affect stress and strain calculations and measurements in the plastic regime;

1. 300M behaves as an elastic-perfectly plastic material; and
2. the initial sample state has consistent properties throughout the thickness and no internal stress.

The first consideration affects residual stress calculations and allows for the assumption of:

- Linear relationship between surface strain and curvature of radius to allow for direct calculation of residual stress from bend profile measurements;
- Linear relationship between plastic zone height, h_p and bending deflection, δ, [40] to allow for plastic stress calculations beyond the strain measurements;
- Linear stress distribution through the sample thickness during unloading, which allows for the superposition of Equation 7.1.4; and
- symmetric residual stress distribution about the center chord of the sample, as shown in Figure 7.1.

This results in equal and opposite residual stress distributions on the top and bottom of the sample, as shown in Figure 7.1, as well as a direct relationship between strain and radius of curvature produced by bending. This is key to permitting the bending calculations and residual stress calculations, as shown in Appendix B, for 300M.

The second consideration assumes that there is no initial stress in the samples before they are plastically deformed. This is an extension of Condition 1, since, if 300M is a linearly elastic material, then it can be bent elastically multiple times without producing residual stress or cyclical fatigue. This is important to note because Samples A, B and G were also used in the elastic bending experiment Section 5. Furthermore, the anisotropy tests in Section 3.2.2 showed that the 300M sample didn't have a directional magnetic bias due to surface stresses from rolling or grinding, compared to the AISI 4340 or HY80 samples. This supports the assumption of zero initial stresses present in the samples prior to bending.

7.2.2 Sources of Error

Sources of error for this experiment include those from the previous two experiments, covered in Sections 4.2.2 and 5.2.4, specific for the 300M samples, as well as additional uncertainties for plastic bending and MBN energy measurements at 50 Hz. There are two types of uncertainty for this experiment; the variation in MBN energy measurements, which is covered by the repeatability test, and uncertainty in relation to the strain measurements and stress calculations. The data collected for these tests can be referenced in Appendix E.

7.2.2.1 Repeatability test

Repeatability tests were conducted to discern the variations in MBN energy across the samples' surface at 50 Hz, as discussed in Section 5.2.4.2 for 30 Hz. The variation in MBN energy was determined by the standard deviation of 20 total measurements taken with the top and bottom probes of two different 300M samples. The results of this test are shown in Table 7.3 for 0.4 T and 0.8 T flux levels at 50 Hz and applicable for both probes.

Table 7.3: Average MBN energy variation at 0.4 T and 0.8 T flux and 50 Hz excitation for 300M samples.

Flux (T)	Ave. MBNe (mV^2s)	Variation (mV^2s)	Difference
0.4 T	360	59	16 %
0.8 T	867	101	12 %

7.2.2.2 Stress and strain uncertainty

Sources of uncertainty for applied stress values come from the precision of the deflection gauge measurements, as previously captured with the initial set up trials shown in Table 5.2. Applied stress was also measured by strain gauge, which showed some variation between repeat measurements in the elastic regime, Section 5.2.2, possibly due to the strain gauge relaxing with repeated loading. Ideally, these sources of stress measurements (deflection gauge and strain gauge) would give the same result, but they don't agree within uncertainty, which is shown in the results of Section 7.3.1. The uncertainty calculations for applied bending stress were derived from the standard deviation difference between the expected stress (from bending calculations and the stress-strain plot for 300M) and the stress derived from strain measurements. This process and the resultant uncertainty are shown in Appendix H.

7.3 Results

The results are broken down into three subsections for each part of the experiment; Part 1 strain gauge sample bending, Parts 2-3 elastic and plastic bending and Part 4 BH curve measurements.

7.3.1 Part 1: Strain gauge bending

The strain gauged Sample G, was deflected from 0 - 9.0 mm and strain measurements taken for deflection increments from 0-7.0 mm, since the gauge broke at 7.5 mm. The resulting stress-strain curve for the applied bending load is shown in Figure 7.6. In the elastic region, the strain measurements were used to calculate stress by Hooke's law, Equation 3.1.1 (grey

data in Figure 7.6) and compared to the stress from bending calculations, Equation B.1.7 (yellow data in Figure 7.6). The yield point was reached around 4.3 mm deflection, which was identified by a divergence between the measured elastic strain calculations and the stress by bending calculations. In the plastic zone, stress was calculated based on the height of the plastic zone, h_p, determined from the loaded strain measurement, up to 7.0 mm deflection (blue data in Figure 7.6). From 7.0-9.0 mm deflection, the stress calculations were based on a linear extrapolation of the plastic zone, h_p (green data in Figure 7.6).

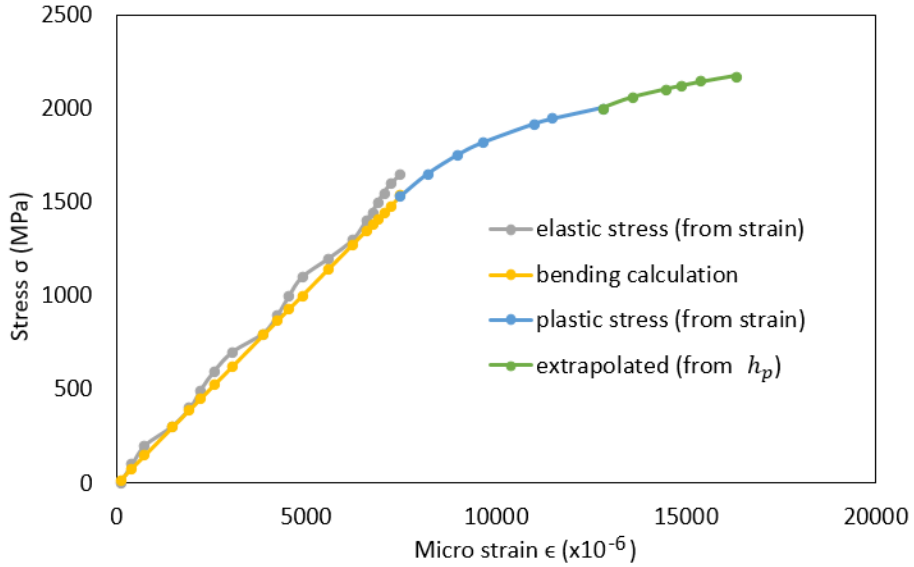

Figure 7.6: stress-strain plot for 300M with measured strain (grey), calculated stress (yellow) and a combination of calculated stress from measured strain in the plastic regime (blue and green).

It may be noted that the bending stress derived by plastic zone, h_p, extrapolation exceeds that of the ultimate strength of 300M, 2000 MPa, as shown in previously measured stress-strain plot, Figure 7.2. At 9.0 mm deflection, the plastic zone height is 75% of the sample's thickness and 2177 MPa loading. To estimate ultimate strength with this method, setting the plastic zone height to 99% gives 2244 MPa loading, which would occur at 10.7 mm deflection. Residual stress at this theoretical extreme would be 744 MPa, which puts an upper bound on what can be expected from the experimental results.

These strain gauge results from Sample G were used to assign stress values to bending

deflections for Samples A, B and C during Parts 2 and 3. In the elastic regime, the stress for deflection was taken as the average of the strain measurement and the bending calculation. In the plastic regime, the strain measurements provided the stress by the height of the plastic zone, h_p, calculations. The resulting elastic and plastic stress by loaded strain is shown in blue in Figure 7.7. These calculations, error bar derivations and a table of stress versus bending deflection are shown in Appendix E.

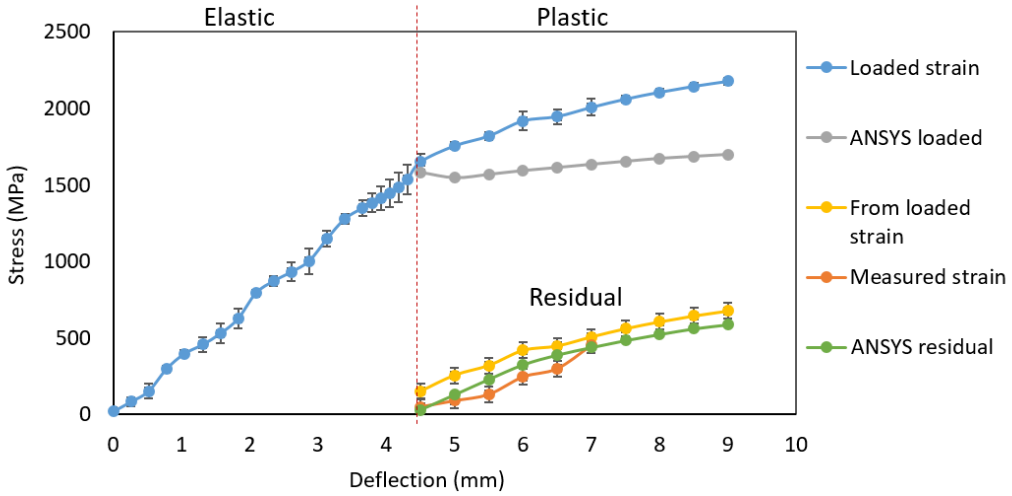

Figure 7.7: Strain gauge results for full bending range, compared with FEM results for plastic deformation and residual stress.

Residual stress was derived using strain measurements in two ways; from calculations with the loaded strain, ϵ_{max}, and from measuring the residual strain directly from the gauge in the offloaded state. Figure 7.7 shows the residual stress by loaded strain in yellow and residual stress from measured residual strain in orange. The ANSYS model residual stress results are shown in green in Figure 7.7 and the loaded stress state is shown in grey. Table 7.4 compares these three sets of data.

The results from this comparison provides some interesting insights. First of all, the ANSYS model residual stress (green data in Figure 7.7) closely trends with the experimental residual stress from strain data and falls between the two measured strain data sets (yellow and orange in Figure 7.7). Loaded stress from this model (grey data in Figure 7.7) is expected to be lower than the experimental stress because of the approximation used to

input the stress-strain data for the model, as shown by Figure 7.2.

Table 7.4: Comparison of residual stress calculated from measured loaded strain, residual strain and the ANSYS model.

Deflection (mm)	**From residual strain (MPa)**	**From loaded strain (MPa)**	**ANSYS model (MPa)**
4.5	50 ±52	150 ±52	29
5	90 ±52	255 ±52	128
5.5	131 ±52	319 ±52	229
6	246 ±52	418 ±52	324
6.5	300 ±52	446 ±52	389
7	451 ±52	506 ±52	438
From extrapolated strain			
7.5	nil	560 ±52	484
8	nil	605 ±52	524
8.5	nil	644 ± 52	561
9	nil	677 ± 52	588

7.3.2 Part 2-3: Elastic and plastic bending

Each sample was bent up to 9.0 mm deflection, except Sample A, which failed at 8.2 mm deflection. The failure was noticed by a sudden drop in resistance to the bending load, so the sequence was stopped there and recorded as the final deflection for the sample. The bent samples' final plastic deformation profiles were measured with a milling machine as discussed in Section 3.1.4. The radius of curvature of the permanent bend was related to residual strain with Equation 7.1.1 at the center of the sample. These measurements and calculations are shown in Appendix I. The results for maximum loaded deflection, residual deflection and residual stress approximated by bent profile for each sample are summarized in Table 7.5.

The MBN energy responses to stress were recorded by flux sweep from 0.1-0.8 T for each bending increment. Figure 7.8 shows a typical set of flux sweeps from the bottom probe for the full bending range up to 9.0 mm deflection. To simplify the analysis, two flux levels, 0.4 T and 0.8 T were selected for assessment of the samples.

Table 7.5: Samples' final plastic deflection and residual stress by bent profile measurements.

Sample	Max deflection	Residual deflection	Residual stress by profile measurements
A	8.2 ± 0.1 mm	1.84 ± 0.10 mm	660 ± 30 MPa
B	9.0 ± 0.1 mm	1.31 ± 0.07 mm	620 ± 30 MPa
C	9.0 ± 0.1 mm	1.40 ± 0.07 mm	660 ± 30 MPa
G	9.0 ± 0.1 mm	1.68 ± 0.08 mm	840 ± 40 MPa

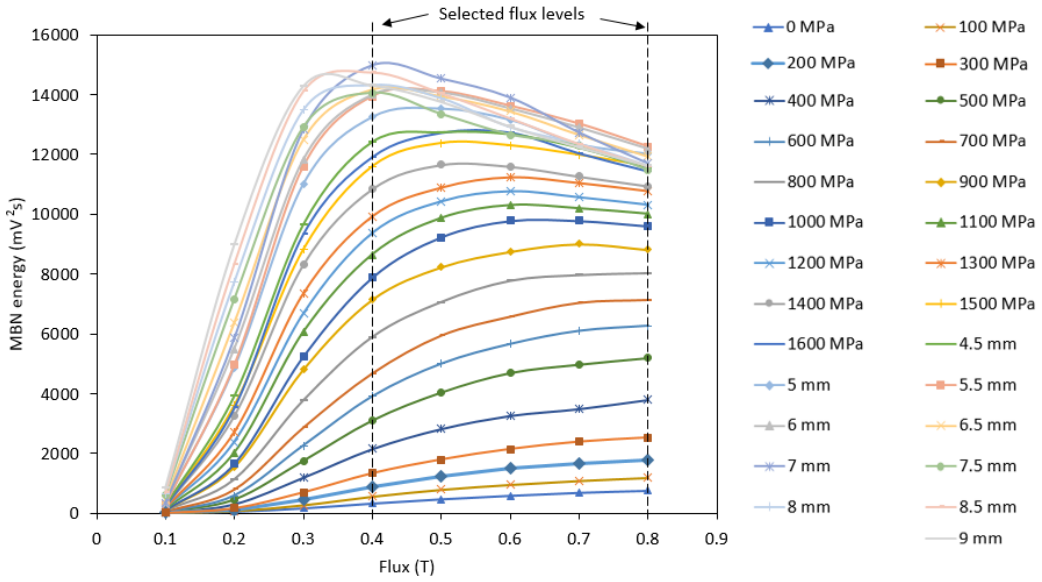

Figure 7.8: A typical flux sweep data set for MBN energy response to increasing tensile stress (Sample B data shown).

0.4 T flux was selected due to its sensitivity to stress, as can be seen by the shape of the flux sweep curves in Figure 7.8, which crest in MBN energy around 0.4 T at the higher stress and bending increments. Kashefi *et al.* [44] and Mandache *et al.* [66] identified that lower excitation fields produce a lower number Barkhausen events than higher fields, but a greater increase in change of MBN energy with DW refinement caused by applied stress. Higher excitation fields, such as 0.8 T, approach saturation of the magnetic circuit between the probe and sample. Therefore, it is less sensitive to stress but also less susceptible to air gaps and geometry changes in the circuit. For these reasons, 0.4 T was selected for its stronger response to stress and 0.8 T was selected for its increased likelihood of reproducible MBN

response between the samples.

Figure 7.9 shows the full bending range MBN energy response for the bottom probe of each sample at 0.4 T and 0.8 T flux, respectively. The calculations for the stress values and uncertainty are shown in Appendix H.

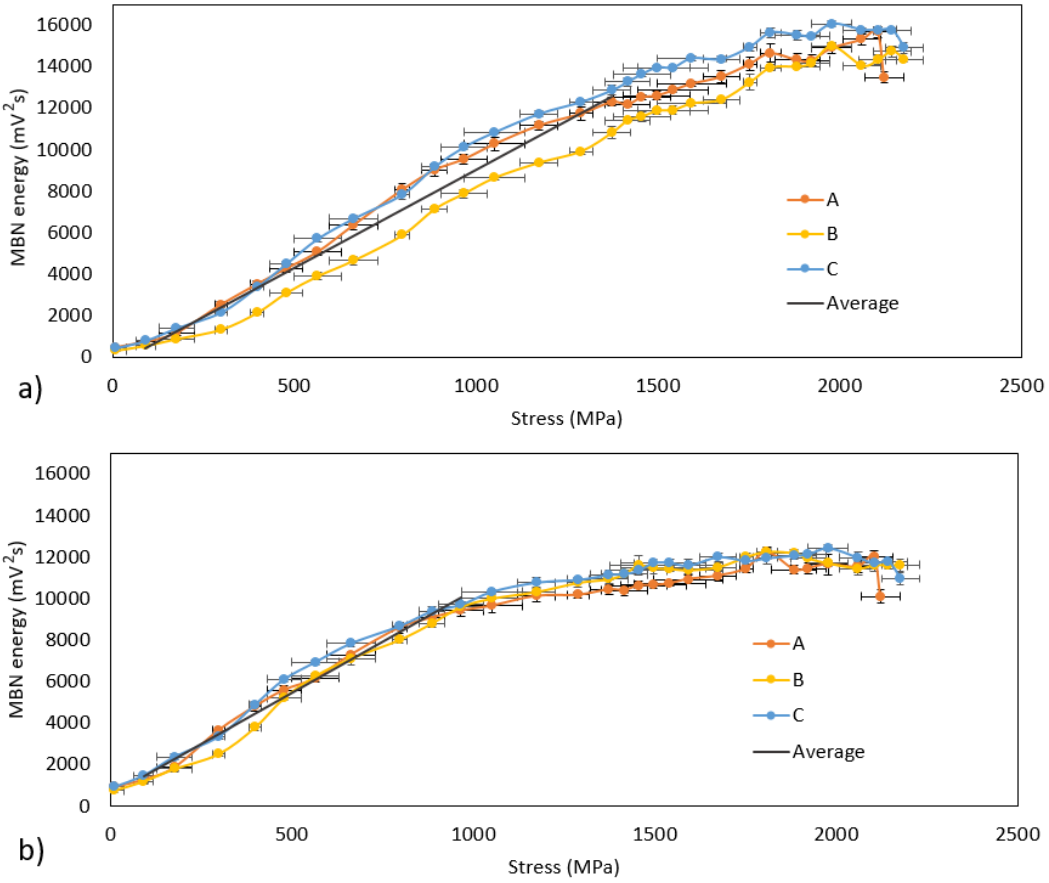

Figure 7.9: MBN energy response to elastic and plastic tensile bending stress (bottom probe) for 300M samples A, B and C at a) 0.4 T flux and b) 0.8 T flux

A linear trend of MBN energy for stress is expected in the elastic stress region, due to the increase in 180° domain walls with tensile stress [63, 72]. Figure 7.9 a) for 0.4 T, shows a near linear trend for most of the bending range (from 0 MPa to approximately 2000 MPa), with a slight decrease in rate around 1400 MPa. At 0.8 T flux level, in Figure 7.9 b), the samples' responses rate decreases with stress around 900 MPa to a near plateau slope.

The linear trends for each sample within a selected range of elastic bending are listed

in Table 7.6 for both 0.4 T and 0.8 T flux. These trends are used as calibration curves to compare the residual stress MBN energy response to an equivalent elastic stress MBN response for stress estimation.

Table 7.6: 300M samples' rate of MBN energy increase with tensile stress for two flux levels.

Flux level 0.4 T			
Sample	**Range (MPa)**	**Calibration slope (mV^2s/MPa)**	**Slope fit (R^2)**
A	90-1375	9.6	0.99
B	90-1375	8.6	0.99
C	90-1375	10.1	0.99
Average	90-1375	9.4	N/A
Flux level 0.8 T			
A	90-970	9.7	0.99
B	90-970	10	0.99
C	90-970	9.8	0.98
Average	90-970	9.8	N/A

Figure 7.10 shows the MBN energy residual stress response by loaded deflection compared to the linear trend response to elastic stress, for 0.4 T and 0.8 T flux levels, for each sample. The black dotted lines show how the calibration curves were used to estimate the final bend residual stress state, by comparing the response to an equivalent elastic stress response. The resulting estimated residual stress state was taken as the average between the 0.4 T and 0.8 T comparison, for each sample (with the exception of Sample A), as summarized in Table 7.7.

Table 7.7: MBN energy response to residual calibrated with elastic stress response to estimate residual stress.

	Calibrated at 0.4 T		Calibrated at 0.8 T		Stress
Samples	MBN energy (mV^2s)	Calibrated stress (MPa)	MBN energy (mV^2s)	Calibrated stress (MPa)	Estimated (MPa)
A	3670 $\pm$140	410 $\pm$30	6080 $\pm$150	550 $\pm$70	550 $\pm$70*
B	4630 $\pm$110	540 $\pm$70	7000 $\pm$150	530 $\pm$70	540 $\pm$70
C	4890 $\pm$150	600 $\pm$50	6420 $\pm$180	520 $\pm$50	560 $\pm$50

*Sample A estimated stress is solely based on 0.8 T calibration.

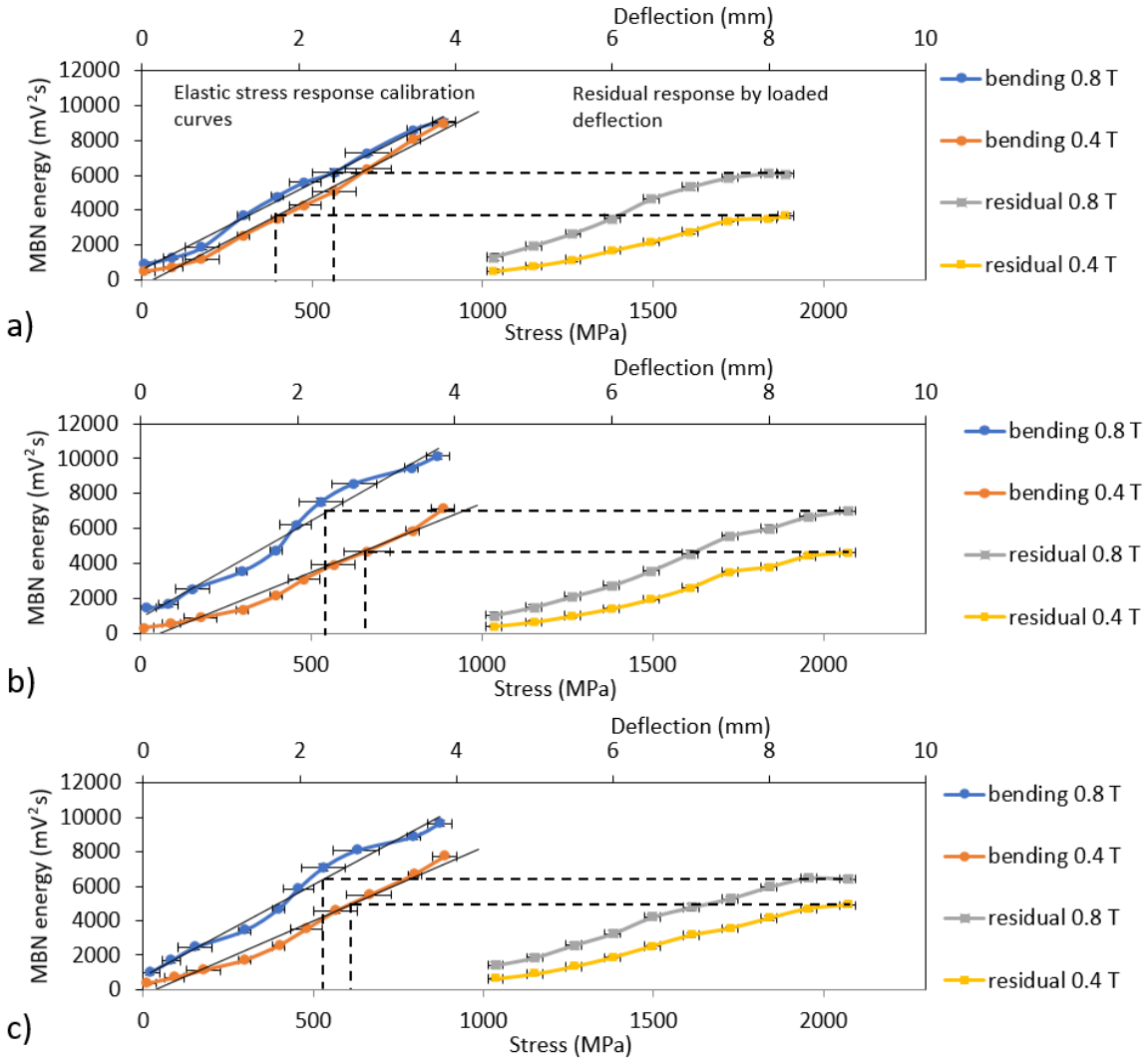

Figure 7.10: Residual stress MBN response compared to tensile bending stress response at 0.4 T and 0.8 T flux levels in 300M samples; a) A, b) B and c) C.

Sample A had the widest spread between its 0.4 T and 0.8 T estimated residual stresses, as shown by the calibration curves in Figure 7.10 a). This is likely due to using the bottom probe to derive the elastic stress calibration curve and compare it with the top probe residual stress response. Repeatability of MBN response between the two probes is improved at 0.8 T flux because the higher flux density increases the saturation of the magnetic circuit so that it is less susceptible to noise. For this reason, Sample A's estimated stress is based on

the 0.8 T flux level calibration, rather than the average of both the 0.4 T and 0.8 T, as was done with Samples B and C.

The consistency between the 0.4 T and 0.8 T results was improved for Sample B and C, since both the calibration curve and the residual stress response were measured with the same probe. The estimated residual stress for all three samples were in good agreement; 540-560$\pm$70 MPa, giving an average of 550$\pm$70 MPa. The experiment endeavoured to apply the same amount of loading to each sample, so even though Sample A was deflected to 8.2 mm and Sample B and C were deflected to 9.0 mm, this result reflects well on the procedure and the MBN calibration method for residual stress estimation.

7.3.3 Part 4: BH curve measurements

BH curve measurements for Samples A, B and C were taken before and after plastic deformation, to explore changes in the magnetic hysteresis behaviour due to bending. Three sets of nested hysteresis loops were measured for each sample; once before bending and twice afterwards, distinguished between magnetizing it from the concave side (side up) and the convex side (side down). The resulting measured BH curves are shown in Figure 7.11.

The initial magnetization curve for each family of nested hysteresis loops was plotted with data from the positive tips of each loop, as discussed in Section 4.1.1. These curves, shown in Figure 7.12 were used to derive the Włodarski model [7, 8] parameters for modelling the hysteresis loops, and they provided a clearer comparison between the unbent and bent BH curves. The initial magnetization curves of the bent samples had, on average, a lower B field than before bending, with no significant difference between being magnetized from the bent side up or down.

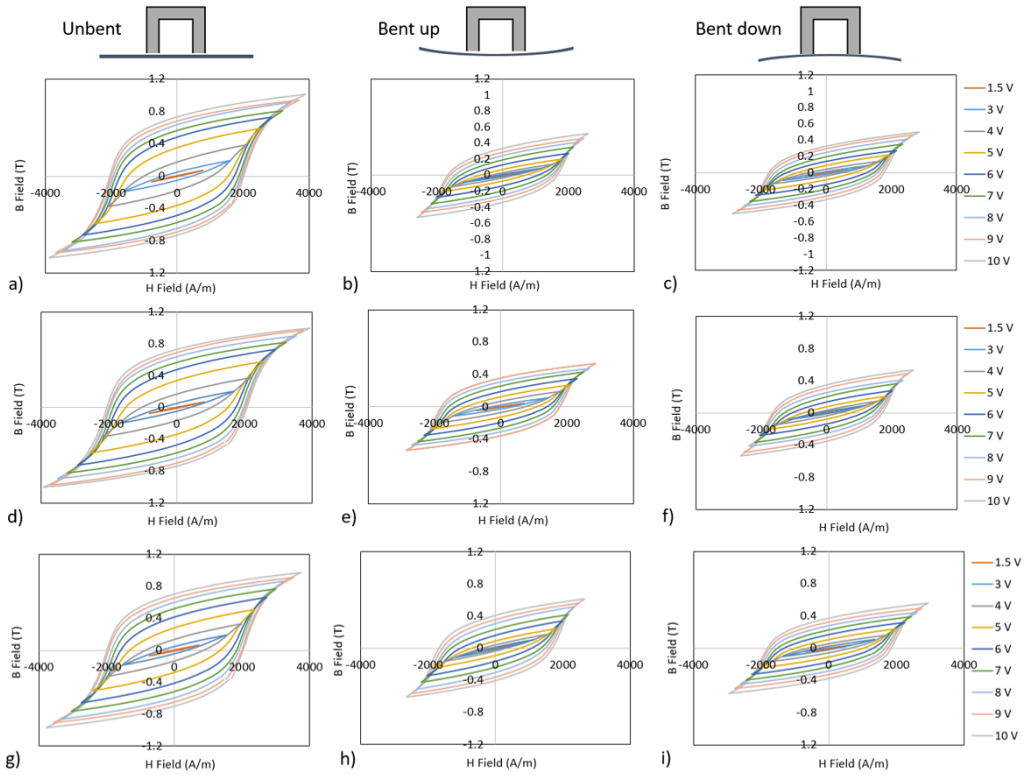

Figure 7.11: Measured BH curves for samples before and after plastic deformation; a) A before bending, b) A magnetized from the concave side, c) A magnetized from the convex side, d) B before bending, e) B magnetized from the concave side, f) B magnetized from the convex side, g) C before bending, h) C magnetized from the concave side, i) C magnetized from the convex side.

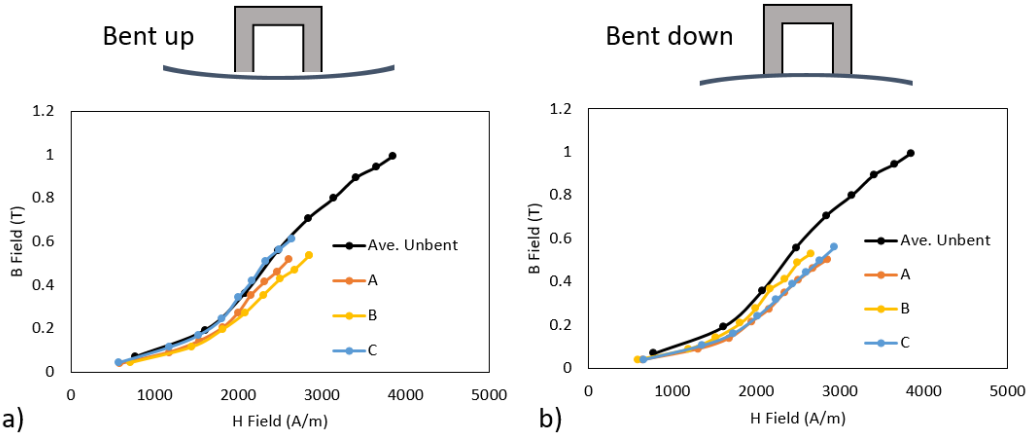

Figure 7.12: Initial magnetization curves of bent samples a) magnetized from side up and b) magnetized from side down, in comparison with the average unbent initial magnetization curve.

The Włodarski model [7, 8] was used to analyze the hysteresis loop differences in magnetic saturation, and reversible and irreversible magnetization terms, as defined by Equation 4.1.11. The model parameters from the initial magnetization curves for each sample can be referenced in Appendix D. The resultant hysteresis characteristics before and after bending are summarized in Table 7.8.

Table 7.8: Magnetic characteristics from initial magnetization curves for samples before and after bending.

Samples	**A**	**B**	**C**	**Average**
Unbent				
Saturation B_s (T)	8.03	8.79	10.1	8.98 ± 0.86
Irreversible B_{irr} (T)	1.04	0.97	0.91	0.97 ± 0.05
Reversible B_{rev} (T)	6.99	7.82	9.19	8.00 ± 0.91
Permeability μ_r	212	207	211	210 ± 2
Bent: Magnetized side up				
Saturation B_s (T)	8.72	8.09	10.6	9.13 ± 1.06
Irreversible B_{irr} (T)	0.55	0.74	0.56	0.62 ± 0.09
Reversible B_{rev} (T)	8.17	7.35	10.0	8.51 ± 1.12
Permeability μ_r	158	149	184	164 ± 15
Bent: Magnetized side down				
Saturation B_s (T)	8.43	9.69	8.37	8.83 ± 0.61
Irreversible B_{irr} (T)	0.54	0.61	0.75	0.63 ± 0.09
Reversible B_{rev} (T)	7.89	9.09	7.62	8.20 ± 0.64
Permeability μ_r	140	158	152	150 ± 7

Table 7.8 provides some interesting comparisons with regards to the magnetic characteristics from the Włodarski model:

- The magnetic saturation does not differ significantly with plastic deformation; the unbent saturation is the average between the bent side up and side down value.
- The irreversible magnetization components decrease with plastic deformation by approximately a third, while this decrease is balanced by an increase in the reversible magnetization component, for both bent side up and down.
- The maximum relative permeability decreases with plastic deformation, but this may be due to the shorter H field range measured for the bent samples, meaning the knee of the magnetization curve may not have been reached.

7.3.3.1 Bent and unbent comparison at H_m= 2385 A/m

The Włodarski model [7, 8] was used to compare the hysteresis loops of the samples before and after bending at an H field strength of $H_m = 2385$ A/m. This H field strength was selected because it was an experimental loop for unbent Sample C and fell within the measured range of all unbent samples. Sample C's experimental data was used for this comparison, because it most closely followed the average unbent initial magnetization curves. Figure 7.13 shows this comparison, where the blue loop is the experimental data for the average unbent sample, the orange loop shows how well the model matches the unbent data, and the yellow is the average bent modelled data. The error bars represent the range of the model results from the four bent samples. Model parameters used for this comparison are shown in Appendix D.

One of the benefits of the Włodarski model is that it can be used to model any H field strength, which made this comparison possible. Figure 7.13 shows that bending the sample affects the samples' hysteresis loop by reducing the B field amplitude by 0% to 33% with an average reduction of 17%. The coercivity intercept increased slightly (higher H field amplitude), which may be indicative of the MBN envelope peak shifting with residual stress, which is discussed in Section 8.2.2.

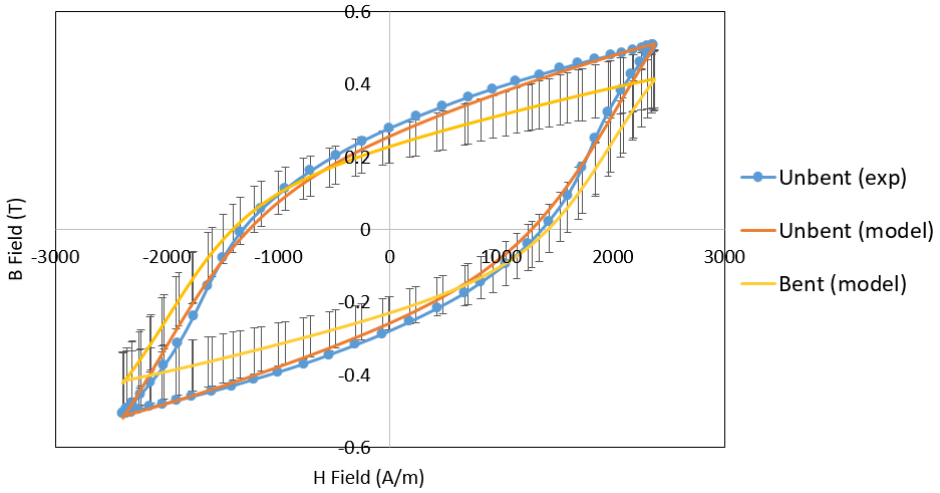

Figure 7.13: BH curve for average bent sample compared with unbent Sample C at H_m = 2385 A/m 300M Samples.

8 Discussions

This section discusses the results from the third experiment with respect to two main topics; magnetic hysteresis measurements to which the Włodarski model was applied, and MBN response to stress.

8.1 The Włodarski model for 300M sample hysteresis

Hysteresis loops were measured for two different widths of 300M samples; 9.4 mm for the hysteresis plot experiment, Section 4, and 19.0 mm for the plastic bending experiment, Section 7. Figure 8.1 shows the initial magnetization curve plotted from the positive tips of the measured nested hysteresis loops for the two sets of 300M samples. The narrower sample, S1, measured loops with larger B field amplitude than the wider unbent samples A, B and C. This may be due to flux dispersing more in the wider samples so the B field outside the sample is weaker for the Hall sensors.

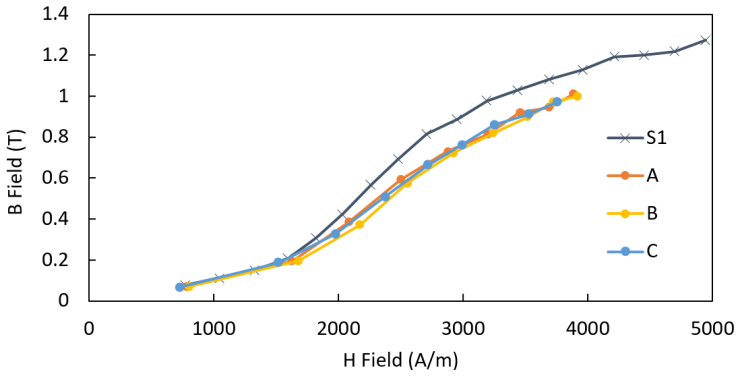

Figure 8.1: Initial magnetization curves for the narrower 300M sample S1 and the wider, unbent Samples A, B and C, which was used to determine the Włodarski model parameters.

The Włodarski model parameters [7] were derived from the initial magnetization curve, so these values may present a way to quantize and compare the differences observed in experiments. Appendix D lists all the samples' model parameters and Table 8.1 summarizes the comparison between Sample S1 and the wider Samples A, B and C. The main difference between the two sets of 300M parameters is the reversible magnetization components; M_a and a. Sample S1's reversible component, M_a, was seven times smaller than the average for Samples A, B and C, which results in a magnetic saturation value approximately four times lower for Sample S1. It is interesting to note that the irreversible component, M_b, is very similar between the two sets of data, which is expected, since MBN occurs with the irreversible magnetization process and is not affected by the sample's width.

Table 8.1: Comparison of the reversible and irreversible magnetization parameters of the Włodarski model for the narrow, S1, and wider, A, B and C, 300M samples.

Włodarski parameter	Sample S1	Average of A, B, C unbent
Reversible M_a (A/m)	1.10×10^6	7.32×10^6
Reversal rate a	5.32×10^3	3.66×10^4
Irreversible M_b (A/m)	8.00×10^5	7.28×10^5

8.1.1 Magnetic circuit geometry

The geometry change between the straight and bent sample affected the magnetic circuit of the probe and sample. The probes for both the hysteresis plot and the bending experiments, had the same shape and material as the MBN system U-core probe, which are ideal for flat contact with the sample. When the U-core is magnetizing a bent sample, the contact shifts to the inner edges of the poles on the convex side (side down) of the sample, or the outer pole edges on the concave side (side down) of the sample. This reduces the contact area, increasing the air gap between the probe and the sample and either shortens or lengthens the flux path, as shown in Figure 8.2 a) and b), respectively.

Both cases are expected to cause a reduction of flux density in the magnetic circuit due to the smaller contact surface between the U-core and sample, and, in the case of the convex side, the longer flux path. This is supported by the results presented in Section 7.3.3, which

shows the BH curve measurements after bending have lower average B field amplitude than before bending. The prediction of longer flux path affecting the hysteresis loops is not supported by the experiment, as Figure 7.12 does not show a significant difference between bent up and bent down initial magnetization curves.

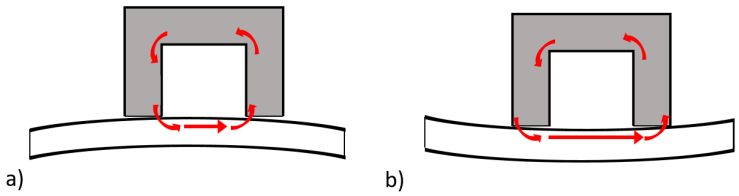

Figure 8.2: a) The flux path is shorter when magnetized from the convex side down and b) longer flux path when magnetized from the concave side up.

Flux across the air gap has a greater effect on the magnetic circuit than the path length through steel, since the relative permeability of air is $\mu_r = 1$, the Supermendur U-core has a permeability of $\mu_r = 6.6 \times 10^4$ [52], and the 300M sample has approximately $\mu_r = 243$, as shown in Table 3.5. Therefore, the reduction of contact area, and increase in air gap between the U-core and the sample due to the bent curvature are the main cause of lower average B field amplitude in the bent hysteresis plots.

The MBN measurements were taken by flux control, which accounts for the differences in flux path and air gap between Figure 2.1 a) and b). This is important because the MBN calibration method for residual stress estimation assumes elastic stress response with the geometry of Figure 2.1 a) can be related to the residual tensile stress response with Figure 2.1 b) geometry. This being said, the stress distribution through the thickness of the sample may influence the flux's path in the circuit, even though the overall flux is being controlled.

Referencing Figure B.5 for a depiction of residual stress through a bent sample, the top surface has residual tension, the bottom surface is in compression and the average stress across the sample is 0. A similar stress distribution was also found by Clapham *et al.* [43]. Under active loading, the stress distribution through the sample can be represented similar to the linear unloading stress distribution step in Figure B.5. The MBN calibration method for

residual stress estimation assumes that MBN measurements resulting from the flux through these two stress distributions can be compared directly.

The skin depth Equation 2.1.7 is used to estimate how much of this stress distribution the magnetic flux and resulting MBN signal encounters. An excitation frequency of 50 Hz has a skin depth of 3.3 mm into the sample, while the 300M samples were 2.2 mm thick, so the affect of stress distribution on flux transfer, can be assumed to be negligible. MBN signal has an average frequency of 200 kHz [10], which has a penetration depth of 0.16 mm in 300M, as shown in Table 3.5. At this small depth from the surface into the sample, the stress distribution changes more rapidly for the bent sample (residual stress) than the actively loaded sample. Further research is required to determine if this has a significant affect on the flux path.

8.2 MBN response to stress

This section discusses how MBN energy responds to bending stress for both the elastic and plastic bending regimes. It should be noted that the two experiments that explored MBN energy response to stress were conducted at different excitation frequencies; 30 Hz for the elastic stress bending experiment in Section 5 and 50 Hz for the plastic bending experiment Section 7. This frequency also affects the MBN response and, for brevity, this topic can be referenced in Appendix F. This section focuses on the results of the plastic bending experiment, Section 7, and the MBN energy calibration method used to estimate residual stress, in comparison with the three other stress estimation methods.

8.2.1 Residual stress estimate methods

The plastic bending experiment estimated residual stress in the 300M samples by four methods, which were compared for the final bent state of Samples A, B, and C, as shown in Table 8.2. The MBN response method gave a residual stress estimation from the average of 0.4 T and 0.8 T flux calibration results, for each sample. Sample A was an exception to this method and only used 0.8 T measurements because different probes were used for the

calibration and residual stress response. The higher flux level provided better agreement between the different probe data sets.

Sample A failed at 8.2 mm deflection for the final bend, whereas Samples B and C were deflected up to 9.0 mm without noticeable loss of strength. The ANSYS model and strain calculation methods estimated a lower residual stress value in Sample A, compared to the other two, because these method base their residual stress estimates were dependent on the deflection amount. The MBN response and profile methods based their estimates on sample measurements that were independent from the active bending deflection and showed similar stress states for all three samples.

Table 8.2: Summary of stress estimation results for the four methods used.

Method of stress estimation	**Sample A (MPa)**	**Sample B (MPa)**	**Sample C (MPa)**	**Average (MPa)**
MBN response	550±70*	540±70	560±50	550±70
ANSYS model	560	590	590	580
Strain calculations	620±50	680±50	680±50	660±50
Profile measurement	660±30	620±30	660±30	650±30

*MBN estimated stress for Sample A is solely based on 0.8 T measurements.

The MBN response method was based on calibration curves derived for each sample individually, from their elastic stress response, which was then used to fit the residual stress MBN measurements for the estimation. This method gave the lowest stress estimations, with the highest uncertainty, of the four methods. The ANSYS model calculations were within the uncertainty bounds of the MBN response, but due to the model's stress-strain curve approximations shown in Figure 7.2, the stress results were expected to be underestimations. The model parameters and simulation method are covered in Appendix G.

The strain calculation and profile measurements gave the highest residual stress results and agreed within uncertainty. These methods were based on the stress analysis and bending calculations covered in Appendix B. The stress calculations were carried out with the strain gauge measurements from Sample G, which are shown in Appendix H. The sample profile measurement data used for this method can be referenced in Appendix I. Since both methods measured strain directly from the samples, their residual stress measurements are considered

the most accurate of the four methods used, until the samples' stress state can be confirmed with X-ray or neutron diffraction.

8.2.2 MBN response to plastic bending

The plastic bending experiment, Section 7, measured the MBN energy response to elastic and plastic bending, and residual stress conditions at 50 Hz excitation. The results were used to propose a method of estimating residual stress that relies on comparing the MBN energy response to residual stress with the calibration curve of the elastic stress response, specific to each of the 300M samples.

This method assumes a linear relationship between the MBN energy response and elastic stress across a specific range; 90-1375 MPa for 0.4 T flux level and 90-970 MPa for 0.8 T flux level, as shown in Table 5.4. This approach of deriving a calibration curve from the elastic stress MBN response has been explored by Gauthier *et al.* [73], and others [42, 49, 74]. Another approach in literature has demonstrated a linear relationship between residual stress and MBN energy [75]. Elastic and residual stress do not have the same stress distribution through the thickness of the material in bending. As shown in Figure 7.1 and research by Clapham *et al.* [43], residual stress can be calculated as the difference between stress during loading, which exceeds the yield stress at the surface, and an assumed linear unload. The plastic deformation caused by loading the sample in bending beyond yield, is at a maximum on the surface, which the MBN signals respond to at an average depth of 0.16 mm for 300M, as shown in Table 3.5.

The calibration method was based on MBN energy response, which is a single value derived from the MBN envelope, that describes the signal response in more detail. MBN envelopes contain information on the shape, width and peak location about how the material magnetizes [44]. Figure 8.3 and 8.4 shows the MBN envelope response for Samples B and C, respectively, for both elastic and residual stress for 0.4 T and 0.8 T flux levels.

The envelopes shown are data from the last magnetization cycle (rather than an average of the 16 cycles, as is the cause for MBN energy response), which has been smoothed by

Savisky-Golay filter and plotted in Matlab. The shape between the elastic and residual stress envelopes differ slightly; the residual stress envelopes seem to lead and trail off sooner than the elastic stress envelopes, with reference to the B field direction, most noticeably for Sample C; Figure 8.4. An MBN envelope peak shift has been documented for residual stress [74], with results being more prominent at lower flux levels [76].

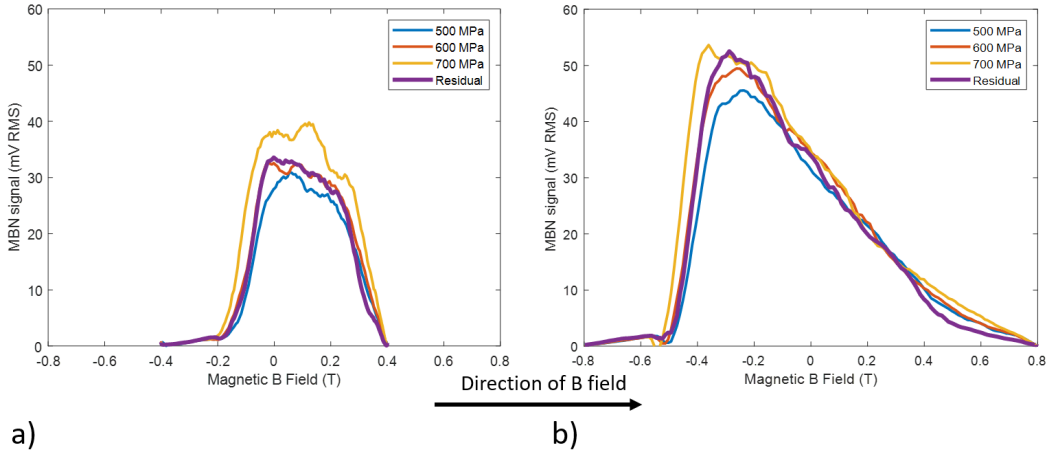

Figure 8.3: MBN envelopes for Sample B showing 500 MPa, 600 MPa and 700 MPa elastic stress compared with the final bend residual stress; a) 0.4 T flux envelopes and b) 0.8 T flux envelopes.

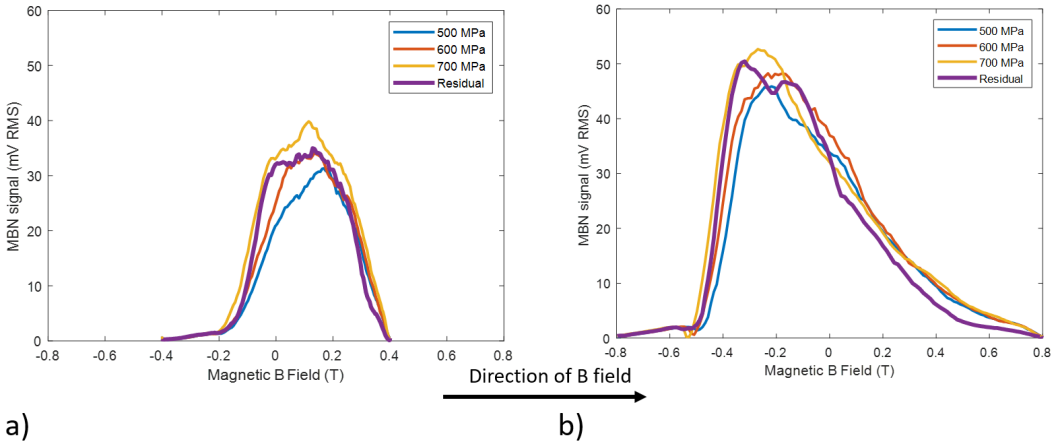

Figure 8.4: MBN envelopes for Sample C showing 500 MPa, 600 MPa and 700 MPa elastic stress compared with the final bend residual stress; a) 0.4 T flux envelopes and b) 0.8 T flux envelopes.

Comparing the residual stress envelope (in purple) with those of the elastic stress response gives a higher stress estimate than the MBN energy calibration method used in the

experiment. The residual stress envelope for Sample C in Figure 8.3 closely matches that for 600 MPa elastic stress, where the calibration curve estimated it at 540 MPa in Table 7.7. For Sample C in Figure 8.4, the residual stress envelope matches above the 600 MPa and just below the 700 MPa elastic stress envelope, compared to the 560 MPa estimate from Table 7.7.

Key characteristics for this comparison are the positions of the leading edge and envelope peak. In Figure 8.3, the leading edge of the residual stress envelope tracks on top of that of the 600 MPa envelope, then the peak has a larger amplidute, for both the 0.4 T and 0.8 T flux measurements. In Figure 8.4, the residual stress envelope leading edge tracks between that of the 600 MPa and 700 MPa envelopes. The envelope peak amplitude is between those two elastic stress envelopes and the peak location is more to the left and leading (by reference to the B field direction) than both elastic stress envelopes at the 0.8 T flux level in Figure 8.4 b). It may be recommended that future research explore a calibration method of matching MBN envelope shape, specifically the leading edge position and peak height of the envelopes to estimate the residual stress, instead of solely MBN energy data.

The MBN envelopes for residual stress may be affected by increased dislocation density that change the microstructure texture when plastic deformation occurs [67][68]. Dislocations act as obstacles to domain wall (DW) movement [41] and high concentrations of dislocations, often at grain boundaries, could cause slip planes, which would limit the size of magnetic domains. These factors could explain the decrease in MBN energy rate with plastic stress, as shown in Figure 7.9 b) for the 300M samples beyond 900 MPa for 0.8 T flux. The dislocations and slip planes may suppress the MBN response and result in an underestimation of residual stress, with the calibrated method that uses elastic stress response. Despite this challenge, other research has found success with elastic MBN calibration curves for residual stress estimates that were confirmed with X-ray diffraction; for tempered AISI 4135 [49], and AISI D2 [46]. Both steels are similar to AISI 4340 and 300M, so this approach has potential to improve with further research.

9 Conclusions and Future Work

This research explored the magnetic behaviour of high strength steel samples with the goal of exploring an MBN energy calibration method to estimate residual stress for applications of developing a portable NDT technique for aircraft landing gear. Three experiments were conducted in support of that objective; measurements of hysteresis loops by the Włodarski model [8, 7], MBN energy response to elastic stress and MBN energy response to plastic stress. This section discusses the main conclusions that came out of this work.

The Włodarski model [8, 7] demonstrated the potential to provide a good approximation of experimental hysteresis for 300M and AISI 4340 samples, but was less accurate for the HY80 sample. The model's accuracy reduced for larger hysteresis loops (greater than 60% of the H field amplitude of the largest experimentally measured loop), which was likely due to the method of deriving model parameters based on the one dimensional initial magnetization curve to model the two dimensional hysteresis loop. This accuracy could be improved by adjusting the model parameters to better fit the experimental loop by minimizing the SSE.

The model related to the MBN signal because it derived reversible and irreversible magnetization values specific to the sample material. MBN is mainly attributed to the irreversible magnetization process, where the 180° domain walls move abruptly in response to an applied magnetic field. The material with the largest irreversible magnetization parameter correlated to the highest MBN energy response, under no stress conditions, and a linear relationship could be plotted between the three sample materials tested.

The Włodarski model [8, 7] proved to be a useful tool in the third experiment for comparing the differences between unbent and bent 300M sample hysteresis at H_m=2385 A/m

field amplitude. This comparison showed that plastic deformation causes a reduction in the B_m field amplitude by an average of 17% $\pm$16%, which implies that there is no measurable reduction within the limits of uncertainty.

The second experiment determined that MBN energy response could be correlated to elastic bending stress with a near linear trend. The MBN energy response increased with tensile stress and decreased, to a plateau, with compressive stress, for all three sample materials. Of the high strength steel samples, 300M showed the most MBN energy responsiveness to stress, which demonstrates potential for this NDT method to be used for aircraft landing gear stress detection.

The final experiment objective was to determine if the MBN response could be used to estimate the residual stress in 300M samples. Calibration curves based on the MBN energy response to elastic stress were used to estimate the residual final bent stress state of three 300M samples. This method provided a residual stress estimation between 540-560$\pm$70 MPa for the final bent state of Samples A, B and C.

The MBN energy method provided the lowest estimated residual stress of the four methods used; MBN energy response, ANSYS model, strain gauge calculations, and bent profile measurements. The strain gauge and profile measurement methods show good agreement and provided the most reliable residual stress estimates, which average between 650-660$\pm$50 MPa for the three samples. A comparison of the MBN envelope leading edge and peak position for Samples B and C provided a higher residual stress estimate, between 600-700 MPa, than the MBN energy calibration method. These results show that MBN response calibration method, in combination with MBN envelope analysis, demonstrates the potential to be used as a foundation towards the development of an NDE method for residual stress detection and estimation in 300M steel.

9.1 Future work

The work presented in this thesis, has been limited to thin rectangular samples, which facilitated MBN measurements and applying stress by bending. The samples' stress results

should be verified by X-ray or neutron diffraction to assess the accuracy of MBN response method used. Additionally, in order to asses the real world applicability of this MBN method for use in detecting and estimating the residual stress in CF 188 aircraft landing gear, future research recommendations include:

- Test more samples in order to build up a database of MBN response to stress, which would improve the accuracy of stress predictions.
- Use larger samples to determine the effects of geometry on MBN response to better approximate the properties of the landing gear component.
- Investigate methods for measuring hysteresis at the same frequency and location as MBN measurements. Combined, they may improve the results for stress estimation.
- Explore options for multi-parameter analysis to improve the stress measurement capability by considering multiple inputs (such as frequency, flux, geometry, orientation, and permeability) for determining stress from magnetic responses.
- Assess the suitability of other analytical models for magnetic hysteresis, since the Włodarski model may not be the most applicable for multi-parameter analysis.

This work has demonstrated that MBN is a promising NDE technique to estimate stress in 300M steel because the material produces a large and measurable MBN response to bending stress. Further research is needed to improve the understanding of all the parameters that affect MBN response, most notably geometry, so that results from samples can be standardized and calibrated for determining the residual stress of an aircraft landing gear component.

References

[1] D. Bray and R. Stanley, *Nondestructive evaluation: A Tool in Design, Manufacturing and Service*. CRC Press, revised edition ed., 1997.

[2] S. P. Farrell and L. W. MacGregor, "Application of X-Ray Diffraction for Residual Stress Analysis on Canadian Naval Platforms," 2010.

[3] B. D. Cullity, *Elements of X-Ray Diffraction*. Addison-Wesley Publishing Company Inc., second edition ed., 1978.

[4] A. Fahr, *Aeronautical Applications of Non-destructive Testing*. DEStech Publications, Inc., 2014.

[5] I. SAE, "ARP 4462: Barkhausen Noise Inspection for Detecting Grinding Burns in High Strength Steel Parts," 2019.

[6] B. NDIT, "Depot & intermediate maintenance nondestructive inspection magnetoelastic inspection for residual stress in the main landing gear trunnion (part no. 74a410511)," *Nondestructive Inspection Methods-NAVAIR 01-1A-16*, 2002.

[7] Z. Włodarski, "Modeling hysteresis by analytical reversal curves," *Physica B 398*, pp. 159–163, 2007.

[8] Z. Włodarski, "Analytical description of magnetization curves," *Phys. B Condens. Matter*, vol. 373, pp. 323–327, Mar. 2006.

[9] A. Krause, A. Samimi, R. Underhill, T. Krause, and L. Clapham, "Portable MBN Acquisition System User Manual," *RMC, Kingston ON*, Sept. 2016.

[10] S. White, *A Barkhausen Noise Testing System for CANDU® Feeder Pipes*. PhD thesis, Queen's University, 2009.

[11] B. D. Cullity and C. D. Graham, *Introduction to Magnetic Materials, Second Edition*, vol. IEEE Press. New Jersey: John Wile & Sons, Inc., 2009.

[12] D. Griffiths, *Introduction to Electrodynamics*. Pearson Education, Inc., fourth ed., 2013.

[13] C. V. Dodd and W. E. Deeds, "Analytical solutions to eddy-current probe-coil problems," *J. Appl. Phys.*, vol. 39, pp. 2829–2838, 1968.

[14] M. N. O. Sadiku, *Elements of Electromagetics*. Oxford University Press, seventh ed., 2018.

[15] D. Jiles, *Introduction to Magnetism and Magnetic Marials*. Chapman & Hall/CRC, second ed., 1998.

[16] M. Plonus, A., *Applied Electro-Magnetics*. McGrw-Hill, Inc., 1978.

[17] R. M. Bozorth, *Ferromagnetism*. D Van Nostrand Company, Inc., second ed., 1951.

[18] T. W. Krause, A. K. Krause, P. R. Underhill, and M. Kashefi, "Modeling magnetization processes in steel under stress using magnetic objects," *Journal of Applied Physics*, vol. 131, p. 171101, May 2022.

[19] C.-W. Chen, *Magnetism and Metallurgy of Soft Magnetic Materials*. New York: Dover Publications Inc., 1986.

[20] J. W. Rayleigh, "On magnetic hysteresis," *Philos. Mag.*, vol. 23, no. 5, p. 225, 1887.

[21] F. Preisach, "Über die magnetische nachwirkung," *Zeitschrift für Physik*, vol. 94, pp. 277–302, Feb 1935.

[22] D. Jiles and D. Atherton, "Theory of ferromagnetic hysteresis," *Journal of Applied Physics*, vol. 25, pp. 2115–2120, 1984.

[23] E. C. Stoner and E. P. Wohlfarth, "A mechanism of magnetic hysteresis in heterogeneous alloys," *Royal Society*, vol. 240, pp. 599–642, 1948.

[24] C. R. Pike and R. Andrew, "Characterizing interactions in fine magnetic particle systems using first order reversal curves," *Journal of Applied Physics*, vol. 85, 1999.

[25] X. Du, J. Pan, and A. Guzzomi, "Modeling the hysteresis characteristics of transformer core under various excitation level via on-line measurements," *Electronics*, vol. 7, 2018.

[26] J. Takács, *Mathematics of Hysteretic Phenomena: The T(x) Model for the Description of Hysteresis*. Wiley, 1st ed., 2003.

[27] P. Weiss, "L'hypthèse du champ moléculaire et la propriété ferromagnétique," *J. Phys. Theor. Appl.*, vol. 6, 1907.

[28] H. Barkhausen, "Zwei mit hilfe der neuen verstärker entdeckte erscheinungen," *Physikalische Zeitschrift*, vol. 20, no. 9, pp. 401–403, 1919.

[29] C. W. Heaps, "Optical and magnetic properties of a magnetite suspension," *Physics Review Journals Archive*, vol. 57, 1940.

[30] S. Chikazumi, *Physics of Ferromagnetism*. Oxford University Press, 2nd ed., 1997.

[31] H. J. Williams, W. Shockley, and C. Kittle, "Studies of the propagation velocity of a ferromagnetic domain boundary," *Physical Review*, vol. 80, 1950.

[32] T. W. Krause and A. A. Samimi, "Micromagnetic Techniques," *ASM International*, vol. 17, pp. 515–530, 2018.

[33] K. H. J. Buschow and F. R. De Boer, *Physics of Magneticm and Magnetic Materials*. New York: Kluwer Academic Publishers, 2003.

[34] C. Kittel, *Introduction to Solid StatePhysics*. John Wiley & Sons, Inc, 8th ed., 2005.

[35] G. Dobmann, "Industrial applications of 3ma - micromagnetic multiparameter microstructure and stress analysis," *e-Journal of Nondestructive Testing*, vol. 13, no. 4, 2008.

[36] M. Kashefi, "Development of Magnetic Technique of Inspcetion of Aircraft Landing Gear," 2023.

[37] L. Lebedev, M. Cloud, and V. Eremeyev, *Tensor Analysis with Applications in Mechanics*. Singapore: World Scientific Publishing Co. Pte, Ltd., revised ed., 2010.

[38] J. P. Joule, "On a new class of magnetic forces," *Annales of Electricity*, vol. viii, 1841.

[39] E. Villari, "Ueber die aenderungen des magnetischen moments, welche der zug und das hindurchleiten eines galvanischen stroms in einem stabe von stahl oder eisen hervorbringen," *Annalen der physik*, 1865.

[40] R. G. Budynas, *Advanced Strength and Applied Stress Analysis*. McGaw-Hill, 1977.

[41] C.-G. Stefanita, D. Atherton, and L. Clapham, "Plastic versus elastic deformation effects on magnetic Barkhausen noise in steel," *Acta Materialia*, vol. 48, no. 13, pp. 3545–3551, 2000.

[42] C. Jagadish, L. Clapham, and D. Atherton, "Influence of uniaxial elastic stress on power spectrum and pulse height distribution of surface Barkhausen noise in pipeline steel," *IEEE Transactions on Magnetics*, vol. 26, pp. 1160–1163, May 1990.

[43] l. Clapham, T. W. Krause, H. Olsen, B. Ma, D. L. Atherton, P. Clark, and T. M. Holden, "Characterizatioon of testure and residual stress in a section of 610 pipeline steel," *NDT & E International*, vol. 28, pp. 73–82, 1995.

[44] M. Kashefi, P. R. Underhill, D. Wowk, and T. W. Krause, "Effect of Bending Induced Plastic Deformation on Magnetic Barkhausen Noise Response in HY-80 Submarine Steel," tech. rep., DRDC Halifax, March 2023.

[45] A. A. Samimi, T. W. Krause, and L. Clapham, "Stress Response of Magnetic Barkhausen Noise in Submarine Hull Steel: A Comparative Study," *Journal of Nondestructive Evaluation*, vol. 35, p. 32, Jun 2016.

[46] S. Kahrobaee and M. Kashefi, "Assessment of retained austenite in aisi d2 tool steel using magnetic hysteresis and barkhausen noise parameters," *Journal of Matierials Engineering and Performance*, vol. 24, pp. 1192–1198, 2015.

[47] A. A. Samimi, T. W. Krause, L. Clapham, M. Gallaugher, Y. Ding, P. Ghosh, R. Chromik, and A. M. Knight, "Correlation between ac core loss and surface magnetic barkhausen noise in electric motor steel," *J. Nondestrict Eval.*, vol. 33, pp. 663–669, 2015.

[48] K. Zhu, S. Zhang, P. Li, C. He, and X. Liu, "Effect of tensile stress on the magnetic barkhausen noise near grain boundary in grain-oriented silicon steel: experimental observation," *Meas. Sci. Technol.*, vol. 36, 2025.

[49] J. Chai, J. Zhong, Z. Shen, B. Xu, Z. Zhang, X. Zhan, and J. Shen, "Characterization of the microstructure and residual stress in quenched and tempered aisi 4135 steel using magnetic nondestructive testing techniques," *J. Mater. Eng. Perform.*, Oct. 2023.

[50] S. Santa-aho, A. Sorsa, and M. Vippola, "Barkhausen noise probes and modelling: A review," *Journal of Nondestructive Evaluation*, vol. 38, 2019.

[51] S. White, T. Krause, and L. Clapham, "Control of flux in magnetic circuits for barkhausen noise measurements," *Measurement Science and Technology*, vol. 18, 2007.

[52] H. Gould and D. Wenny, "Supermendur: A new rectangular-loop magnetic material," *Electr. Eng.*, vol. 76, no. 3, pp. 208–211, 1957.

[53] W. Young and R. Budynas, *Roark's Formulas for Stress and Strain*. McGraw-Hill, Inc, seventh ed., 2002.

[54] MechaniCal, "Stresses & deflections in beams," 2014. https://mechanicalc.com/reference/beam-analysis, accessed online Jul. 2024.

[55] VISHAYPG. Item code number MMF309393 Micro-Measurements strain gauges, www.VISHAYPG.com, accessed online Mar. 2024.

[56] Allegro, "A1321, a1322, and a1323: Ratiometric linear hall effect sensor ics for high-temperature operation," 2011. accessed online Nov. 2024.

[57] L. MatWeb, "MatWeb: Material Property Data," 1996. https://www.matweb.com/, accessed online Nov. 2023.

[58] A. I. INC, "Alloy Steel 300M," 2024. https://alloysintl.com/inventory/alloys-steels-supplier/alloy-steel-300m/, accessed online Feb. 2024.

[59] W.-S. Lee and T.-T. Su, "Mechanical properties and microstructural features of AISI 4340 high-strength alloy steel under quenched and tempered conditions," *Journal of Materials Processing Technology*, vol. 87, pp. 198–206, Mar. 1999.

[60] S. International, *AMSH-6875 Heat Treatment of Steel*, 1998.

[61] W. A. Wood, *The Study of Metal Structures and their Mechanical Properties*. New York: Pergamon Press INc., 1971.

[62] R. Eybel, "Hardness test on 300M samples." email, June 2020.

[63] T. W. Krause, L. Clapham, A. Pattantyus, and D. L. Atherton, "Investigation of the stress-dependent magnetic easy axis in steel using magnetic barkhausen noise," *J. Appl. Phys.*, vol. 79, pp. 4242–4252, 1996.

[64] I. D. Mayergoyz, "Mathematical modles of hsteresis (invited)," *IEEE Transactions on Magnetics*, vol. MAG-22, no. 5, 1986.

[65] S. Thompson and B. Tanner, "The magnetic properties of pearlitic steels as a function of carbon content," *Journal of Magnetism and Magnetic Materials*, vol. 123, 1993.

[66] C. Mandache, T. W. Krause, and L. Clapham, "Investigation of Optimum Field Amplitude for Stress Dependence of Magnetic Barkhausen Noise," *IEEE Transactions on Magnetics*, vol. 43, pp. 3976–3983, Nov. 2007.

[67] C. C. H. Lo, E. Kinser, and D. C. Jiles, "Modeling the interrelating effects of plastic deformation and stress on magnetic properties of materials," *Journal of Applied Physics*, vol. 93, pp. 6626–6628, May 2003.

[68] Y.-X. Zhanga, M.-F. Lana, Y. Wanga, F. Fanga, X. Lua, G. Yuana, R. Misrab, and G.-D. Wang, "Microstructure and texture evolution of thin-gauge non-oriented silicon steel with high permeability produced by twin-roll strip casting," *Materials Characterization*, vol. 150, pp. 118–127, 2019.

[69] A. Koken and E. Kurt, "Finite element analysis of steel structure elements with ansys workbench," *Journal of Multidisciplinary Engineering Science and Technology (JMEST)*, vol. 8, 2021.

[70] M. Kashefi, "Stress-strain curve for 300M." email, Oct. 2024.

[71] B. Ducharne, M. Q. Le, G. Sebald, P. J. Cottinet, D. Guyomar, and Y. Hebrard, "Characterization and modeling of magnetic domain wall dynamics using reconstituted hysteresis loops from barkhausen noise," *J. Magn. Magn. Mater.*, vol. 432, pp. 231–238, Jun. 2017.

[72] T. W. Krause, L. Clapham, A. Pattantyus, and D. L. Atherton, "Investigation of strain dependent magnetic barkhausen noise in steel," *IEEE Transactions on Magnetics*, vol. 31, pp. 3376–3378, 1995.

[73] J. Gauthier, T. Krause, and D. Atherton, "Measurement of residual stress in steel using the magnetic barkhausen noise technique," *Ndt & E International*, vol. 31, no. 1, pp. 23–31, 1998.

[74] A. Srivastava, A. Awale, M. Vashista, and M. Z. K. Yusufzai, "Characterization of Ground Steel Using Nondestructive Magnetic Barkhausen Noise Technique," *Journal of Materials Engineering and Performance*, vol. 29, no. 7, pp. 4617–4625, 2020.

[75] D. Carlos and F. Grijalba, "Sensitivity of barkhausen noise in monitoring the surface integrity of sae 4340 hardened steel after turning process," *JONDE*, accepted June 21 2025.

[76] M. Kashefi, T. W. Krause, P. R. Underhill, A. Saleem, and S. P. Farrell, "Decoupling the effect of stress and microstructure on MBN response in cast Q1N steel," *Materials Science and Technology*, vol. 37, pp. 1225–1235, Oct 2021.

[77] A. Wilk and M. Michna, "The dynamic model of magnetic hysteresis," *IEEE International Conference on Industrial Technology (ICIT), Seville, IEEE*, 2015.

[78] I. Mayergoyz, "Mathematical models of hysteresis," *IEEE Trans. Magn.*, vol. 22, pp. 603–608, Sep. 1986.

[79] COMSOL. http://www.comsol.com/, accessed online 10 Februray 2025.

[80] Altair. http://altair.com/, accessed online 10 Feb. 2025.

[81] A. Regan, J. Wilson, and A. Peyton, "Extension to the jiles–atherton hysteresis model using gaussian distributed parameters for quenched and tempered engineering steels," *Sensors*, vol. 25, p. 1328, 2025.

[82] M. Toman, G. Stumberger, and D. Dolinar, "Parameter identification of the jiles-atherton hysteresis model using differential evolution," *IEEE Trans. Magn.*, vol. 44, pp. 1098–1101, 2008.

[83] Z. Gao, D. Jiles, D. Branagan, and R. McCallum, "Dependence of energy dissipation on annealing temperature of melt-spun ndfeb permanent magnet materials," *Journal of Applied Physics*, vol. 79, pp. 5510–5512, 1996.

[84] A. P. Roberts, C. R. Pike, and K. L. Verosub, "First-order reversal curve diagrams: A new tool for characterizing the magnetic properties of natural samples," *J. Geophys. Res.*, vol. 105, pp. 461–475, Dec. 2000.

Appendices

Appendix A

Models for magnetic hysteresis

This appendix provides a brief description and literature review of a few common hysteresis models used to depict and analyse the magnetic behaviour of materials. The Włodarski model [7][8] used in this research was derived from the Rayleigh relation [20] and the FORC model [64], and influenced by the Priesach [21] and the Jiles-Atherton models [22].

The Rayleigh relation [20] describes the permeability under low amplitude magnetic fields that are less than one-tenth of magnetic saturation [17]. At these levels, the hysteresis loop can be approximated by a parabolic relation between B and H field using a permeability function comprised of a constant initial permeability value and a slope: $\mu = \mu_i + \nu H$ [17]. The upper and lower branches of the hysteresis loop, B_- and B_+, respectively, can be plotted for the H field between amplitudes of $H = \pm H_m$ [17], as shown in Figure A.1, by:

$$B_\pm = (\mu_i + \nu H_m)H \pm \frac{\nu}{2}(H_m^2 - H^2) \; . \tag{A.0.1}$$

This relationship has been adapted into many hysteresis models and as a result, this low magnetization field range is also called the Rayleigh region.

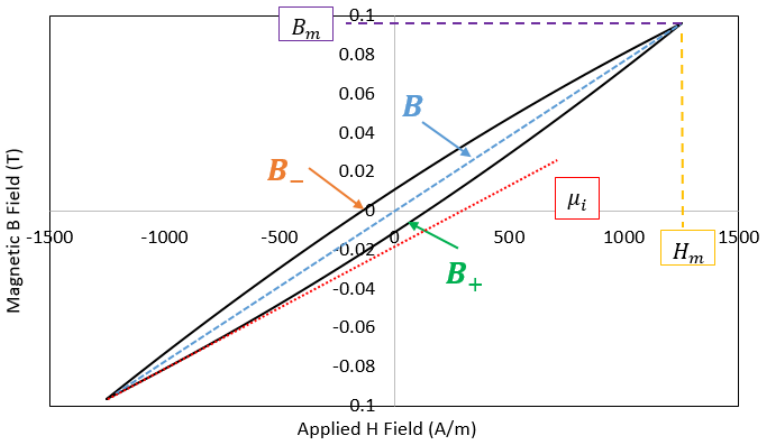

Figure A.1: Rayleigh hysteresis loop at low applied H field strength for 300M steel.

The Preisach model [21] is based on a transducer switch with an input and output relationship, which, when combined with several switches, can simulate nonlinear hysteresis. It begins with the elementary hysteresis loop, which is rectangular. Numbers α and β correspond with the up and down switching values of the input, where $\alpha > \beta$. The output values are +1 and -1, so when plotted, as shown in Figure A.2, it traces a rectangular loop from one output to the other [21]. A large number of these small loops, known as elementary hysteresis operators are summed to form a major hysteresis loop [77].

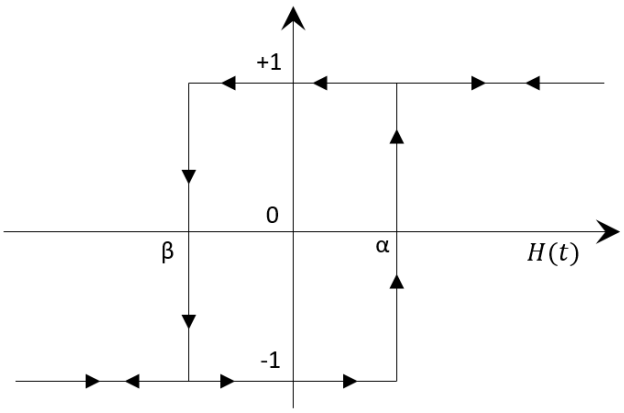

Figure A.2: A rectangular loop of an elementary hysteresis operator, which forms the basis of the Preisach model (adopted from [78]).

The Jiles-Atherton model (J-A), model [22] is based on mean field theory for DW move-

ment, which uses a differential equation solved numerically to model hysteresis [22]. This equation is composed of interrelated terms for reversible, irreversible, anhysteretic and current magnetization. In this model [22], reversible magnetization is attributed to DW bulging, irreversible magnetization is from DW pinning, anhysteretic assumes ideal magnetization without energy loss and current magnetization is the resultant magnetization of the material at the specified time. It requires five model parameters as well as theoretical variables for effective applied field and anhysteretic magnetization to plot the loops by numerical integration techniques.

The J-A model [22] has been widely adopted for electrical engineering applications with modelling software such as COMSOL [79] and Altair [80]. This being said, the model does not approximate the hysteresis of magnetically hard materials well, such as tempered martensitic steels [81], which includes 300M. Modifications to this model have been proposed using Gaussian functions to model parameters at higher H field strengths in order to better angle and shape the curve approaching saturation [82], [83]. This improves the fit for applicable steels, but increases the complexity and computational power required, and may not be practical [81].

The Stoner-Wohlfarth Model is a method to plot hysteresis based on the rotational magnetization and was first proposed by Stoner and Wohlfarth in 1947 [23]. This model is summarized well by Cullity [11] and has been found to be most applicable for magnetic powder, since it best describes uniform isolated crystals of a material. This model considers the internal demagnetization field to be composed of tiny elliptical fields based on the material's crystal anisotropy so that this magnetization can be considered constant. Figure A.3 a) shows how an elliptical shape can produce a uniform internal magnetic field, as it applies to a permanent magnet or single fully saturated ferromagnetic domain. The dimensions of the ellipse are determined by the strength of anisotropy of the material's crystal structure, which gives the dimensions of a along the "easy axis" and b along the "hard axis", as shown in Figure A.3 b). This model has found applications in magnetic recording devices [15].

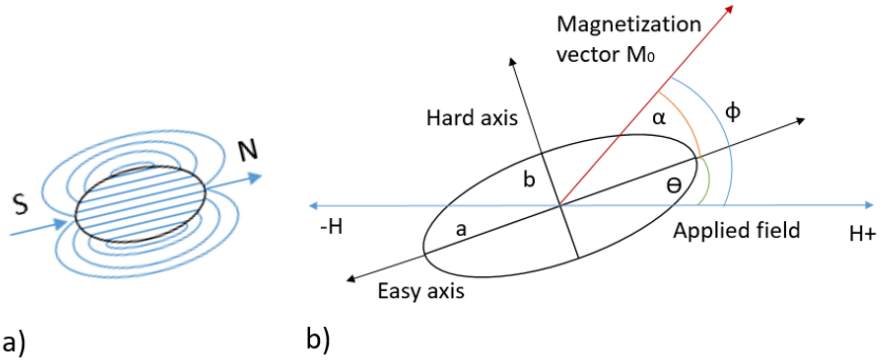

Figure A.3: a) The uniform internal magnetic field of an elliptical permanent magnet under no applied field; and b) the resulting magnetization (M_0) of the elliptical magnet under an applied H field.

The FORC method describes magnetic hysteresis by calculating the reversible and irreversible sections of the hysteresis curve [24]. Each partial curve is started at a saturation field followed by a decrease to a lower field, H_a, then reversed back up to saturation. These curves are repeated to a lower and lower H_a value and together, they are called FORC suite, which is used to determine the FORC distribution (a mixed second derivative). A FORC diagram is a contour plot of a FORC distribution. This mathematical model was first proposed by Mayergoyz [78] in 1986 in response to Priesach's scalar model of magnetic hysteresis. It has found applications in paleo-magnetic and environmental magnetic studies of natural materials affected by Earth's magnetic field [84].

Appendix B

Bending calculations

The bending apparatus has four contact points with the beam sample at A, B, C, and D with measurements between the contacts as shown below. When a load, $2 \times F$, is applied, as shown in Figure B.1 by equal point loads at B and C, the moment diagram and the beam deflection profile are obtained. Moment is force acting at a distance, so it is dispersed along the beam between the contact pins, as shown by the moment diagram in Figure B.1[53].

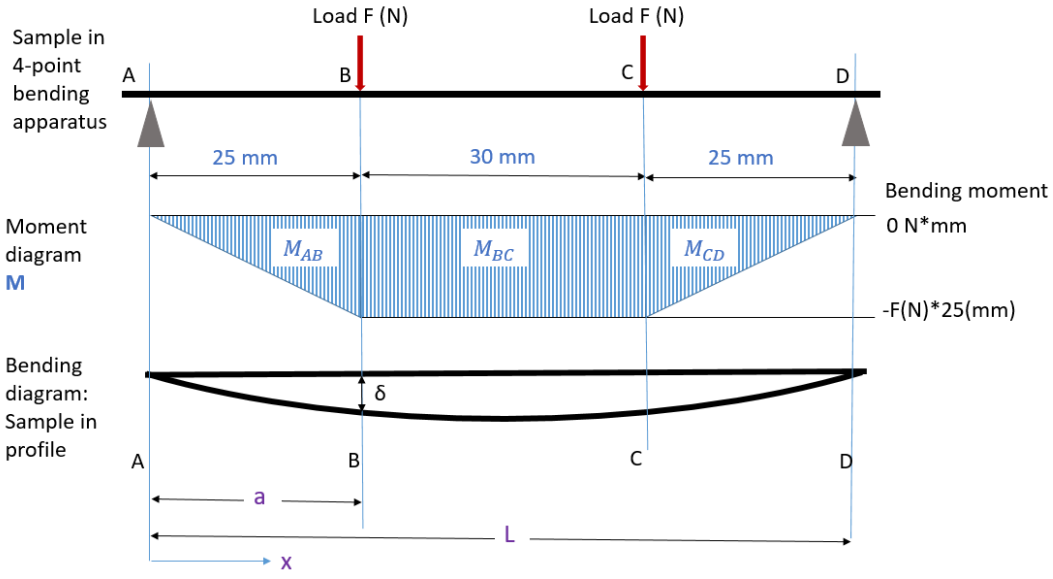

Figure B.1: Profile view of bending apparatus, moment diagram and bending diagram.

Moment is M_z, about the z axis, since the force is acting downwards in the $-y$ direction

and distance along the beam sample is in the x direction. Stress and strain are tensors, but in this bending configuration only stress and strain in the x direction; $\sigma_{xx} = \sigma$ and $\epsilon_{xx} = \epsilon$ are considered.

B.1 Elastic bending

Elastic bending is defined as a material being bent below its yield stress, σ_y. In the elastic regime, stress has a linear relationship with strain. Strain, ϵ, is the factor that a material elongates under stress, $\epsilon = \Delta l/l$, often described in terms of % of elongation. This relationship between stress and strain is also known as Hooke's law [53] :

$$\sigma = E\epsilon \ , \tag{B.1.1}$$

where E is the modulus of elasticity, or Young's modulus E, which is the slope of this region for a stress-strain plot. The limit of the elastic region is defined by the interception of an E slope off set by 0.2% strain off-set [53], as shown in Figure B.2. The ultimate stress, σ_u, is the maximum stress prior to fracture. A material is considered elastic-perfectly plastic when the yield stress is the same as the ultimate stress. Figure B.2 shows a difference between these stresses, resulting from work hardening in the plastic region, which is typical of metals.

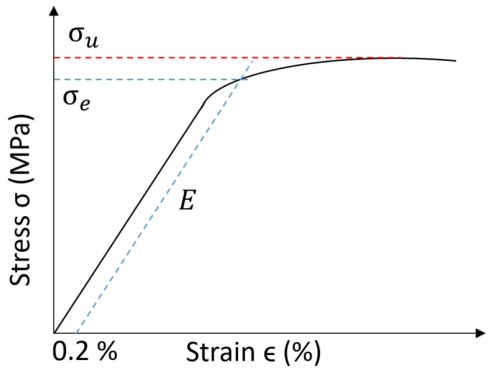

Figure B.2: A typical stress-strain plot for metal identifying the yield stress σ_e and the ultimate stress, σ_u.

Stress is force divided by area and in bending, this force is acted over a distance, so the moment must be calculated. Referring to Figure B.1, at points A and D, the moment is 0 because the beam is simply supported there. The moment equations for the three different zones of the beam; A-B, B-C, and C-D are:

$$M_{AB} = -F \cdot x \quad for\, 0 \leq x \leq B \tag{B.1.2}$$

$$M_{BC} = -F \cdot 25\,mm \quad for\, B \leq x \leq C \tag{B.1.3}$$

$$M_{CD} = F \cdot x - F \cdot 80\,mm \quad for\, C \leq x \leq D \tag{B.1.4}$$

where F is one of the two equal loads as contact points at B and C.

The second moment of inertia about the z axis, I_z, is calculated from the cross-sectional area of the beam [53] and in the case of a rectangular shape is:

$$I_z = \frac{base \cdot height^3}{12}\, mm^4\ . \tag{B.1.5}$$

Since the cross-section of the sample beam is symmetric, the height can be divided two; $height = 2c$, and reflects equal and opposite stresses above and beyond this neutral axis. The stress, σ, in the elastic region is dependent on the distance, y, away from this neutral axis of the beam and is at its maximum on the surface of the beam where $y = \pm c$:

$$\sigma = \frac{M_z \cdot y}{I_z} \quad and \quad \sigma_{max} = \frac{M_z \cdot c}{I_z}\ . \tag{B.1.6}$$

Based on the moment diagram, Figure B.1, the maximum stress occurs in the middle of the beam between B and C and is constant due to $M_z = M_{AB}$.

Deflection, δ , is the second derivative of y, vertical distance, but given the symmetry and simplicity of the four-point bending configuration, the following equation is given [54]:

$$\begin{aligned} \delta &= -\frac{Fx}{6EI}\left(3aL - 3a^2 - x\right) \quad \text{for } (0 \leq x \leq a) \\ \delta &= -\frac{Fa}{6EI}\left(3xL - 3x^2 - a^2\right) \quad \text{for } (a \leq x \leq L - a)\ , \end{aligned} \tag{B.1.7}$$

where L is the length of the beam between the bottom contact pins, a is the distance between the bottom contact pin and the nearest load pin, and x is displacement in the horizontal

direction, as shown in Figure B.1. The bending apparatus measures the deflection at the points of contact where the force F is applied. Therefore, let $x = a$ and the equation simplifies to;

$$\delta = -\frac{F}{6EI_z}\left(3La^2 - 4a^3\right) \ . \tag{B.1.8}$$

Now rearranging the above equations to solve for F and knowing the maximum moment along the middle section of the beam is $M_{max} = M_{BC} = F \cdot a$. Since this moment is linearly related to the stress according to Equation B.1.8, the relationship between deflection and stress σ can be derived:

$$F = -\delta\frac{6EI}{3La^2 - 4a^3} \ , \tag{B.1.9}$$

$$M_{\max} = F \cdot a = -\frac{6EI\delta}{3La^2 - 4a^3} \cdot a = \frac{6EI\delta}{3La - 4a^2} \ , \tag{B.1.10}$$

$$\sigma = \frac{M_{max}y}{I_z} = -\frac{6EI\delta y}{(3La - 4a^2)I_z} = -\frac{6E\delta y}{3La - 4a^2} \ , \tag{B.1.11}$$

where y is the distance of the neutral axis of the beam to the point where the stress is being considered. In this case, the stress is being measured at the surface of the beam, where it is the highest. Equation B.1.11 was used to calculate the bending increments for the elastic bending experiment (Section 5) and the elastic portion of the plastic bending experiment (Section 7) .

B.2 Bending into the plastic regime

This calculation in the plastic regime assumes the material is elastic-perfectly plastic, meaning it can not experience a stress higher than yield, $\sigma_{max} = \sigma_e = \sigma_u$. That being said, the beam as a whole can experience a moment higher than yield because, in bending, stress is a function of height, y, so the surfaces will yield before the material closer to the neutral axis. In the elastic regime, stress increases linearly with bending moment according to B.1.1 until the maximum stress reaches yield, $\sigma = \sigma_e$, and the bending moment is $M_z = M_e$, as shown in Figure B.3 a) [40]. Combining Equation B.1.5 and B.1.6, the maximum elastic stress σ_e is:

$$\sigma_e = \frac{M_e \cdot c}{\frac{1}{12} \cdot base \cdot (2c)^3} = \frac{M_e \cdot c}{I_z} \ , \tag{B.2.1}$$

or

$$M_e = \frac{I_z \cdot \sigma_e}{c} \ , \tag{B.2.2}$$

where I_z is the second moment of inertia about the z-axis, which is defined in Equation B.1.5 for a rectangular cross-sectional area. If the moment increases beyond yield, $M_z > M_e$, then the stress is partial plastic and elastic, as shown in Figure B.3 b).

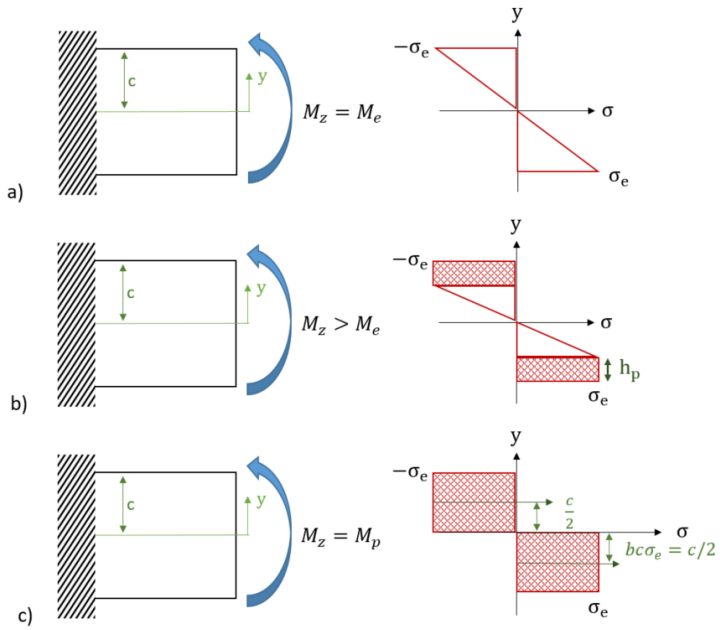

Figure B.3: Beam bending stress diagram for a) maximum elastic bending, b) partial plastic and elastic bending, and c) fully plastic bending.

Since the material does not experience stress beyond yield in the elastic-perfectly plastic approximation, this increasing moment produces a plastic zone that increases linearly with the height of the plastic zone, h_p. Strain gauge measurements from the surface of the beam, where the stress and strain are at a maximum, $\epsilon = \epsilon_{max}$ and $\sigma = \sigma_e$, can be used to

determine the height of the plastic zone [40]:

$$\begin{aligned} \epsilon_{max} &= \frac{\sigma_e c}{E(c-h_p)} \ , \\ h_p &= c - \frac{\sigma_e c}{E(\epsilon_{max})} \ , \end{aligned} \tag{B.2.3}$$

Equation B.2.3 shows that h_p and ϵ_{max} are proportional in this plastic regime, since all other variables are constant. This relationship was used during the experiment, to extrapolate the height of the plastic zone beyond the bending deflection when the strain gauge broke, to continue residual stress calculations.

The moment M_z, is determined by integrating over the area produced by this stress distribution for the cross-section of the beam; $dA = base \cdot dy$. This moment integration becomes [40]:

$$\begin{aligned} M_z &= -2\int_0^c y \cdot \sigma_x dA \ , \\ M_z &= -2\left[\int_0^c \left(-\frac{\sigma_e}{c-h_p}y\right) y \cdot base \cdot y + \int_{c-h_p}^c \sigma_e \cdot y \cdot base \cdot dy\right] \ , \\ M_z &= \frac{2}{3} base \cdot c^2 \cdot \sigma_e \left[1 + \frac{h_p}{c} - \frac{1}{2}\left(\frac{h_p}{c}\right)^2\right] \ , \\ M_z &= \frac{I_z \sigma_e}{c}\left[1 + \frac{h_p}{c} - \frac{1}{2}\left(\frac{h_p}{c}\right)^2\right] \ , \end{aligned} \tag{B.2.4}$$

since the second moment of inertia for a rectangular beam is $I_z = 2/3 \ base \cdot c^3$, obtained from Equation B.1.5 when the height is $2c$.

According to Equation B.2.4, at $h_p = 0$, there is no plastic stress and $M_z = M_e$ as shown in Equation B.2.2. If $h_p = c$, then the beam is in fully plastic stress and $M_z = M_p$, as shown in Figure B.3 c).

The bending moment, M_z and the height of the plastic zone are closely linked and are key to calculating the residual stress and strain remaining in the beam once the active load is removed.

B.3 Residual stress and strain

Residual stress, σ_{res}, is the stress that remains after permanent deformation has occurred and the bending load has been removed. On a stress-strain plot, unloading decreases the load along a path parallel to the Young's modulus, E, which does not return to zero strain. For the stress-strain plot of a monotonic tensile test, the unloading follows this parallel path back to the x-axis producing a residual strain without residual stress. For a bending sample, the bowed shape locks in residual stress so that the residual strain produces an internal stress as shown in Figure B.4, which depends on y-coordinate through the thickness of the sample, as previously shown in Figure B.3 a).

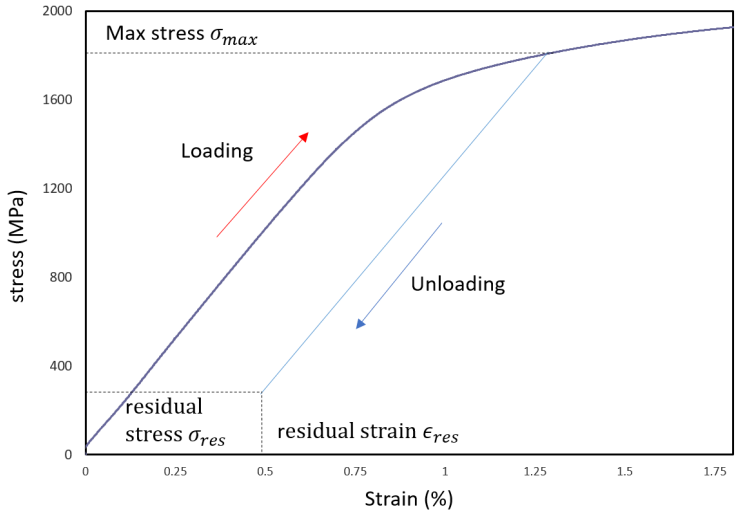

Figure B.4: Stress-strain plot for 300M steel showing the residual strain and stress when loaded to a stress above the yield point then unloaded.

To calculate residual stress and strain, consider profile view of the partial plastic and elastic stress distribution diagram in Figure B.3 b). The active bending moment is then unloaded linearly. These two steps are superposed to produce the resulting residual stress distribution, as shown Figure B.5.

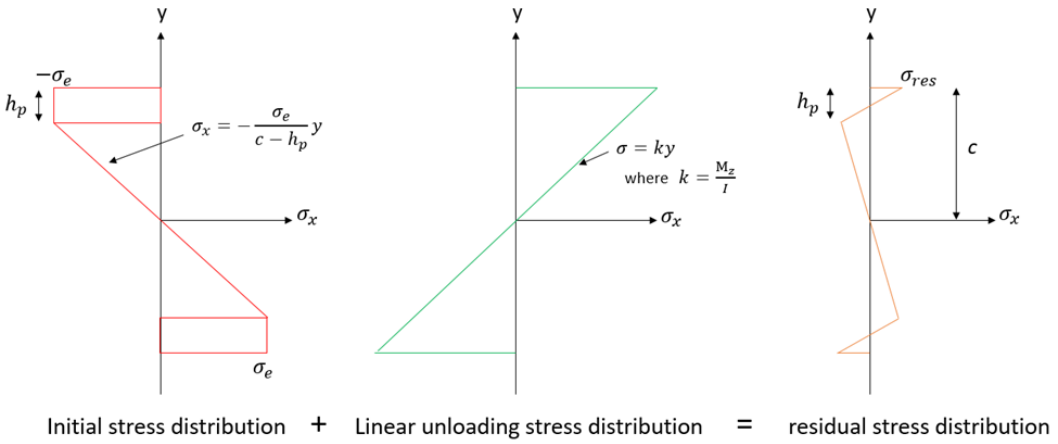

Figure B.5: Residual stress distribution as a result of initial stress and linear unloading (adopted from [40]).

This residual strain, and its associated residual stress, are directly related to height of the plastic zone, h_p, and active bending moment M_z [40]:

$$\sigma_{res} = \begin{cases} \left(\frac{M_e}{I_z} - \frac{\sigma_e}{c-h_p}\right)y & 0 \leq y \leq c - h_p \\ \frac{M_z}{I_z}y - \sigma_e & c - h_p \leq y \leq c \ , \end{cases} \tag{B.3.1}$$

and

$$\epsilon_{res} = \frac{1}{E}\left(\frac{M_z}{I_z} - \frac{\sigma_e}{c-h_p}\right)y \ . \tag{B.3.2}$$

B.4 Bending deflection

The bending deflection is the displacement of the center chord, in the vertical or y direction. In the four-point bending configuration, the deflection, δ, is given by Equation B.1.7, which produces a parabolic function between the center load points $a \leq x \leq L - a$ of Figure B.1. This parabolic shape is known as the radius of curvature, R, which, for a rectangular cross-sectional beam is given by [53];

$$\frac{1}{R} = \frac{d^2y_0/dx^2}{[1 + (dy_0/dx)^2]^{2/3}} = \frac{M_z}{EI_z} \ , \tag{B.4.1}$$

where $y_0 = \delta$ is the deflection of the centroid axis. For small slopes, the small angle approximation of the radius of curvature equation is often simplified to the second derivative;

$1/R = d^2y_0/dx^2$. The radius of curvature is directly related to strain, since curving requires a change in length. Equation B.4.1 reduces to;

$$\begin{gathered} \frac{1}{R} = \frac{M_z}{EI_z} = -\frac{\epsilon_x}{y} \\ \text{at } y = c \quad \epsilon = -\frac{c}{R} \, , \end{gathered} \tag{B.4.2}$$

where ϵ_x is strain at any position along the beam, y indicates the height through the thickness of the beam so that $y = c$ is on the surface, and ϵ is the strain at the middle surface of the beam.

When the sample is subjected to elastic bending, the deflection along the length, δ_x, can be calculated by Equation B.1.7. Plotting the resulting bent profile on an x-y graph will give a parabolic trend in the form of $y = ax^2 + bx + c$, which can then be used in Equation B.4.1 to determine the radius of curvature. Under plastic bending, the deflection profile cannot be assumed to follow Equation B.1.7, but if it can be measured and plotted, Equation B.4.1 still applies. This was the method used to calculate residual stress in the permanently bent samples, as shown in Appendix I. The radius of curvature correlates to strain, which can then be used to calculate stress by Hooke's law, Equation B.1.1.

Appendix C

Conductivity measurements

The samples' conductivity, σ values were measured by way of Ohm's law, Equation 2.1.8, using a four-point contact experimental set up. The samples' cross-sectional area was measured, a current was sent through its length and two contacts were used to measured the voltage drop between them. This experimental set up is shown in Figure C.1. The measurements and resulting conductivity values for the three experimental sample materials are summarized in Table C.1.

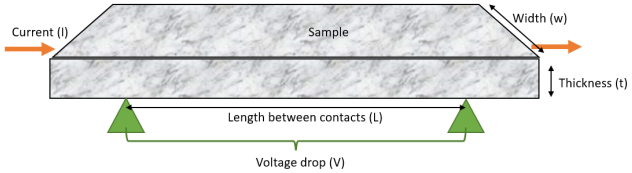

Figure C.1: Conductivity measurement of a sample by 4-point contact; two contacts for applying a current and two for measuring the voltage drop.

Table C.1: Summary of measurements taken for sample conductivity values

Material	**300M**	**4340**	**HY80**	**Units**
Width	0.74	0.73	0.55	cm
Thickness	0.20	0.20	0.28	cm
Length	6.55	9.05	9.60	cm
Voltage	0.237	0.276	0.170	mV
Current	105	100	100	mA
Resistance	2.26×10^{-3}	2.76×10^{-3}	1.70×10^{-3}	Ω
Conductivity σ	1.96×10^{6}	2.25×10^{6}	3.67×10^{6}	S/m

Appendix D

Włodarski model parameters

This appendix lists all the Włodarski Model [8], [7] parameters derived in this study from experimental data. The method for this derivation is covered in Section 4.1.1 and the five parameters are:

- M_a is the reversible magnetization parameter;
- M_b is the irreversible magnetization parameter;
- a is the parameter governing the reversal rate from saturation;
- c is the coercivity parameter; and
- b is the parameter controlling the rate of approach to saturation.

This model was used in the hysteresis plot experiment, Section 4, and the plastic bending experiment, Section 7.

D.1 From the hysteresis plot experiment

This experiment plotted the hysteresis curves for three sample materials; 300M, AISI 4340 and HY80. The initially derived parameters from the initial magnetization curve are listed in Table D.1, which was used to compare the hysteresis models between the three sample materials and explore the applicability of modelling minor hysteresis loops for 300M. The major hysteresis loops for the samples were also analyzed with adjusted parameters to finding the best fit to the major hysteresis loops for each material is shown in Table D.2.

Table D.1: Włodarski Model parameter from initial magnetization curves for 300M, AISI 4340, and HY80 samples.

Parameter	**300M**	**AISI 4340**	HY80
M_a (A/m)	1.10×10^6	6.45×10^5	6.31×10^5
a	5.32×10^3	6.62×10^3	8.84×10^3
M_b (A/m)	8.00×10^5	1.09×10^6	1.32×10^6
b	3.31×10^2	1.27×10^2	1.08×10^2
c	1.96×10^3	8.83×10^3	4.66×10^3

Table D.2: Włodarski Model parameter adjusted to best fit the major BH curves for 300M, AISI 4340, and HY80 samples.

Parameter	**300M**	**AISI 4340**	**HY80**
M_a (A/m)	4.20×10^5	1.61×10^6	8.51×10^5
a	3.00×10^3	3.09×10^5	8.82×10^3
M_b (A/m)	9.00×10^5	1.23×10^6	1.29×10^6
b	2.15×10^2	1.16×10^2	8.82×10^1
c	2.14×10^3	9.33×10^3	6.05×10^2

D.2 From the plastic bending experiment

This experiment plotted the hysteresis curve for three 300M samples before and after plastic deformation. The samples were measured three times in the BH curve experimental set up; once before bending and twice after plastic deformation. The bent samples had two different orientations; magnetized from the concave side, bent up, and magnetized from the convex side, bent down, as shown in Figure D.1. Table D.3 shows the Włodarski Model [7, 8], parameters for the three samples in the measured configurations.

Figure D.1: Configuration of 300M samples in the BH curve experiment for the plastic bending experiment.

Table D.4 shows the model parameters used to compare the average unbent and bent sample hysteresis loops conducted for the analysis of Section 7.3.3.1.

Table D.3: Magnetic characteristics from initial magnetization curves for samples before and after bending.

Parameters	Sample A	Sample B	Sample C
Unbent			
M_a (A/m)	5.56×10^6	6.22×10^6	7.32×10^6
a	3.73×10^4	3.58×10^4	3.66×10^4
M_b (A/m)	8.25×10^5	7.75×10^5	7.28×10^5
b	4.40×10^2	4.13×10^2	4.16×10^2
c	1.97×10^3	2.12×10^3	2.05×10^3
Bent: Magnetized side up			
M_a (A/m)	6.50×10^6	5.85×10^6	7.98×10^6
a	4.06×10^4	4.82×10^4	3.82×10^4
M_b (A/m)	4.39×10^5	5.87×10^5	4.46×10^5
b	2.63×10^2	4.25×10^2	2.26×10^2
c	1.94×10^3	2.01×10^3	1.91×10^3
Bent: Magnetized side down			
M_a (A/m)	6.28×10^6	7.23×10^6	6.06×10^6
a	4.57×10^4	4.64×10^4	4.59×10^4
M_b (A/m)	4.33×10^5	4.82×10^5	5.94×10^5
b	3.09×10^2	2.98×10^2	4.17×10^2
c	2.02×10^3	1.94×10^3	2.11×10^3

Table D.4: Włodarski Model parameter for the average of 300M Samples A, B and C: unbent, bent, bent down and bent up sample hysteresis loops.

Parameter	Average unbent (sample C)	Average bent sample	Max bent (sample C up)	Min bent (sample A down)
M_a (A/m)	7.32×10^6	6.65×10^6	7.98×10^6	6.28×10^6
a	3.66×10^4	4.42×10^4	3.82×10^4	4.57×10^4
M_b (A/m)	7.28×10^5	4.97×10^5	4.46×10^5	4.33×10^5
b	4.16×10^2	3.23×10^2	2.26×10^2	3.09×10^2
c	2.05×10^3	1.99×10^3	1.91×10^3	2.02×10^3

Appendix E

Experimental uncertainty data

This section discusses the experimental uncertainty measured for the stress due to deflection, the zeroing test, and the variation of MBN measurements for the same sample, the repeatability test. The tables contain the experimental data gathered for these two tests.

E.1 Initial set up; zeroing test

This section shows the data collected to capture the variation in deflection for the initial set up of the sample in the bending apparatus. Two samples of each material were repeatedly placed in the apparatus, which was set up for zero deflection. The samples used in this test were of the same batch as described in Section 3.2 and labelled Samples S5 and S7 for 300M, Samples S1 and S2 for AISI 4340 and Samples S3 and S4 for HY80 steels. Five of these trials were conducted per sample per side, as denoted by calling the sample flipped. The deflection gauge was not readjusted between trials so that the variation could be calculated as the standard deviation for each set of five trials, as recorded in the Table E.2.

The largest standard deviation measured for each sample orientation was used to calculate the uncertainty for the sample initial set up, which carries through for all the bending deflection stress calculations. Table E.1 summarized these results.

Table E.1: Summary of stress uncertainty from zeroing test for sample materials.

Sample (thickness)	Largest standard deviation (mm)	Bending stress (MPa)	Rounded stress uncertainty (MPa)
300M (2.18 mm)	0.041	15.7	$\pm$15
AISI 4340 (2.02 mm)	0.045	15.8	$\pm$15
HY80 (2.8 mm)	0.051	23.5	$\pm$25

Table E.2: Deflection variation for 300M, AISI 4340 and HY80 initial sample bending apparatus set-up (units 10^{-2} mm).

300M sample & orientation	**Trial 1**	**Trial 2**	**Trial 3**	**Trial 4**	**Trial 5**	**Standard Deviation**
S5	-2	7	-3	6	1	$\pm$4.1
S5 flipped	40	37	38	43	39	$\pm$2.3
S7	4	10	2	8	3	$\pm$3.1
S7 flipped	24	17	20	18	23	$\pm$2.7
4340 sample & orientation	**Trial 1**	**Trial 2**	**Trial 3**	**Trial 4**	**Trial 5**	**Standard Deviation**
S1	2	4	1	-1	-4	$\pm$2.7
S1 flipped	2	4	6	8	9	$\pm$2.6
S2	6	5	-2	-6	2	$\pm$4.5
S2 flipped	9	7	1	8	4	$\pm$2.9
HY80 sample & orientation	**Trial 1**	**Trial 2**	**Trial 3**	**Trial 4**	**Trial 5**	**Standard Deviation**
S3	13	9	7	12	13	$\pm$2.4
S3 flipped	-3	6	4	-1	1	$\pm$3.3
S4	-4	-3	9	-5	-1	$\pm$5.1
S4 flipped	9	1	11	4	-2	$\pm$4.8

E.2 MBN energy repeatability test

MBN energy measurements are very repeatable when taken one after the other, with no change to the sample or probe position. Although, it is very sensitive to surface conditions and microstructure, so variation in measurements are expected at different locations along the surface of the sample. These repeatability tests capture that variation, in terms of standard deviation of the measurements, to provide the bases for the experimental measurements. This variation is defined as the standard deviation of 20 total measurements taken with both top and bottom probes of two different samples of each material. These tests were

conducted at both 30 Hz and 50 Hz excitation, as shown in Tables E.3 and E.4, respectively. The elastic bending experiment (Section 5) used the uncertainty values for 0.8 T flux and 30 Hz and the plastic bending experiment (Section 7) used the values for the 300M sample only, at 0.4 T and 0.8 T flux and 50 Hz.

The excitation frequency and flux level also affects the repeatability of MBN energy measurements. The excitation frequency affects the time it takes for a magnetization cycle, which changes the time integral for MBN energy calculation 2.5.1. This allows lower excitation frequencies to give higher MBN energy measurements, with higher variation, even though the MBN signal peak amplitudes are lower than with higher frequencies. For both excitation frequences, low flux values produce less MBN energy so there is a higher level of uncertainty for 0.1 T and 0.2 T. Although, 0.4 T and 0.5 T flux have been found to produce a more responsive level of MBN energy than 0.8 T, for some materials [44].

These repeatability tests were taken with the sample under zero loading, so it can't be assumed that the uncertainty would be constant as the bending load increases. For that reason, these uncertainty values were added to the standard deviation values obtained by multiple measurements taken during the experiments.

Table E.3: Measurements of Average Magnetic Barkhausen noise energy (MBNe) and variation for 300M, AISI 4340, and HY80 samples at 30 Hz excitation.

300M			
Flux (T)	Ave. MBNe (mV^2s)	Standard deviation (mV^2s)	Difference %
0.1	4.5	3.8	85%
0.2	30.0	21.6	72%
0.3	130.0	45.4	35%
0.4	332.9	63.8	19%
0.5	542.0	84.2	16%
0.6	721.1	104.5	14%
0.7	864.6	116.7	13%
0.8	979.8	121.4	12%
AISI 4340			
Flux (T)	Ave. MBNe (mV^2s)	Standard deviation (mV^2s)	Difference %
0.1	37.7	17.2	46%
0.2	396.7	48.3	12%
0.3	858.1	57.2	7%
0.4	1275.0	53.7	4%
0.5	1638.7	50.4	3%
0.6	1946.3	83.4	4%
0.7	2232.1	134.0	6%
0.8	2453.7	163.1	7%
HY80			
Flux (T)	Ave. MBNe (mV^2s)	Standard deviation (mV^2s)	Difference %
0.1	35.2	27.4	78%
0.2	335.5	179.6	54%
0.3	810.3	273.1	34%
0.4	1318.8	288.9	22%
0.5	1800.5	256.6	14%
0.6	2266.5	203.0	9%
0.7	2671.8	151.0	6%
0.8	3004.8	114.1	4%

Table E.4: Measurements of Average Magnetic Barkhausen noise energy (MBNe) and variation for 300M, AISI 4340, and HY80 samples at 50 Hz excitation.

300M			
Flux (T)	Ave. MBNe (mV^2s)	Standard deviation (mV^2s)	Difference %
0.1	4.3	3.3	76%
0.2	33.2	21.5	65%
0.3	155.3	44.0	28%
0.4	360.4	58.5	16%
0.5	545.9	78.4	14%
0.6	686.0	89.4	13%
0.7	788.5	94.7	12%
0.8	867.2	101.1	12%
AISI 4340			
Flux (T)	Ave. MBNe (mV^2s)	Standard deviation (mV^2s)	Difference %
0.1	47.5	17.8	38%
0.2	448.7	42.5	9%
0.3	895.7	49.8	6%
0.4	1268.9	44.5	4%
0.5	1575.7	54.3	3%
0.6	1803.5	88.0	5%
0.7	2005.9	97.0	5%
0.8	2177.1	120.3	6%
HY80			
Flux (T)	Ave. MBNe (mV^2s)	Standard deviation (mV^2s)	Difference %
0.1	46.5	31.4	68%
0.2	449.2	176.6	39%
0.3	1002.7	212.8	21%
0.4	1517.8	202.4	13%
0.5	1982.1	177.6	9%
0.6	2378.1	130.6	5%
0.7	2674.2	99.2	4%
0.8	2868.2	80.8	3%

Appendix F

MBN response with frequency

The elastic bending and plastic bending experiments were conducted at the different excitation frequencies of 30 Hz and 50 Hz. Frequency affects Barkhausen noise because it changes in time interval over which the MBN events or signals are picked up, as well as the magnetizing rate, depth of field penetration and induced eddy currents. Lower frequency allows more time over which the events are integrated but comes with a lower field strength to induce events.

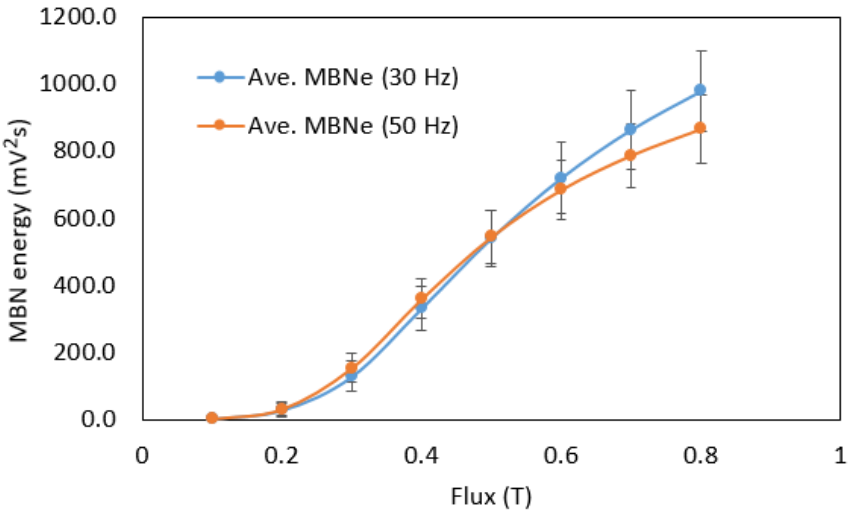

Figure F.1: Flux sweep results from repeatability tests on 300M Sample S8 at 30 Hz and 50 Hz.

By comparing MBN response at 30 Hz with the response at 50 Hz, the trend shows the lower frequency produces more MBN energy than the higher frequency, because of the

longer time interval. Figure F.1 shows the average flux sweeps for both 30 Hz and 50 Hz, from the measurements collected for the Repeatability test discussed in Section 5.2.4.2 and 7.2.2.1. The low field strength from 0.1 to 0.5 T masks the differences between the frequencies.

Comparing the MBN envelopes formed by the magnitude, or RMS value for the MBN signals, for the two frequencies, provides a different perspective. Figure F.2 shows the envelopes for Sample A at different flux levels for 30 Hz and 50 Hz. The higher frequency MBN envelopes are bigger, but when they are integrated over the 50 Hz time interval, the resulting MBN energy is more comparable to the MBN energy of the 30 Hz envelope, as is shown in Figure F.1. The higher frequency increases the speed and abruptness of the H field applied to the sample, which induces a higher signal amplitude and a steeper envelope shape. The 30 Hz envelope for 800 mT flux has more noise between the cycles than the higher frequency, as shown by the peaks between 0.8 and 0.5 T. The envelope peak locations between the two sets of envelopes are similarly situated for each flux level, with a slight left or forward leaning bias for the 50 Hz envelopes.

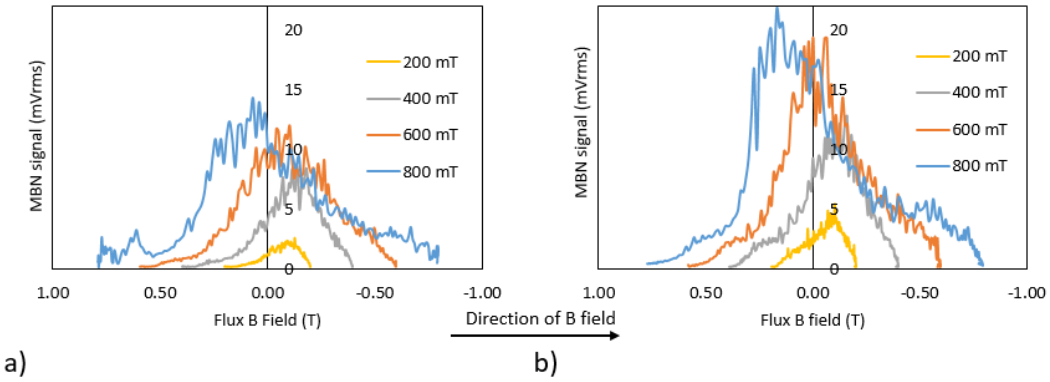

Figure F.2: MBN envelopes from Sample A, no stress, bottom probe results at a) 30 Hz and b) 50 Hz excitation.

Future research may look into a way to normalize MBN response for different frequencies with the goal to reduce the number of parameters affecting the results. Alternatively, experiments could be conducted to determine the best combination of flux and frequency for MBN stress detection in this 300M material. Results from this research suggest that

0.4 T flux at 50 Hz excitation is more sensitive to stress and therefore, produces a bigger variation in MBN energy response to stress than 0.8 T, as shown by the flux sweep plot Figure 7.8 . Although, this sensitivity also results in more variability between measurements. 0.8 T approaches saturation of the magnetic circuit, so it will exhibit overall less variation in MBN response due to noise, producing more repeatable measurements.

Appendix G

ANSYS model for sample bending

This section provides information on the Finite Element Method (FEM) model of the 300M sample in four-point bending apparatus. This ANSYS model and simulation work was done by Fan Liu, on behalf of the author. The model was used for analysis of the samples in plastic deformation to determine residual stress for comparison with the MBN results for stress estimation. The sample configuration and bending apparatus contact pins that were modelled are shown in Figure G.1.

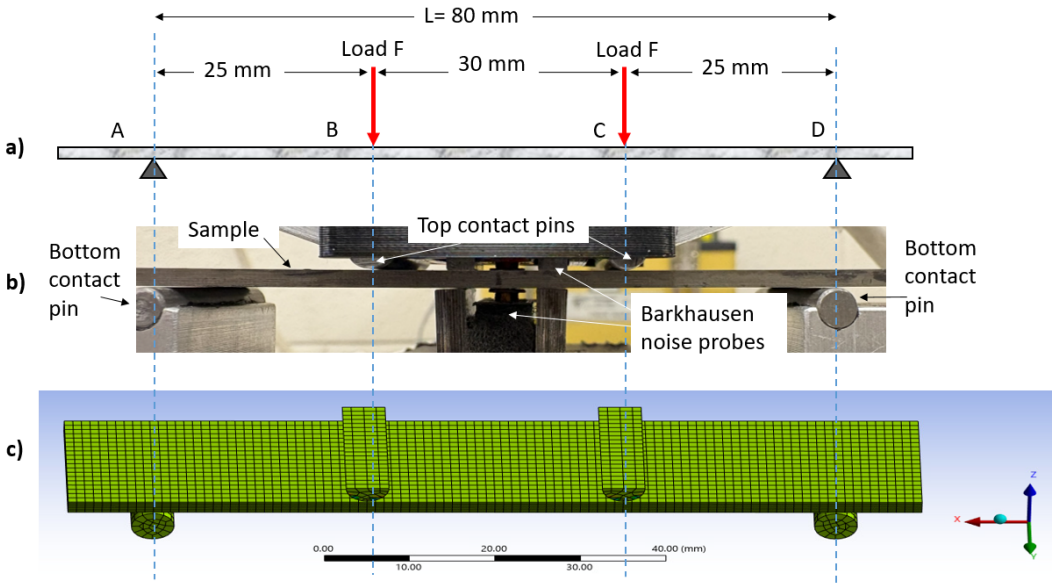

Figure G.1: Diagram of a) sample with dimensions of four-pint bending contacts, b) image of sample in experimental set up, and c) ANSYS model of sample and contacts.

The model analysis was conducted with ANSYS, Version 2024 R2. The purpose of the model was to determine the residual stress between the top contact pins on the upper surface of the sample, following plastic bending. Bending was measured by the downwards displacement of the center contacts. The yield strength for this material, 1500 MPa, was expected to be reached around 4.5 mm displacement so the model was run for ten stand-alone displacement simulations from 4.5 mm to 9.0 mm, at 0.5 mm increments. Residual stress was calculated as the remaining stress when the sample was off loaded, at 0 mm deflection.

The material properties for the 300M steel sample [57, 58] and the sample dimensions are summarized in Table G.1. The tangent modulus was calculated from the stress-strain data conducted by M. Kashefi [70] as a linear approximation of the plastic region of the stress-strain plot. The material properties were entered into the Isotropic Elasticity and Bilinear Isotropic Hardening sections of the Engineering data for the simulation. The four contact pins were selected as regular structural steel [69] from the ANSYS database, with properties as shown in Table G.1. The Barkhausen noise probes shown in Figure G.1 were omitted from the model as they shouldn't affect the bending of the sample.

Table G.1: Mechanical properties of the sample and contact pins.

Characteristic	300M Sample	Structural steel contact pins
Dimensions	$100\times19\times2.0$ mm^3	2.5 mm radius, 19 mm length
Yield strength	1500 MPa	250 MPa
Ultimate strength	2000 MPa	460 MPa
Poisson's ratio	0.28	0.3
Elastic modulus	205 GPa	200 GPa
Tangent modulus	13.6 GPa	N/A

G.1 Meshing and model configuration

The Model consisted of the rectangular sample, $100\times19\times2.0$ mm^3, and four contact pins represented as half-cylinders with 2.5 mm radius and a length to match the sample's width of 19 mm. The top two contact pins were cut length-wise so as only to model the bottom

half that made contact with the sample, as shown in Figure G.1 c). The physical sample differed slightly from these dimensions by being longer and thicker; $119 \times 19 \times 2.18$ mm^3. This difference in thickness translates to a 130 MPa lower stress for 4.18 mm displacement, which is an 8% reduction to the expected 1600 MPa for the experimental sample. This difference was assessed as negligible in comparison with the stress underestimation expected from the linear approximation of the plastic region of the stress-strain curve. The longer length did not affect the stress analysis in the center of the sample.

The sweep method was used to mesh with a final body size of 1 mm across the top and bottom surfaces of the sample. This element size was confirmed to be appropriate for this analysis by a convergence curve based on the resulting Von-Mises stress, as shown in Figure G.2 a). The element mesh size was increased from 1 mm to 10 mm and gave a tight stress range of 702-708 MPa, which indicates that the solution is converging. Meshes finer than 1 mm were not attempted due to the increased computational load and satisfactory convergence results. The sample model was meshed with 7 elements through the thickness.

The sample and contact pins were modelled in halves, split in the center and mirrored to create the full model. The center face, in the Y-Z plane, was restrained from moving in the X and Y directions so that it could only translate in the vertical Z direction when deflected. Rotation about the X axis was constrained by the physical interaction of the contact pins. A convergence study was conducted for the stiffness factor between these contact pins and the sample, and the resulting Von-Mises stress, as shown in Figure G.2 b). An increase in stiffness factor from 1 to 10 showed minimal variation in stress, which indicates that the simulation is able to converge with the current meshing configuration.

The interface between the contact pins and the sample were selected as contact interaction with no coefficient of friction, since the stresses act normal to the surface. To ensure that there was no stress on the sample at the beginning of the simulation, all components were separated in the Z direction. The initial contact information, generated by ANSYS, indicated that the gap distance ranged between 0.25 and 0.27 mm. Therefore, the first set in the simulation sequence was to move the components together by more than the gap dis-

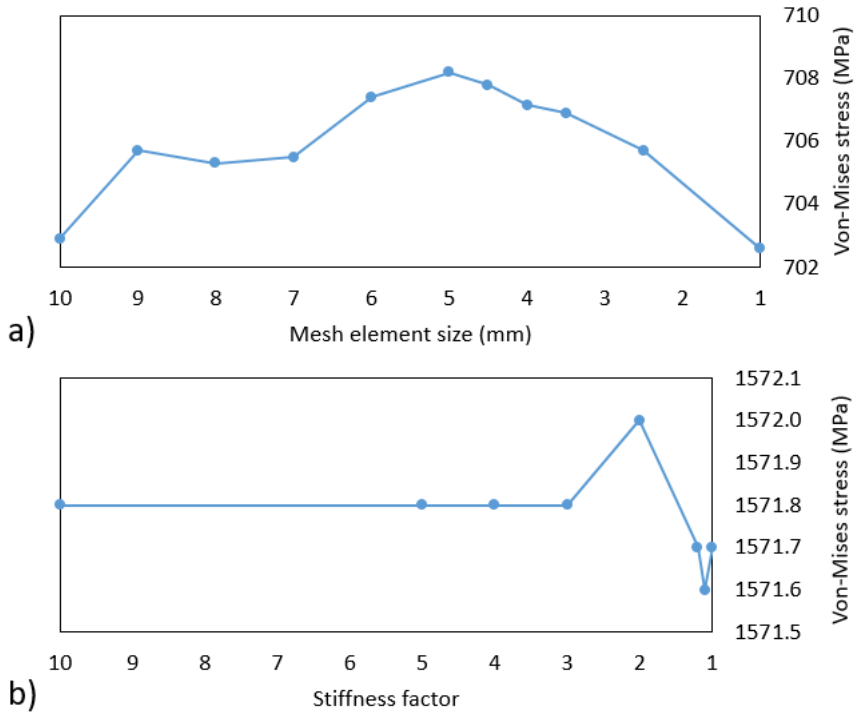

Figure G.2: Convergence studies a) mesh sizing for sweep method and b) stiffness factor for top contact pins.

tance, to ensure contact was established before bending load was applied. For this, a gap closing distance of 0.31 mm was selected.

G.2 Simulation sequence

The model was run for each 0.5 mm deflection increment from 4.5 mm to 9.0 mm, for a total of 10 simulations. The model began with the sample and contact pins separated by a gap to ensure no initial stresses were present. The first two steps of the simulation brought the top loading contact pins into contact with the sample, then pushed it down into the bottom contact pins. The sample was then loaded by moving the loading pins down to the designated deflection increment, then unloaded by returning the pins to the starting position. Details for this sequence are in Table G.2. The data collected for each simulation was the loaded and residual stress and strain on the center top and bottom surfaces of the sample.

This was the location of interest where the Barkhausen noise probes took measurements of the sample's magnetic response to stress.

Table G.2: Simulation sequence for ANSYS model, Sample and contact pins.

Steps	Time (s)	Sample Status	Loading Pins Status
1	0	No deflection.	Loading pins Z=0 mm, no contact.
1	1	No deflection. In contact with loading pins.	Loading pins Z=-0.31 mm, made contact with sample.
2	2	No deflection, sample Z=-0.31 mm, made contact with fixed support pins.	Loading pins Z=-0.62 mm, all model components in contact but no loading.
3	3	Under loaded bending.	Loading pins Z=-(0.62+deflection input) mm.
4	4	Unloaded, recovered to Z=0 mm	Unloaded position, pins Z=0 mm, no contact

Each bending sequence was run independently, meaning that the sample was returned to an initial zero stress state for Step 1. This differed from the experimental procedures, since each sample was cycled through all the bending deflections. An attempt was made to increase the simulation sequence for multiple plastic bending increments, but the software couldn't handle the computational load and failed to solve. This stand-alone approach should provide a good approximation to the experimental set up, since cyclical fatigue and work hardening were not being considered and 300M steel was assumed to be an elastic-perfectly plastic material, as approximated by the bilinear isotropic stress-strain plot. This assumption implied that the stress results are not influenced by previous loaded states.

Appendix H

Stress calculations for 300M samples

This section discusses how the stress values were established for the plastic bending experiment. Stress or loading on the sample in the four-point bending apparatus wasn't measured directly, so it is important to state how it was derived from bending deflection, strain measurements and calculations.

The method selected for this research was to take the average stress between initial calculations and those derived from strain measurements. The initial calculations were based on elastic bending and deflection, as covered in Appendix B. Near the yield point and in the plastic zone, this was changed to make estimates based on the stress-strain plot. Stress derived from strain measurements were calculated with Hooke's law, Equation 3.1.1, in the elastic range. After yield, around 4.31 mm deflection or 1650 MPa, stress was calculated based on the height of the plastic zone, h_p. When the strain gauge broke, at 7 mm deflection, these calculations were based on the extrapolation of plastic zone height in relation to bending deflection.

The average between the initial calculations and the strain based calculations was used to assess MBN response to stress. The uncertainty of these stress values were based on the standard deviation between the sets of stress calculations, plus the uncertainty due to the zeroing test described in Appendix E, which was $\pm$15 MPa for the 300M samples, as shown in Section 5.2.4. Table H.1 shows these stress calculations and uncertainty values for bending deflection at each increment measured during the plastic bending experiment.

Table H.1: Calculated stress used to determine the average stress and uncertainty as plotted in Section 7.3.1.

Deflection	**Stress (MPa)**		**Plotted stress (MPa)**		
	Based on initial calculations	Based on strain measurements	Average stress (MPa)	**Deviation**	Total Uncertainty
0	0	19	9	13	28
0.26	100	82	91	13	28
0.52	200	152	176	13	28
0.78	300	297	298	2	17
1.04	400	396	398	3	19
1.31	500	456	478	31	46
1.57	600	529	564	50	65
1.83	700	626	663	52	67
2.09	800	793	797	3	20
2.35	900	872	886	20	35
2.61	1000	932	966	48	63
2.87	1100	1003	1051	69	84
3.13	1200	1147	1174	37	52
3.39	1300	1277	1289	16	31
3.65	1400	1348	1374	36	51
3.79	1450	1383	1416	47	66
3.92	1500	1411	1465	63	78
4.05	1550	1443	1484	70	90
4.18	1600	1483	1541	83	98
Yield and Plastic bending zone					
4.31	1650	1536	1593	81	96
4.5	1700	1650	1675	36	51
5	1750	1705	1753	4	19
5.5	1800	1819	1810	13	28
6	1850	1908	1903	3	18
6.5	1900	1946	1923	33	48
7	1950	2006	1978	40	55
Plastic zone beyond strain gauge measurements					
7.5	-	2060	2060	-	52
8	-	2105	2105	-	52
8.22	-	2123	2123	-	52
8.5	-	2144	2144	-	52
9	-	2177	2177	-	52

Appendix I

Sample profile measurements

The convex sides of the bent Samples A, B, C and G were measured for permanent deflection by way of a milling machine, as described in Section 3.1.4. This change in height measurement gave the curved profile for each sample as shown in Figure I.1. The profile measurements have been taken along the sample's surface, setting $y = 0$ at $x = 0$ as the reference to the left side outer contact pin. The figure only shows the profile for the center section of the samples, between the two inside loading pins of the four-point bending apparatus, where the MBN probes are located. The x-axis of the figure indicates the distance along the sample starting at the left side bottom contact pins, which are 80 mm apart, so the center is at $x = 40$ mm.

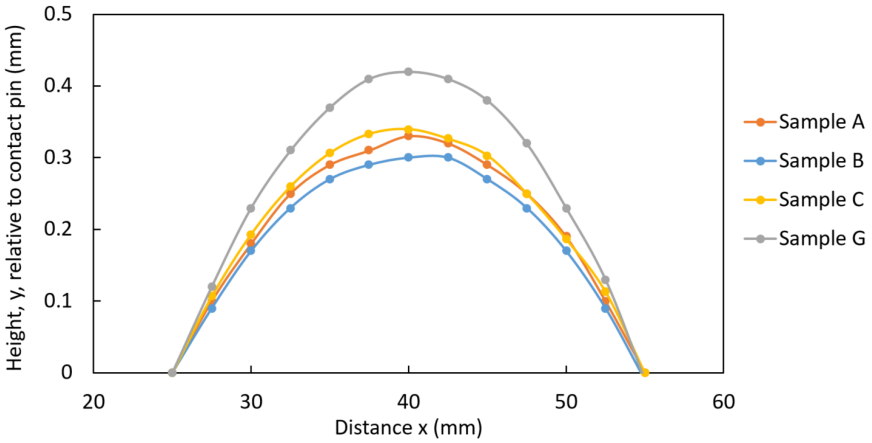

Figure I.1: Permanent deflection profile measurements for the center section of Samples A, B, C and G, height adjusted relative to the contact pin point at y = 0 mm.

The measured profiles can be approximated with a parabolic trend line of the form $y = ax^2 + bx + c$, from which the first and second derivative an easily be derived. Since the samples are thin, 2.18 mm, these y height measurements are taken as the neutral chord displacement, y_0 values for the radius of curvature calculations. Radius of curvature, R is calculated as [53];

$$\frac{1}{R} = \frac{d^2y_0/dx^2}{[1 + (dy_0/dx)^2]^{2/3}}. \tag{I.0.1}$$

The radius of curvature is directly related to strain, since curving requires a change in length. The center chord of the sample, y_0 is the neutral axis, because of its symmetric rectangular cross-section. Therefore, strain due to the curvature depends on the distance, y, from the neutral axis, to a maximum at the surface, or the half thickness of the sample, $y = c$. Equation I.0.1 for the strain in the center, x = 40 mm, simplifies to;

$$\begin{aligned} \frac{1}{R} &= -\frac{\epsilon_x}{y} \\ \text{at } y = c \quad \epsilon &= -\frac{c}{R}\ . \end{aligned} \tag{I.0.2}$$

This strain relates to stress on the surface of the sample through Hooke's law (see Section 2.5.1):

$$\sigma = \epsilon E\ , \tag{I.0.3}$$

The results of this calculation for the profile curves shown in Figure I.1 at the center, $x = 40$ mm, and surface, $y = c = 1.08$ mm, of the sample is summarized in the Table I.1. The stress uncertainty value of 5% was selected to cover the accuracy of the profile measurements, which was $x = \pm 0.01$ mm, and provide a conservative estimate to encompass any non-linearly elastic material behaviour of the sample.

Table I.1: Sample residual stress by radius of curvature from profile measurements.

Sample	**Profile (mm)** $y = ax2 + bx + c$	**Strain** at $x = 40$ mm	**Stress (MPa)** $\sigma = \epsilon E$	**Uncertainty** (5%)
A	y=-0.0015x^2+0.116x-0.16	0.003	664	30
B	y=-0.0014x^2+0.109x-0.57	0.0028	620	30
C	y=-0.0015x^2+0.118x-0.59	0.003	664	30
G	y=-0.0019x^2+0.152x-0.94	0.0038	841	40